

AD A095503

LEVEL II

DNA 5259F

(12)

PRECHARGE ENHANCED SGEMP

Systems, Science and Software
P.O. Box 1620
La Jolla, California 92038

1 May 1980

Final Report for Period 27 November 1978–1 May 1980

CONTRACT No. DNA 001-79-C-0079

APPROVED FOR PUBLIC RELEASE;
DISTRIBUTION UNLIMITED.

DTIC
ELECTED
FEB 26 1981
S D
E

THIS WORK SPONSORED BY THE DEFENSE NUCLEAR AGENCY
UNDER RDT&E RMSS CODE B323079464 R99QAXEE50117 H2590D.

FILE COPY
DNA

Prepared for
Director
DEFENSE NUCLEAR AGENCY
Washington, D. C. 20305

812 26069

Destroy this report when it is no longer needed. Do not return to sender.

PLEASE NOTIFY THE DEFENSE NUCLEAR AGENCY,
ATTN: STTI, WASHINGTON, D.C. 20305, IF
YOUR ADDRESS IS INCORRECT, IF YOU WISH TO
BE DELETED FROM THE DISTRIBUTION LIST, OR
IF THE ADDRESSEE IS NO LONGER EMPLOYED BY
YOUR ORGANIZATION.



UNCLASSIFIED

SECURITY CLASSIFICATION OF THIS PAGE (When Data Entered)

REPORT DOCUMENTATION PAGE		READ INSTRUCTIONS BEFORE COMPLETING FORM
1. REPORT NUMBER 18) DNA 5259F	2. GOVT ACCESSION NO. AD-A095303	3. RECIPIENT'S CATALOG NUMBER
4. TITLE (and Subtitle) PRECHARGE ENHANCED SGEMP	5. TYPE OF REPORT & PERIOD COVERED Final Report for Period 27 Nov 78-1 May 80	6. PERFORMING ORG. REPORT NUMBER SSS-R-80-4413
7. AUTHOR(s) M. J. Mandell, G. W. Schnuelle, D. E. Parks I. Katz, A. R. Wilson, E. M. Waisman P. C. Steen, M. Rotenberg	8. CONTRACT OR GRANT NUMBER(s) DNA 001-79-C-0079	9. PROGRAM ELEMENT, PROJECT, TASK AREA & WORK UNIT NUMBERS Subtask R99QAXEE501-17
10. PERFORMING ORGANIZATION NAME AND ADDRESS Systems, Science and Software P. O. Box 1620 La Jolla, California 92038	11. CONTROLLING OFFICE NAME AND ADDRESS Director Defense Nuclear Agency Washington, D. C. 20305	12. REPORT DATE 1 May 1980
13. NUMBER OF PAGES 120	14. MONITORING AGENCY NAME & ADDRESS (if different from Controlling Office)	15. SECURITY CLASS. (at this report) UNCLASSIFIED
16. DISTRIBUTION STATEMENT (of this Report) Approved for public release; distribution unlimited.	17. DISTRIBUTION STATEMENT (of the abstract entered in Block 20, if different from Report)	15a. DECLASSIFICATION/DOWNGRADING SCHEDULE
18. SUPPLEMENTARY NOTES This work sponsored by the Defense Nuclear Agency under RDT&E RMSS Code B323079464 R99QAXEE50117 H2590D.	19. KEY WORDS (Continue on reverse side if necessary and identify by block number) SGEMP Spacecraft Charging Electrostatic Discharges Blowoff Charge	20. ABSTRACT (Continue on reverse side if necessary and identify by block number) We present analytic and numerical results relevant to the SGEMP response under conditions of strong differential charging, and a theory for dielectric surface discharges. Scaling relations are presented for space charge limited currents near edges of charged dielectrics. A new hybrid electrostatic/electromagnetic SGEMP computer code is presented. Comparisons with experiment are made for precharge-enhanced SGEMP and for surface discharges.

TABLE OF CONTENTS

<u>Section</u>	<u>Page</u>
LIST OF ILLUSTRATIONS - - - - -	3
LIST OF TABLES - - - - -	4
1 INTRODUCTION - - - - -	5
2 EXPERIMENTAL SIMULATION OF PRECHARGE- ENHANCED SGEMP - - - - -	9
2.1 DESCRIPTION OF EXPERIMENTS - - - - -	9
2.2 NASCAP PRECHARGING CALCULATIONS - - - - -	10
2.3 EXPERIMENTAL RESULTS AND CRITIQUE - - - - -	17
3 ANALYTICAL CALCULATIONS - - - - -	19
3.1 ANALYTIC TREATMENT OF ELECTROSTATIC POTEN- TIAL AND PARTICLE TRAJECTORIES NEAR SUDDEN SURFACE POTENTIAL CHANGES - - - - -	19
3.2 ANALYTIC TREATMENT OF SPACE CHARGE LIMITED EMISSION NEAR SUDDEN SURFACE POTENTIAL CHANGES - - - - -	26
3.3 ANALYTIC SOLUTION FOR THE ELECTROSTATIC POTENTIAL OF A CHARGED DISK ON A GROUND PLANE - - - - -	36
4 A HYBRID ELECTROSTATIC/ELECTRODYNAMIC SGEMP COMPUTER CODE - - - - -	39
4.1 WHY DEVELOP YET ANOTHER 2-D SGEMP CODE? - - -	39
4.2 CODE DESCRIPTION - - - - -	40
4.2.1 Mathematical Summary - - - - -	40
4.2.2 Code Structure - - - - -	43
4.3 SIMULATION OF SGEMP EXPERIMENTS - - - - -	46
4.4 SIMULATION OF SPACE CHARGE LIMITED DIS- CHARGES - - - - -	51
5 A THEORY OF DIELECTRIC SURFACE DISCHARGES - -	56

TABLE OF CONTENTS (Continued)

<u>Section</u>		<u>Page</u>
5.1	REVIEW OF THE DATA	56
5.2	THE MODEL	57
5.3	GENERAL DIMENSIONAL CONSIDERATIONS FOR SPACE CHARGE LIMITED EMISSION	59
5.4	PROBLEMS WITH NO LENGTH SCALE	62
5.5	A CLASS OF PROBLEMS WITH ONE LENGTH SCALE	66
5.6	A PROBLEM WITH TWO LENGTH SCALES	67
5.7	COMPARISON WITH EXPERIMENT	68
5.8	CONCLUSION	73
	REFERENCES	76

Appendix

A	MECHANISM FOR SGEMP-TRIGGERED SURFACE FLASHOVER	79
B	RESULTS FOR SGEMP (BESSEL FUNCTION PROFILE) CALCULATIONS	85
C	EFFECT OF EARTH'S MAGNETIC FIELD ON PRE- CHARGING EXPERIMENTS	107

Accession For	
NTIS GRA&I	
DTIC TAB	
Unannounced <input checked="" type="checkbox"/>	
Justification	
By	
Distribution/	
Availability Codes	
Dist	Avail and/or Special
A	

LIST OF ILLUSTRATIONS

<u>Figure</u>		
2.1	NASCAP model of cylindrical SGEMP test object	11
2.2	NASCAP model of insulating surface on SGEMP test object	12
2.3	Voltage profile across teflon surface	14
2.4	Potential contours during charging of teflon surface	15
2.5a	Particle trajectories at equilibrium	16
2.5b	Particle trajectories at equilibrium	16
3.1	Edge location at $X = 0, Y = 0$ line	20
3.2	Geometrical construction for particle trajectories and space charge density near charged edge	21
3.3	Particle trajectory near charged edge	24
3.4	Unique particle trajectory	34
3.5	Potential contours for charged disk on grounded plane	38
4.1	Electrostatic grid used for precharge-enhanced SGEMP/discharge calculations	41
4.2	Grid used for electromagnetic part of precharge-enhanced SGEMP/discharge calculation	42
4.3	Centering scheme for transverse electromagnetic code	44
4.4	Block diagram of hybrid code	45
4.5	Relative surface currents for the baseline precharge case (I) and other cases (II-V)	50
4.6	Predictions of peak SGEMP surface currents	52
4.7	Surface currents versus time	55

LIST OF ILLUSTRATIONS (Continued)

<u>Figure</u>		<u>Page</u>
5.1	Edge location at $X = 0, Y = 0$ line	60
5.2	Two equipotential planes intersecting at angle θ_0	63
5.3	Current density versus radius for various values of healing length, λ	69
5.4	Emission current density (A/m^2)	70
5.5	Emission current density (A/m^2)	71
5.6	Total space charge limited emission current	72
5.7	Emission current comparison	74

LIST OF TABLES

<u>Table</u>		<u>Page</u>
3.1	Numerical Results for Space Charge Limited Flow Between Half Planes	36
4.1	Results of SGEMP Calculations With Bessel Function Profile	48
4.2	Surface Current Response for Discharge	54
5.1	Emission Current Density and Anode Current Density Reduction Factor	65

SECTION 1

INTRODUCTION

This report is a summary of work performed under Contract DNA001-79-C-0079, entitled "Precharge-Enhanced SGEMP". The aim of this effort was to develop phenomenology to model the enhancement of the electromagnetic response of spacecraft resulting from electrostatic charging in the natural space environment or in laboratory simulations.

It is now well-accepted^[1] that geosynchronous spacecraft not infrequently experience "magnetospheric substorms" which cause them to attain negative potentials of ~ 10 kV. Further, spacecraft can charge differentially to potentials sufficient to cause spontaneous electrostatic discharges. Commonly, these discharges cause logic malfunctions requiring correction by ground-based command. In a few instances they have caused serious damage to spacecraft.

Another well-studied area is the electromagnetic response of a spacecraft to an x-ray burst (SGEMP). Typically, an x-ray burst causes emission of ~ 100 A/m² of electrons with energy of ~ 1 keV, together with larger numbers of low energy electrons^[2] for a time $\sim 10^{-8}$ seconds. The electromagnetic response consists of surface currents ~ 1 A/m. Normally, the low energy electrons play a negligible role in this response. Also, increasing the x-ray fluence (and thus the emitted current) does not greatly increase the response because of space charge limiting effects. These space charge effects can be somewhat lessened if the spacecraft is charged negatively; however, a factor of two is the largest enhancement expected from such uniform charging.

Much larger effects are expected if the spacecraft is differentially charged. The basis for this expectation lies in the much larger energies stored in differentially charged

spacecraft. We at Systems, Science and Software^[3] predicted SGEMP enhancements of an order of magnitude under these conditions. Such effects were demonstrated dramatically in measurements^[4] performed by Mission Research Corporation (MRC) on the Skynet Qualification Model. It was found that differentially precharging the model by electron spraying caused SGEMP enhancements of a factor of 5. Also observed was DGEMP - electromagnetic response due to spontaneous discharges. In one irreproducible but well-documented case, a discharge was triggered by an SGEMP pulse.

These findings resulted in two efforts to develop phenomenology for precharge-enhanced SGEMP. MRC was directed to perform experiments using simple geometry and well-characterized materials. Systems, Science and Software was directed to perform the effort described in this report. Our goals were:

1. Provide analytical support (using the NASCAP code)^[5] for the precharging phase of the MRC experiments.
2. Provide consulting services on the general question of laboratory precharging of spacecraft, using the NASCAP code where appropriate.
3. Perform analysis of the MRC experiments.
4. Develop analytical tools and phenomenology appropriate to precharge-enhanced SGEMP, electromagnetic response to discharges and related matters.

In Section 2 we discuss the MRC experiments and our support of them. We address as well (Appendix C) the question of precharging a real spacecraft in a large tank by electron spraying. This question arose in connection with the proposed Satellite X-ray Test Facility (SXTF).^[6] Analysis of precharge-enhanced SGEMP under conditions similar to the MRC experiments appears in Section 4 and Appendix B. We concluded (as did

MRC^[7], in accordance with our previous work^[3]), that the enhancement was associated with acceleration of low energy electrons by strong, localized electric fields.

We abstracted two generic precharge configurations for theoretical treatment. The first (Appendix A) was an emitting surface with a tangential field. This led to the concept of the conductivity of a space charge layer, as well as a possible mechanism for SGEMP-triggered surface flashover. The conductivity concept later proved useful to estimate the skin current in the metallization beneath the emitting dielectric (Section 4.3).

The second generic configuration was a differentially charged edge (step function potential). This configuration is analyzed in Section 3. A first surprising result (747 effect) was that the anode current density was nearly three orders of magnitude below the cathode current. The problem could also be done self-consistently with space charge. The "747 effect" then became a less exciting "38 effect", and the space charge limited current was found to be divergent. Also in Section 3 is the analytic solution for the potential of a charged disk on a ground plane.

Section 4 describes a new hybrid electrostatic/electrodynamic 2-D code designed to study SGEMP under conditions where high local resolution is required. This problem has been applied both to the MRC type problem and to discharges, and has proven to be an excellent analytical tool.

Finally, Section 5 describes a theory of dielectric surface discharges. We postulate that during a discharge the entire dielectric surface behaves as a space charge limited emitter. As noted above, the current for a step-function potential is divergent, so it is necessary to postulate a voltage profile near the edge of the dielectric. The scaling of the current and the character of the emission

profile is treated analytically in detail. Additional information comes from simulations using the code described in Section 4. We find that this theory gives good agreement with experimental measurements.

In summary, we have found that the electromagnetic response to x-rays under precharged conditions, or to discharges, is dominated by the flow of low energy electrons in strong local fields. We have proposed a mechanism for SGEMP-triggered flashover involving these low energy electrons. We have shown how amplification of the SGEMP response by an order of magnitude over the non-precharged response is possible. We have developed both computational tools and approximate theoretical models to aid in predicting this response. Such models could be incorporated as "effective source" treatments in a practical 3-D SGEMP code. In addition, we have shown NASCAP to be a helpful tool for analysis of precharging under laboratory conditions and for design of experiments.

SECTION 2

EXPERIMENTAL SIMULATION OF PRECHARGE-ENHANCED SGEMP

The experimental program designed to study precharge-enhanced SGEMP is described in this section. A very brief outline of the experimental details is given in Section 2.1. NASCAP charging simulations performed by S³ to aid in the experimental design and setup are presented in Section 2.2. The main results of the experiments are summarized and assessed in Section 2.3.

2.1 DESCRIPTION OF EXPERIMENTS

During the early part of 1979 experiments were performed by Mission Research Corporation (MRC) using the OWL II¹ photon source to study precharge-enhanced SGEMP. MRC has described these experiments elsewhere.^[7] This discussion is included for completeness, and to provide a context for the analytical and simulation work which follows.

The basic experiment consisted of an aluminum cylinder, 1.2 m in diameter and 51 cm long, with an 82 cm diameter hole in one end against which a sample was placed. We will be concerned with two of the four samples used: 0.013 cm silvered teflon mounted on a copper backplate, and 0.05 cm white paint on fiberglass mounted on a segmented backplate. The experiment was located in an approximately cylindrical tank with effective radius ~1.2 m and length ~3.5 m.

The insulating surfaces were charged by an electron gun with $\sim 10^{-9}$ A/cm² current over a period of several minutes to potentials of 10 kV to 15 kV. The potential was far from uniform along the surface; it was commonly measured to vary several kilovolts on a few centimeter scale.

The primary measurement taken upon photon exposure was the current between the aluminum cylinder and the sample backplate (teflon sample), or the currents between backplate segments (paint sample). Photodiodes were used to determine pulse characteristics, and the final object potential was measured. During the time of the photon pulse the cylinder was effectively ungrounded.

2.2 NASCAP PRECHARGING CALCULATIONS

The NASCAP code was used to simulate the precharging of the MRC test object. The results of these calculations were described to MRC experimenters in advance of their SGEMP test series to assist them in the design and interpretation of their experiments.

NASCAP allows a detailed simulation of the charging of an object in a test tank environment, as documented elsewhere.^[5] A charging surface is described in terms of its thickness, dielectric constant, energy and angle dependent emission, as well as bulk and surface conductivity. The initial beam current profile can be specified at the sample surface, and electrostatic effects on the incident electron trajectories are included as the charging proceeds. Complicated current profiles, such as that produced by a rastered beam, can be included in the simulation.

The NASCAP model of the SGEMP test object is illustrated in Figures 2.1 and 2.2. NASCAP solves Poisson's equation on a cubic mesh, on which an octagonal prism was used to model the aluminum cylinder. The insulating surface was normal to the axis of the electron gun, located approximately 2 m above the test object. The cylinder and the surrounding tank were grounded throughout the charging simulations.

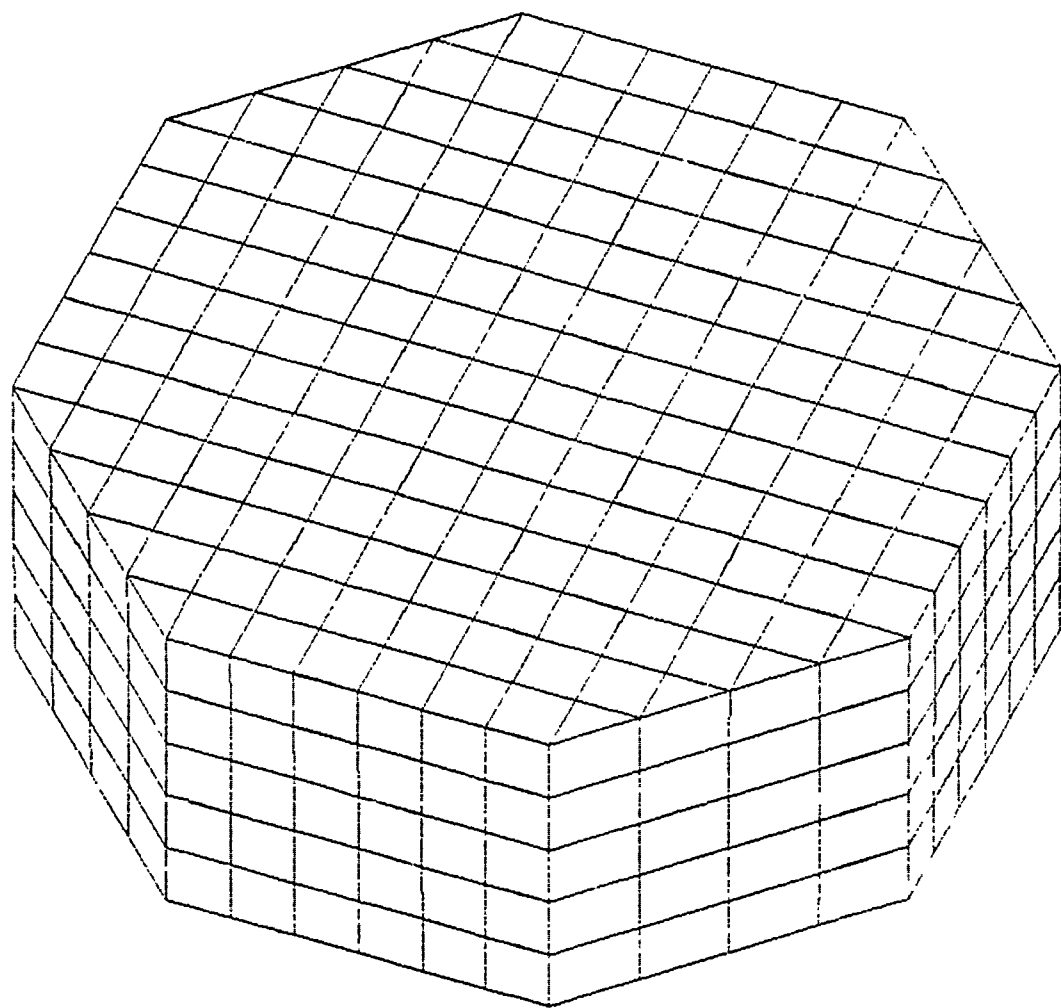


Figure 2.1. NASCAP model of cylindrical SGEMP test object.
Zone size = 8.6 cm.

SURFACE CELL MATERIAL COMPOSITION AS VIEWED FROM THE NEGATIVE Z DIRECTION

FOR Z VALUES BETWEEN -1 AND 21

MATERIAL LEGEND

1	ALUMIN	□
5	TEFLON	▨

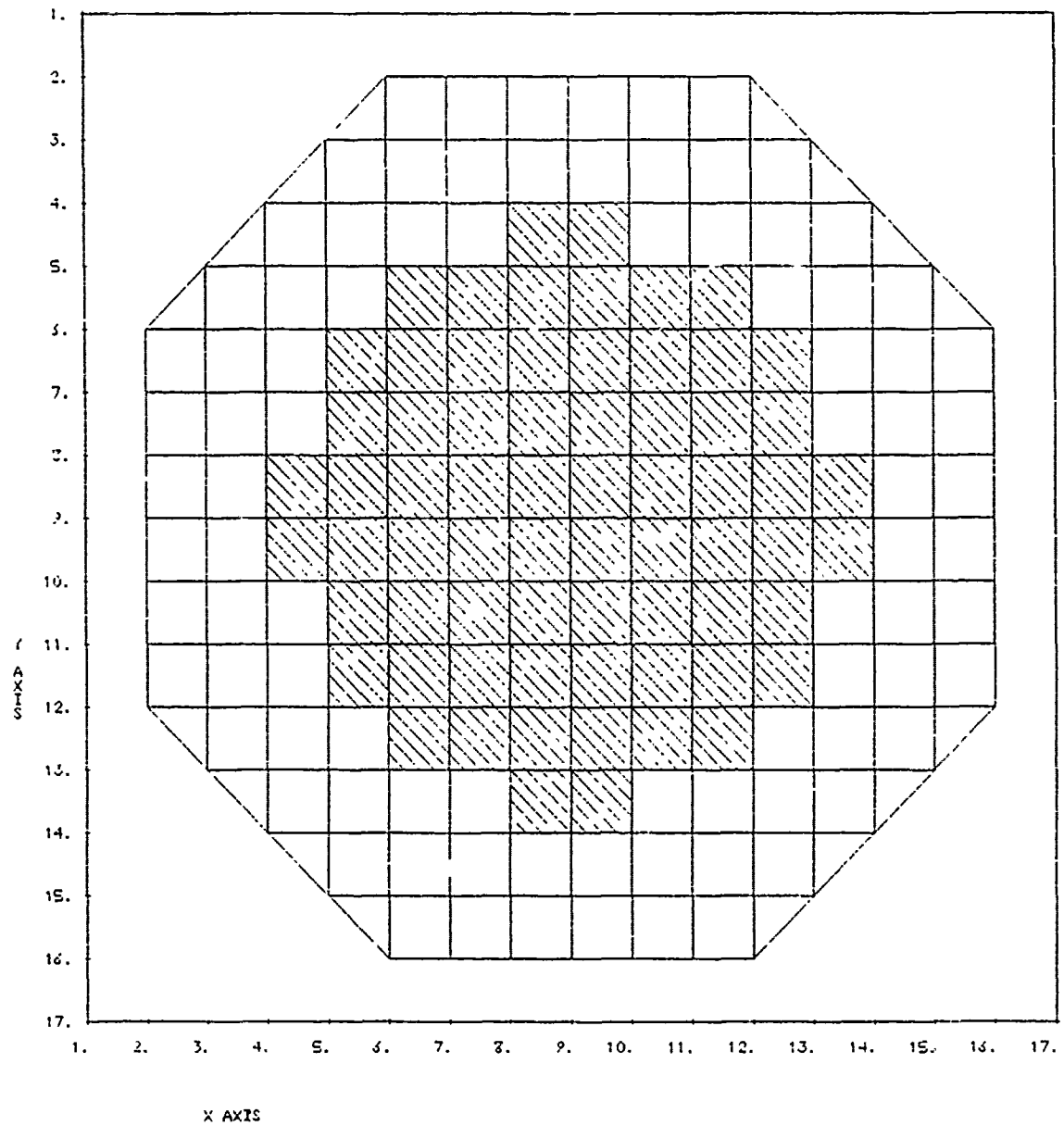


Figure 2.2. NASCAP model of insulating surface on SGEMP test object.

Results of the charging study for a teflon insulating surface using a 10 kV beam are illustrated in Figures 2.3 through 2.5. The initial electron beam profile was taken to be uniform across a circular region of variable radius, while the sample radius was fixed at 40 cm. The MRC experimenters expressed an interest in predicted voltage profiles as the initial radius of the charging beam was reduced below the insulating sample radius, so that the edges of the sample might remain near zero potential. The voltage profile for an initial beam radius of 40 cm was almost indistinguishable from that for the 30 cm case, illustrated in Figure 2.3. The strong electric fields near the edge of the sample deflect the 30 cm beam so that the entire surface is sprayed with electrons. The potential contours during charging which cause the beam spreading are shown in Figure 2.4, and typical trajectories are shown in Figure 2.5a. In both cases, the sample charges less near the edges due to a higher yield of secondary electrons for non-normal incidence. Also shown in Figure 2.3 is the voltage profile resulting from a beam initially 10 cm in radius. In this case the beam spreading, shown in Figure 2.5b, is not as large since the integrated deflecting forces are much reduced for such a collimated beam. A significant fraction of the insulator remains uncharged, and the potential gradient is large near the beam edge. As a result of the above study, MRC experimenters were aware before their test series that sample shields or very restricted beams would be required if the effects of a sharp potential gradient located some distance from the sample edge were to be investigated.

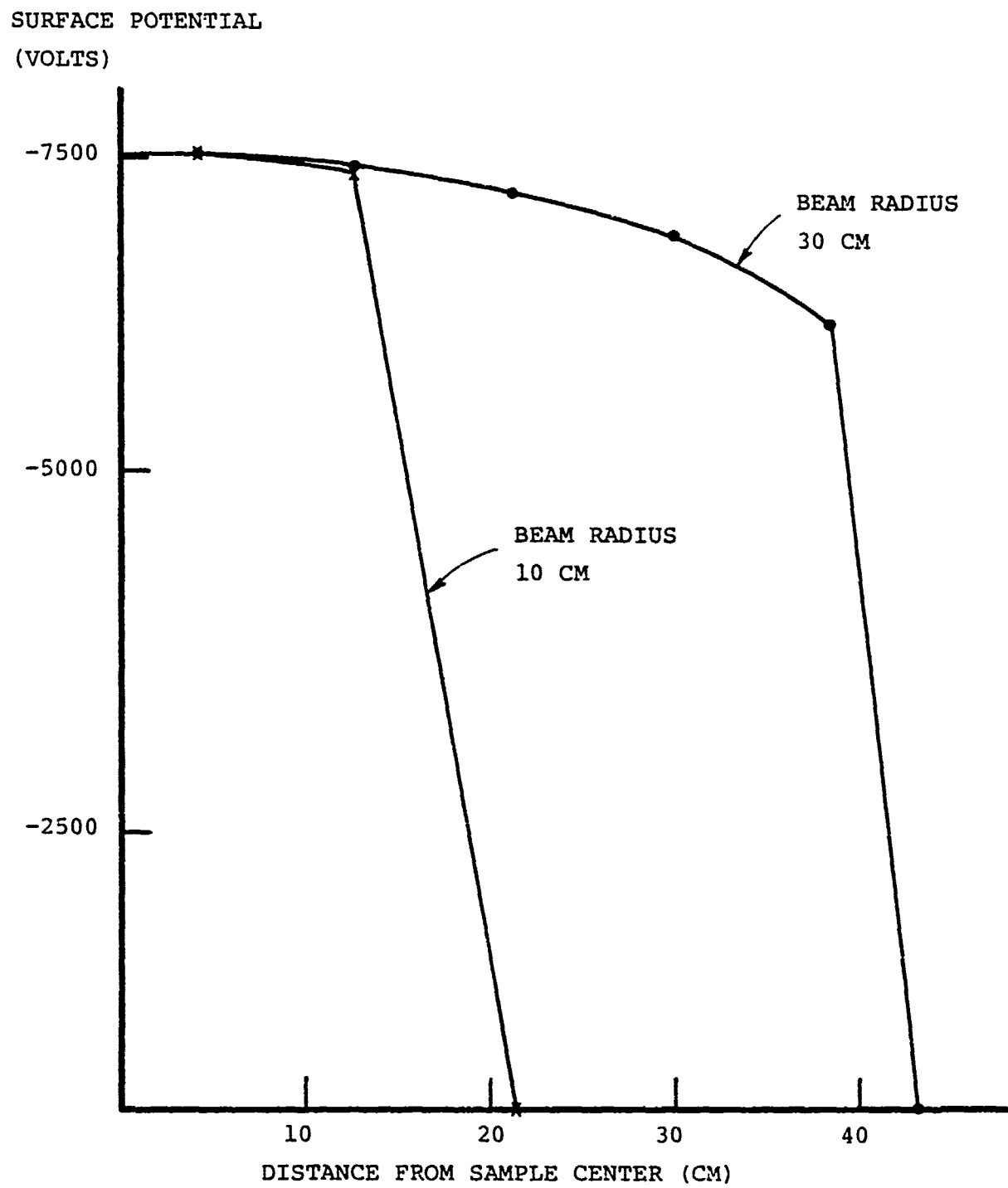


Figure 2.3. Voltage profile across teflon surface. Beam voltage = 10 kV.

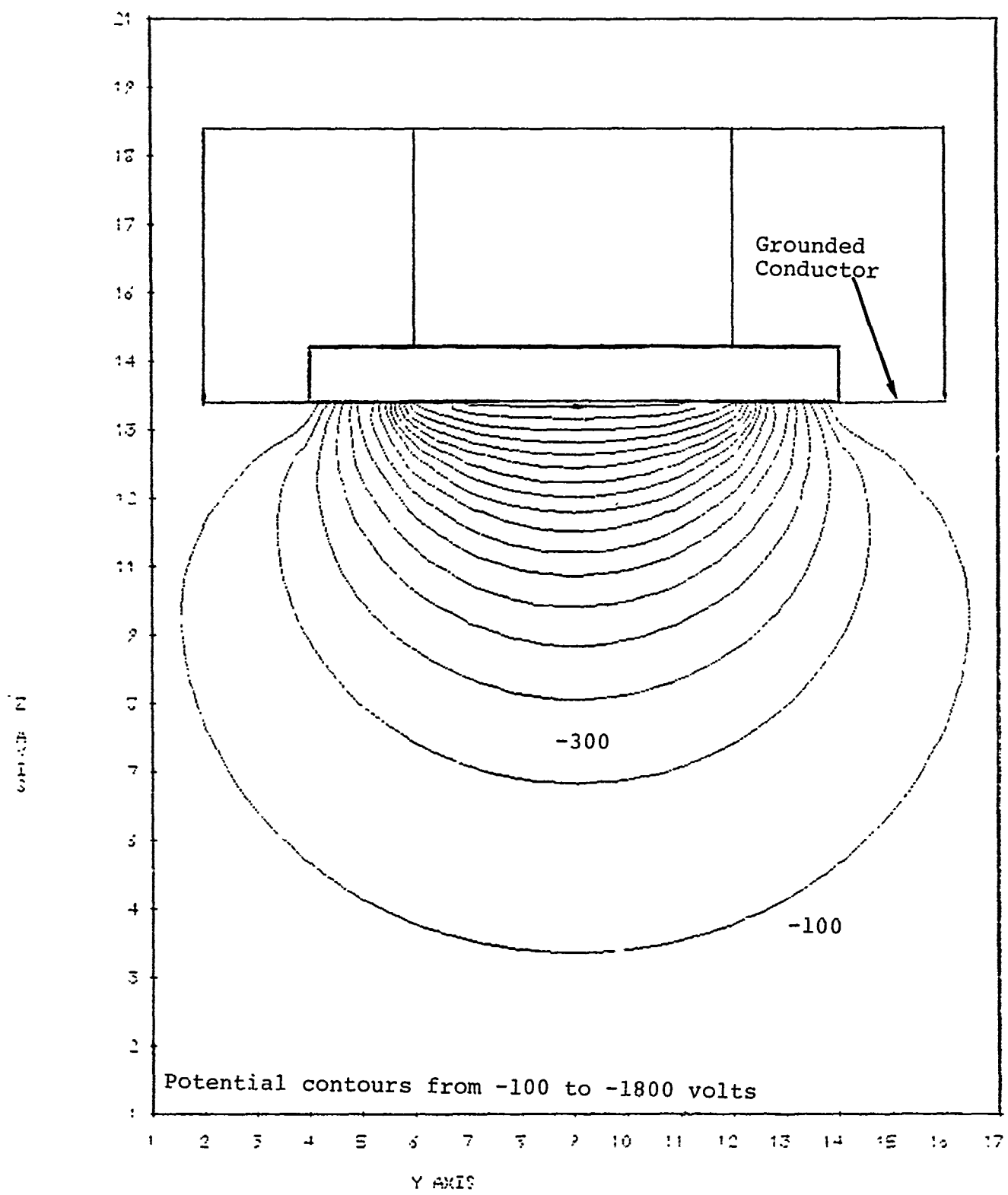


Figure 2.4. Potential contours during charging of teflon surface.

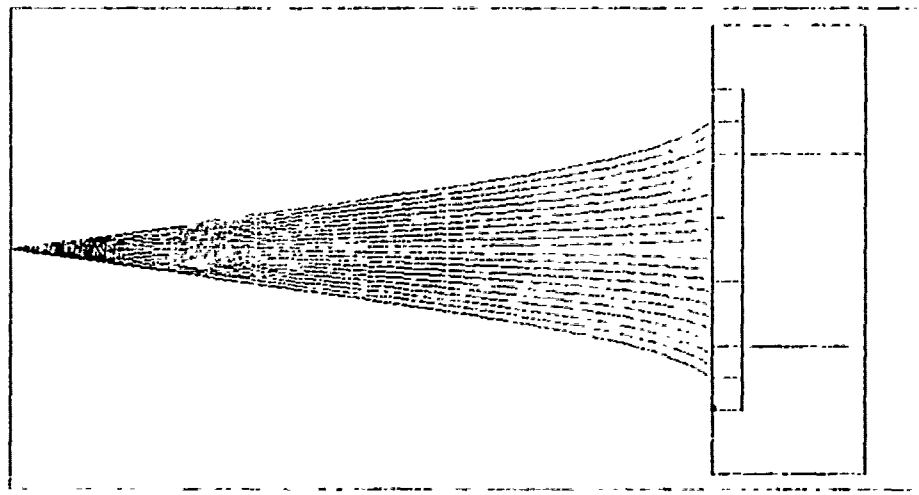


Figure 2.5a. Particle trajectories at equilibrium. Initial beam radius = 30 cm.

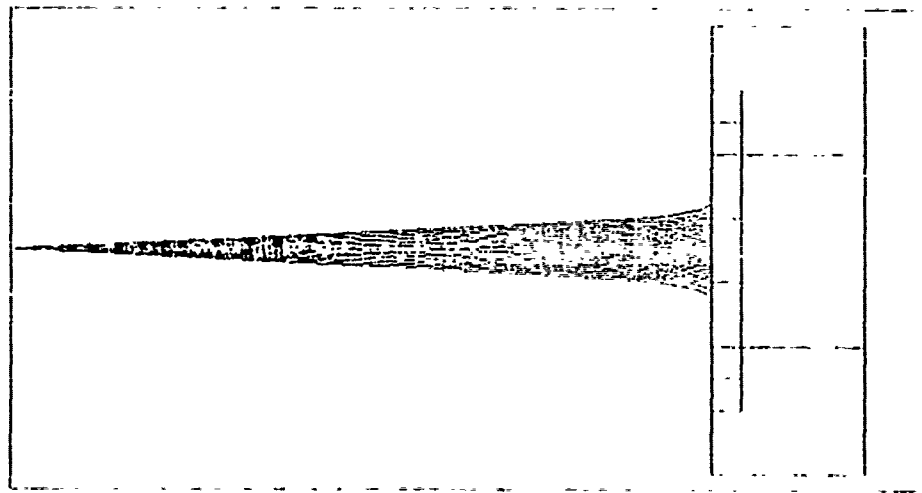


Figure 2.5b. Particle trajectories at equilibrium. Initial beam radius = 10 cm.

2.3 EXPERIMENTAL RESULTS AND CRITIQUE

For comparison with results to be presented later, there were three main results from these experiments:

1. Increased Surface Currents

Under precharged conditions surface currents of 10-20 A/m were measured at the sample edges. By comparison, non-precharge shots had surface currents an order of magnitude less.

2. Lack of Surface Discharging

In general, no significant dielectric discharging was seen. This was expected: given 10 pf/cm^2 and 10 mA/cm^2 for 10^{-7} seconds, $\Delta V/V = 100 \text{ volts/15 kilovolts}$. However, in one or two cases substantial local redistribution of charge was observed.

3. Blowoff Charge

The potential reached by the body is a measure of the blowoff charge. Typically this potential was 1-2 kV, indicating a blowoff of $\sim 0.3 \mu\text{C}$. In at least one case, however, an additional $\sim 1 \mu\text{C}$ of charge was blown off during $\sim 1 \mu\text{sec}$ following the shot. MRC referred to this phenomenon as "delayed photocurrent".

Most of the difficulties with these experiments were beyond the control of MRC. The small number of photon shots and their irreproducibility make the data difficult to interpret. There were questions of debris being shot into the experiment area. Also, the nonuniform potentials on the dielectric surfaces complicates some interpretations. Because of these factors, planned experiments such as narrow or patterned charging profiles had to be abandoned.

As theorists attempting to obtain data for interpretation we found that the data taken as polaroid scope pictures was very difficult to work with. These data included the object potential measurement and the back-biased diode data used to characterize the photon pulse. The diodes having

insulating materials were in unknown states of precharge and gave conflicting results from shot to shot. Also these pictures reproduced so badly as to be often unreadable when we obtained them.

Despite the above difficulties, we believe these experiments provide good estimates of the amount of SGEMP enhancement expected from precharging. They can be used to validate predictive theories and computer codes. The delayed effects which were seen represent a type of discharge, and show that nuclear photons can trigger weak, localized discharges. Even though strong triggered discharges, such as observed in the previous Skynet tests, were not seen here, we feel that such strong synergistic effects remain a real possibility.

SECTION 3

ANALYTICAL CALCULATIONS

This section describes the analytical solution of three model problems which illustrate the behavior of electrostatic potentials and electron trajectories near sudden surface potential changes. Although these model problems are considerably simplified abstractions of real experiments, they provide insight into the central physical mechanisms, and they generate parametric representations of SGEMP response which can represent or even replace the results of more detailed simulations. Potentials and electron trajectories near the interface of infinite half planes is discussed in Section 3.1, and the space charge limited flow of electrons between such half planes is analyzed in Section 3.2. The analytic potentials around a charged disc are presented in Section 3.3.

3.1 ANALYTIC TREATMENT OF ELECTROSTATIC POTENTIAL AND PARTICLE TRAJECTORIES NEAR SUDDEN SURFACE POTENTIAL CHANGES

The largest effects of differential charging in SGEMP occur in the immediate vicinity of edges between charged and uncharged surfaces (e.g., charged dielectric and exposed, grounded conductor). Naively, one would expect large currents of electrons to follow field lines from one surface to the other. This turns out not to be the case; in fact, the current density incident on the collecting surface is nearly three orders of magnitude less than the current density on the emitting surface.

Consider the situation shown in Figure 3.1. Let r denote the radial distance from the edge, and θ the angle, (see Figure 3.2). The electrostatic potential $\phi(r, \theta)$ satisfies the Laplace equation

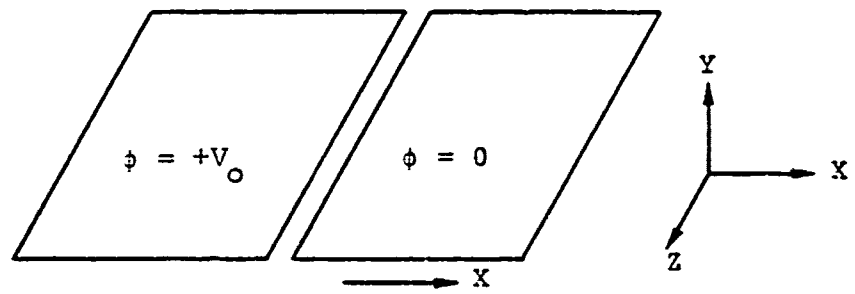


Figure 3.1. Edge is located at $X = 0$, $Y = 0$ line.

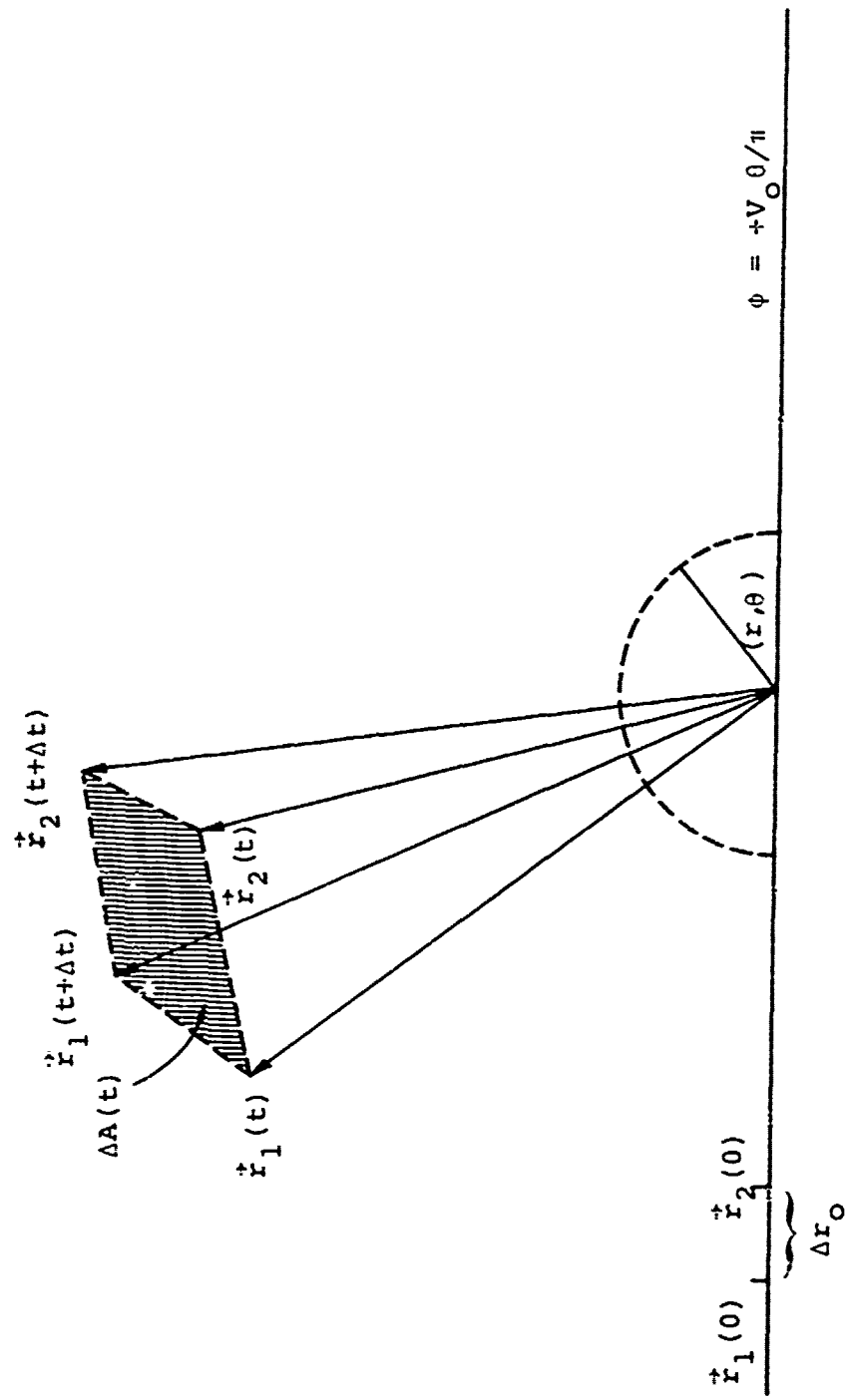


Figure 3.2. Geometrical construction for particle trajectories and space charge density near charged edge.

$$\nabla^2 \phi(r, \theta) = 0 \quad (3.1)$$

with boundary conditions

$$\phi(r, \theta=\pi) = +V_0, \quad \phi(r, \theta=0) = 0 \quad (3.2)$$

where r is the distance from the edge and θ the angle measured from the grounded to the positive surface. The potential $\phi(r, \theta)$ which satisfies (3.1) and (3.2) is:

$$\phi(r, \theta) = +V_0 \frac{\theta}{\pi} \quad (3.3)$$

Electrons emitted from the positive surface will be immediately limited by the electrostatic field, so we need to consider emission only from the grounded surface.

Let us find the trajectory of an electron leaving from the left half plane, with initial position (r_0, π) . The Lagrangian is given by:

$$\mathcal{L}(r, \theta) = T - V = T + e\phi = \frac{1}{2} mr^2 + \frac{1}{2} mr^2 \dot{\theta}^2 + eV_0 \frac{\theta}{\pi} \quad (3.4)$$

It is advantageous to write \mathcal{L} in terms of the dimensionless radius, $R \equiv r/r_0$, and time

$$\tau \equiv \frac{t}{r_0} \left(\frac{eV_0}{m\pi} \right)^{1/2} \quad (3.5)$$

In terms of R , τ and using primes to denote the derivative with respect to τ one obtains

$$\frac{\pi}{eV_0} \mathcal{L}' = \frac{1}{2} (R'^2 + R^2 \dot{\theta}'^2) - \theta \quad (3.6)$$

Thus, if initially ($\tau = 0$) the dimensionless angular momentum $R^2 \dot{\theta}'$ is zero, it follows that

$$R^2 \dot{\theta}^2 = -\tau \quad (3.7)$$

and

$$R^3 \dot{R}^2 = \tau^2 \quad (3.8)$$

Equations (3.7) and (3.8) together with energy conservation, result in a single dimensionless particle trajectory for electrons emitted with negligible initial energy $[R^*(\tau=0) = \theta^*(\tau=0) = 0]$:

$$\varepsilon = + \frac{1}{2} (R^*{}^2 + \tau^2/R^2) \quad (3.9)$$

We have solved for the single trajectory numerically; we show it in Figure 3.3. Defining $(X, Y) = (R \cos \theta, R \sin \theta)$, this trajectory has the following properties:

- The particle returns back to the plane on the left hand side, $(\theta = \pi)$, of the edge at $X = R \approx -747$, at $\tau = 314$.
- $Y_{\max} = 48$ and occurs at $X = 250$.
- $Y(x=0) = 2.5$.
- $dY/dX (\theta = \pi) \approx -0.17$ (angle of incidence = 80°).

It is instructive, as an example, to notice that at $V_0 = 10$ kV and $r_0 = 1$ cm the time taken to return to the plane is 132×10^{-9} sec. We may conclude that, in the absence of space charge effects, current emitted from a negatively charged surface returns to a neighboring position only after a long time and at low current density (down by 747). Effectively, this current may be considered to escape the neighborhood of the spacecraft or test object.

We now can derive the charge density of electrons moving in this Laplace field. We can do that analytically because of the existence of a unique trajectory. Consider

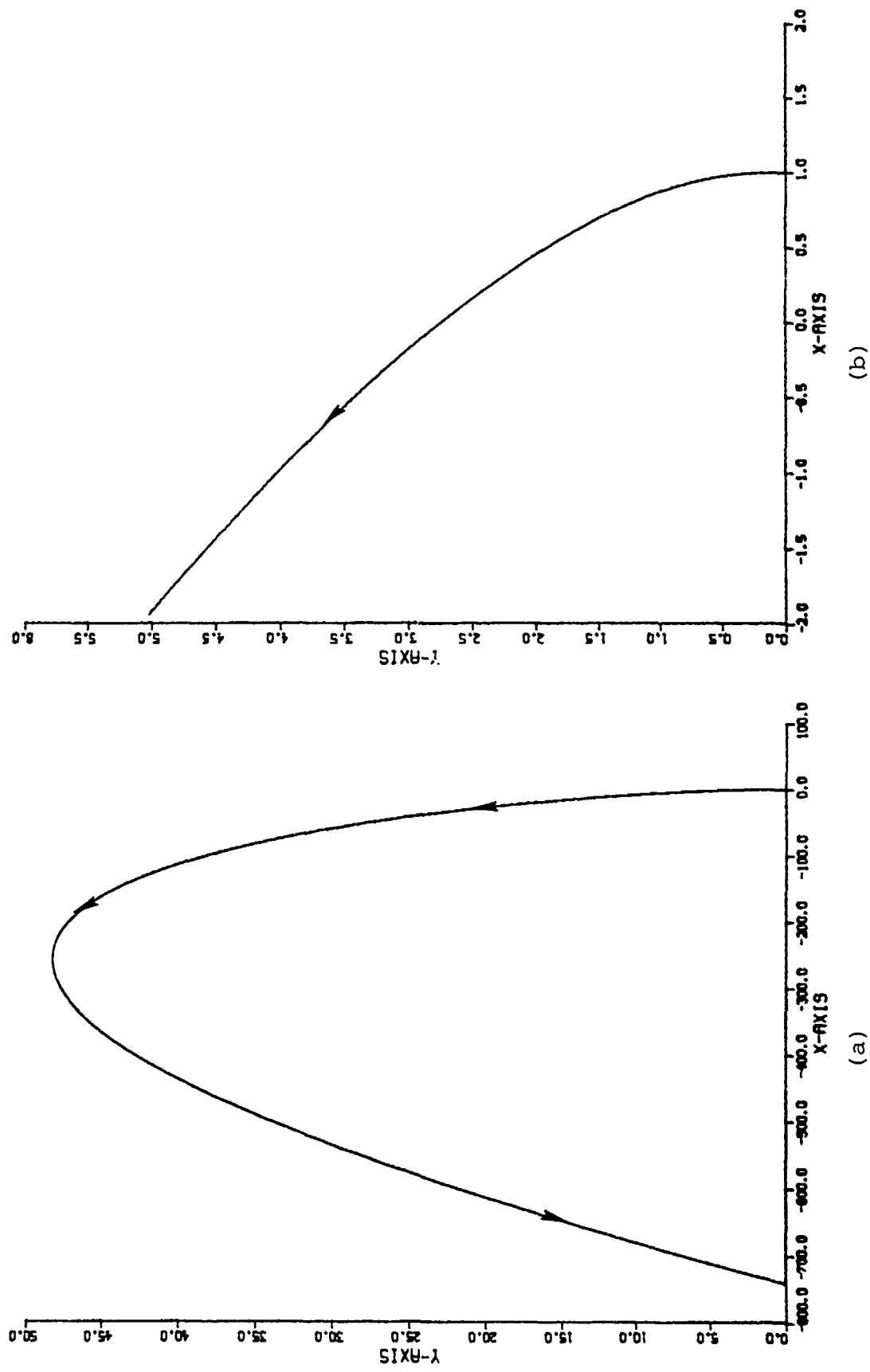


Figure 3.3. Particle trajectory near charged edge: (a) full trajectory;
 (b) initial portion of trajectory.

electrons emitted at $r_o < r < r_o + dr_o$ and between t and $t + dt$. Conservation of charge implies

$$\iint \rho r dr dt d\theta = \iint J_o dt dr_o \quad (3.10)$$

(See Figure 3.2.) Since Eq. (3.10) holds for an arbitrary domain of integration it follows that

$$\rho = J_o / \left(r \left| \frac{\partial(\theta, r)}{\partial(t, r_o)} \right| \right) \quad (3.11)$$

where $\partial(\theta, r) / \partial(t, r_o)$ stands for the Jacobian of (θ, r) with respect to (t, r_o) . Using the scaling implied by (3.5) and Eqs. (3.7) and (3.9) we obtain

$$\rho(r, \theta) = \frac{J_o}{\tau \left(\frac{eV_o}{\pi m} \right)^{1/2}}, \quad (3.12)$$

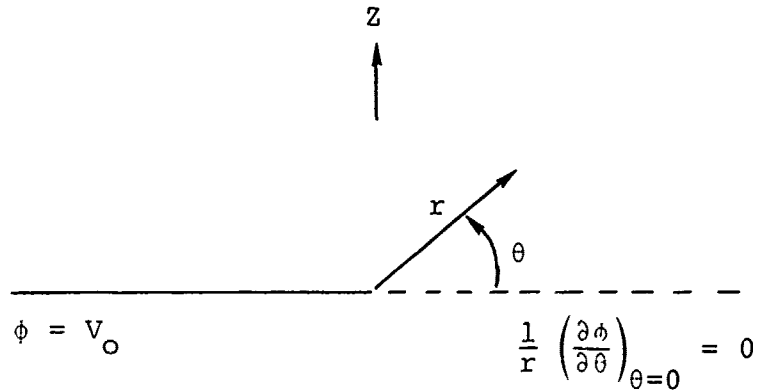
where τ is the dimensionless time it takes an electron to reach point (r, θ) .

Equation (3.12) allows us to obtain (non-self-consistently) the space charge limiting field as a function of time and distance from the edge. This should provide a simple way of estimating the SGEMP enhancement due to differential charging.

3.2 ANALYTIC TREATMENT OF SPACE CHARGE-LIMITED EMISSION NEAR SUDDEN SURFACE POTENTIAL CHANGES

Problem Definition, Geometry and Boundary Conditions

Consider the half space $Z \geq 0$, bounded at $Z = 0$ by an infinite plane, the left half ($\theta = \pi$) is at potential V_0 , right half plane ($\theta = 0$) is grounded, electrons are emitted with zero initial velocity, and $\phi(r,0) \xrightarrow{r \rightarrow \infty} 0$. What is the space charge-limited emission $j(r,0)$ from $\theta = 0$?



Dimensional Considerations

The solution of Poisson's equation and Newton's equations consistent with the boundary conditions, and the initial conditions of electron motion, can be expressed in terms of the dimensional quantities r_0 , t , V , e , and m , where r_0 is the initial radius. We consider these to be the independent variables of the problem. The only dimensionless combination that can be formed from these quantities is

$$\tau = \frac{v_o t}{r_o} \quad (3.13)$$

where v_o is given by

$$\frac{1}{2} mv_o^2 = eV \quad (3.14)$$

Consequently, we may write:

Electron radial and angular positions

$$r = r_o R(\tau) \quad (3.15)$$

$$\theta = \theta(\tau) \quad (3.16)$$

Electric potential

$$\phi = V \Phi(\tau) \quad (3.17)$$

Electron density

$$n = \frac{V}{er_o^2} N(\tau) \quad (3.18)$$

Electron particle current density

$$j = \frac{1}{2\pi} \left(\frac{2e}{m} \right)^{1/2} \frac{V^{3/2}}{r_o^2} J(\tau) \quad (3.19)$$

Observe in particular that the solutions are separable into products of functions of r_o and functions of τ . Because of Eq. (3.16), this separability is preserved if θ rather than τ is used as an independent variable.

Solutions

The remainder of this section will be directed toward obtaining $R(\tau)$, $\theta(\tau)$, $\phi(\tau)$, $N(\tau)$ and $J(\tau)$. Of particular interest is the current density on the emitting surface.

Consider first the equations of motion

$$m \left(\frac{\partial \dot{r}}{\partial t} \right)_{r_0} = mr\dot{\theta}^2 + e \left(\frac{\partial \Phi}{\partial r} \right)_\theta \quad (3.20)$$

$$m \left(\frac{\partial}{\partial t} (r^2 \dot{\theta}) \right)_{r_0} = e \left(\frac{\partial \Phi}{\partial \theta} \right)_r \quad (3.21)$$

where

$$\cdot \rightarrow \left(\frac{\partial}{\partial t} \right)_{r_0}$$

With the help of Eqs. (3.13) through (3.17), these equations become

$$R(R'' - R\theta'^2) = \frac{1}{2} r_0 \left(\frac{\partial \Phi}{\partial r} \right)_\theta \quad (3.22)$$

$$\frac{d}{d\tau} R^2 \theta' = \frac{1}{2} \left(\frac{\partial \Phi}{\partial \theta} \right)_r \quad (3.23)$$

where

$$\cdot \rightarrow \frac{d}{d\tau} = \left(\frac{\partial}{\partial \tau} \right)_{r_0}$$

subject to the initial conditions

$$\theta' = 0 \text{ at } \tau = 0 \quad (3.24)$$

Later, in analyzing the potential equations we will require transformations from r, θ to r_0, τ :

$$\left(\frac{\partial}{\partial r}\right)_\theta = \left(\frac{\partial}{\partial r_o}\right)_\tau \left(\frac{\partial r_o}{\partial r}\right)_\theta + \left(\frac{\partial}{\partial \tau}\right)_{r_o} \left(\frac{\partial \tau}{\partial r}\right)_\theta \quad (3.25)$$

$$\left(\frac{\partial}{\partial \theta}\right)_r = \left(\frac{\partial}{\partial r_o}\right)_\tau \left(\frac{\partial r_o}{\partial \theta}\right)_r + \left(\frac{\partial}{\partial \tau}\right)_{r_o} \left(\frac{\partial \tau}{\partial \theta}\right)_r \quad (3.26)$$

From Eqs. (3.15) and (3.16)

$$\left(\frac{\partial \tau}{\partial r}\right)_\theta = 0 \quad (3.27)$$

$$\left(\frac{\partial r_o}{\partial r}\right)_\theta = \frac{1}{R} \quad (3.28)$$

$$\left(\frac{\partial \tau}{\partial \theta}\right)_r = \frac{1}{\theta} \quad (3.29)$$

$$\left(\frac{\partial r_o}{\partial \theta}\right)_r = - \frac{r_o R'}{R \theta'} \quad (3.30)$$

so that

$$\left(\frac{\partial}{\partial r}\right)_\theta = \frac{1}{R} \left(\frac{\partial}{\partial r_o}\right)_\tau \quad (3.31)$$

$$\left(\frac{\partial}{\partial \theta}\right)_r = - \frac{r_o R'}{R \theta'} \left(\frac{\partial}{\partial r_o}\right)_\tau + \frac{1}{\theta'} \left(\frac{\partial}{\partial \tau}\right)_{r_o} \quad (3.32)$$

Now consider Poisson's equation

$$\frac{1}{r} \frac{\partial}{\partial r} r \frac{\partial \phi}{\partial r} + \frac{1}{r^2} \frac{\partial^2 \phi}{\partial \theta^2} = 4\pi n e \quad (3.33)$$

In steady state the electron density is related to the dynamical variables by the conditions of charge conservation

$$\int_{V(r, \theta)} nr dr d\theta = \int_{S(r_o, t)} j(r_o, 0) dr_o dt \quad (3.34)$$

where the region V in r, θ space is determined from the emission region S in r_o, t space by that dynamical transformation defined by the equations of motion. Since we may choose S arbitrarily

$$nr \frac{\partial(r, \theta)}{\partial(r_o, t)} = j(r_o, 0) \quad (3.35)$$

or

$$nr \left[\left(\frac{\partial r}{\partial r_o} \right)_t \left(\frac{\partial \theta}{\partial t} \right)_{r_o} - \left(\frac{\partial r}{\partial t} \right)_{r_o} \left(\frac{\partial \theta}{\partial r_o} \right)_t \right] = j(r_o, 0) \quad (3.36)$$

From (3.15) and (3.16)

$$\left(\frac{\partial r}{\partial r_o} \right)_t = R - R' \tau \quad (3.37)$$

$$\left(\frac{\partial r}{\partial t} \right)_{r_o} = R' v_o \quad (3.38)$$

$$\left(\frac{\partial \theta}{\partial r_o} \right)_t = -\theta' \frac{\tau}{r_o} \quad (3.39)$$

$$\left(\frac{\partial \theta}{\partial t} \right)_{r_o} = \theta' \frac{v_o}{r_o} \quad (3.40)$$

whence

$$n = \frac{j(r_o, \theta)}{v_o R^2 \theta'} \quad (3.41)$$

Return now to Poisson's equation and evaluate the radial derivatives

$$\frac{1}{r} \frac{\partial}{\partial r} r \frac{\partial \phi}{\partial r} = \frac{V}{r_o R} \frac{\partial}{\partial r_o} \left(r_o \left(\frac{\partial \phi}{\partial r} \right)_{\theta} \right)_{\tau} \quad (3.42)$$

where on the right hand side $\partial/\partial r_o$ is taken at constant τ and on the left hand side $\partial/\partial r$ is taken at constant θ .

Using Eq. (3.22)

$$\frac{1}{r} \frac{\partial}{\partial r} r \frac{\partial \phi}{\partial r} = \frac{2V}{r_o R} \left(\frac{\partial}{\partial r_o} R (R' - R \theta'^2) \right)_{\tau} = 0 \quad (3.43)$$

since R and θ are functions of τ alone. Similarly we find

$$\frac{1}{r} \frac{\partial^2 \phi}{\partial \theta^2} = \frac{2V}{\theta'} \frac{\partial^2 R^2 \theta'}{\partial \tau^2} \quad (3.44)$$

Recalling Eqs. (3.19) and (3.41), Poisson's equation reduces to

$$\frac{d^2 (R^2 \theta')}{d\tau^2} = J(0) \quad (3.45)$$

From Eq. (3.21) and the required vanishing of initial velocity and normal electric field at $\theta = 0$, the solution of (3.45) is

$$R^2 \theta' = \frac{1}{2} J(0) \tau^2 \quad (3.46)$$

Now from Eqs. (3.22) and (3.31)

$$R^2 (R'' - R\theta'^2) = \frac{r_o}{2} \left(\frac{\partial \phi}{\partial r_o} \right)_\tau = K \quad (3.47)$$

where K is a constant independent of r_o and τ . Since ϕ must vanish at $r_o \rightarrow \infty$ on $\theta = 0$ ($\tau=0$)

$$K = 0 \quad (3.48)$$

so that

$$\phi(r_o, 0) = 0 \quad (3.49)$$

$$R^3 R'' = \frac{1}{4} J^2(0) \tau^4 \quad (3.50)$$

The constant $J(0)$ follows from energy conservation and the boundary condition $\phi = 1$ on the reduced potential on the surface $\theta = \pi$ where $\tau = \tau_o$:

$$R'^2(\tau_o) + R^2(\tau_o)^2 \theta'^2(\tau_o) = 1 \quad (3.51)$$

The reduced emission current $J(0)$ is the value that renders the solutions of (3.46) and (3.50) consistent with the condition (3.51). The evaluation of $J(0)$ is simplified by the substitution

$$s = J(0)^{1/3} \tau = J(0)^{1/3} \frac{v_o t}{r_o} \quad (3.52)$$

giving

$$R^3 \frac{d^2 R}{ds^2} = \frac{1}{4} s^4 \quad (3.53)$$

$$R^2 \frac{d\theta}{ds} = \frac{1}{2} s^2 \quad (3.54)$$

$$\left(\frac{dR}{ds} (s_0) \right)^2 + R^2(s_0) \left(\frac{d\theta}{ds} (s_0) \right)^2 = J(0)^{-2/3} \quad (3.55)$$

with s_0 determined from

$$\pi = \int_0^{s_0} \frac{d\theta}{ds} ds = \frac{1}{2} \int_0^{s_0} \frac{s^2 ds}{R^2} \quad (3.56)$$

The solution is trivially generalized to the case of an angle $\alpha \neq \pi$ between the two half planes.

Particle Trajectory

The problem reduces to the determination of the unique particle trajectory established by the functions R and θ (Eqs. 3.15, 3.16) which are solutions of Eqs. (3.53), (3.54).

The constant $J(0)$ is given by Eq. (3.55). The space charge limited electron current density on the half plane emitting surface, j_{HP} , is related to $J(0)$ by

$$j_{HP} = \frac{1}{2\pi} \left(\frac{2e}{m} \right)^{1/2} \frac{v^{3/2}}{r_0^2} J(0) \quad (3.57)$$

The trajectory was generated by numerical integration of Eqs. (3.53) and (3.54) using a second-order leapfrog scheme, with boundary conditions $R(0) = 1$, $R'(0) = 0$, $\theta(0) = 0$. Figure 3.4 displays the solution. An electron emitted at $r = 1$ from the $\theta = 0$ half-plane rises to a maximum height of 6.7 before returning to the $\theta = \pi$ half-plane at $r = 38$. (The corresponding figures for the zero space charge case are maximum height of 48 and return at $r = 747$.) For $V = -10$ kV and $r = 1$ cm, the time to return to the plane is 11 nanoseconds.

PARTICLE TRAJECTORY

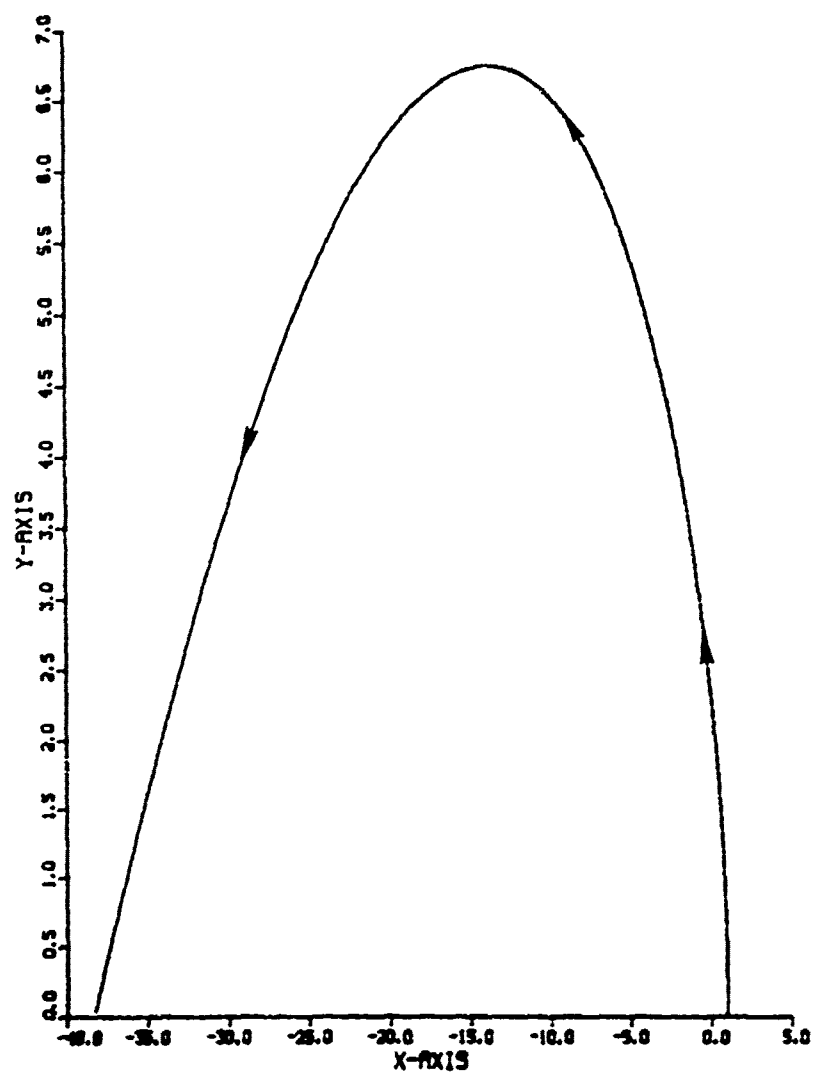


Figure 3.4. Unique particle trajectory from solution of equations. Electrons start on the $\phi = 0$ half plane (positive X-axis) at $X = 1.0$ and return to the $\phi = V$ half plane (negative X-axis) at $X = -38.2$. Note disparity in the X and Y axis scales.

Emission Current Density

For half-planes separated by an angle $\alpha = \pi$,
 $J(0) = 8.6 \times 10^{-3}$. Therefore

$$j_{HP} = 9.0 \times 10^{-8} \frac{V^{3/2}}{r_0^2} \quad (3.58)$$

where V is in volts, and j_{HP} will be in amps-cm^{-2} if r_0 is in cm. The parameter $J(0)$ has also been calculated as a function of α , the angle between half-planes, and the results are displayed in column 1 of Table 3.1. The radial distance from the origin at the end of the trajectory is given in column 2 of the same table.

The above results for emission current density are surprisingly close to a simple estimate obtained from the Child-Langmuir expression for space charge limited flow between parallel plates. If the distance between plates is d , the Child-Langmuir current density, j_{CL} , is

$$j_{CL} = \frac{1}{9\pi} \left(\frac{2e}{m}\right)^{1/2} \frac{V^{3/2}}{d^2} \quad (3.59)$$

If the distance d is estimated by $d = \alpha r_0$, we have

$$\frac{j_{HP}}{j_{CL}} = \frac{9}{2} J(0) \alpha^2 \quad (3.60)$$

The right hand side of Eq. (3.60) is given in column 3 in Table 3.1. As expected, the ratio approaches unity for small angles. At large angles, the ratio deviates surprisingly little from unity, even though an inspection of the final r values in column 2 indicates that the estimate $d = \alpha r_0$ is grossly in error. However, the space charge limiting is

certainly much less in the two-dimensional problem than in the Child-Langmuir case, apparently nearly compensating for the error in the estimate of d .

Table 3.1. Numerical Results for Space Charge Limited Flow Between Half Planes

α	<u>$J(0)$</u>	ξ	<u>j_{HP}/j_{CL}</u>
0.1	22.2	1.003	1.00
0.5	0.88	1.08	0.99
1.0	0.21	1.37	0.95
$\pi/2$	0.080	2.29	0.89
2.0	0.044	4.16	0.79
2.5	0.023	10.5	0.65
3.0	0.011	28.9	0.44
π	0.0086	38.2	0.38

α = angle between half planes in radians, $J(0)$ = unitless parameter determined from Eq. (6), ξ = distance of particle from origin, j_{HP}/j_{CL} = ratio of calculated current to an estimated current using the Child-Langmuir expression.

3.3 ANALYTIC SOLUTION FOR THE ELECTROSTATIC POTENTIAL OF A CHARGED DISK ON A GROUND PLANE

A more realistic, though less analytically tractable, case is that of the electrified disk of radius r_D , charged up to unit voltage, and surrounded by a grounded plane.

The potential upon neglecting space charge satisfies Laplace's equation. In cylindrical coordinates $\rho \equiv r/r_D$ and $z = Z/r_D$, we have:

$$\nabla^2 \phi(\rho, z) = 0 \quad z > 0 \quad (3.61)$$

$$\phi(\rho > 1, z=0) = 1 \quad (3.62)$$

$$\phi(\rho > 1, z=0) = 0 \quad (3.63)$$

The integral representation of the solution for (3.61-3.63) is known,^[8] i.e.,

$$\phi(\rho, z) = -\frac{2}{\pi} \operatorname{Im} \int_0^1 \frac{t dt}{\sqrt{1-t^2} \rho^2 + (z+it)^2}^{1/2} \quad (3.64)$$

Introducing the substitution $t = \sin\theta$, $\phi(\rho, z)$ is found to be

$$\phi(\rho, z) = \frac{2}{\pi} \int_0^{\pi/2} d\theta \frac{\sin\theta \sin\left(\frac{1}{2} \tan^{-1} \left(\frac{2z \sin\theta}{\rho^2 + z^2 - \sin^2\theta} \right)\right)}{\left[(\rho^2 + z^2 - \sin^2\theta)^2 + (2z \sin\theta)^2 \right]^{1/4}} \quad (3.65)$$

In Figure 3.5 we show a contour plot of $\phi(\rho, z)$. It is worth remarking that ϕ decays faster or as fast as $(\rho^2 + z^2)^{-1}$ and that the monopole and dipole moments of the induced charged density are zero. No higher order multipoles exist.

While this case is far more complex, it would be useful to study particle trajectories and space charge for both the cases of negatively charged dielectric on a ground plane, and for a positive interconnect. The delay in space charge limiting relative to the limiting time for an uncharged surface will provide a simple estimate of SGEMP enhancement.

PRE-CHARGE PROBLEM
ZMIN = .21135-03 ZMAX = .99785+00 A2 = .50000-01

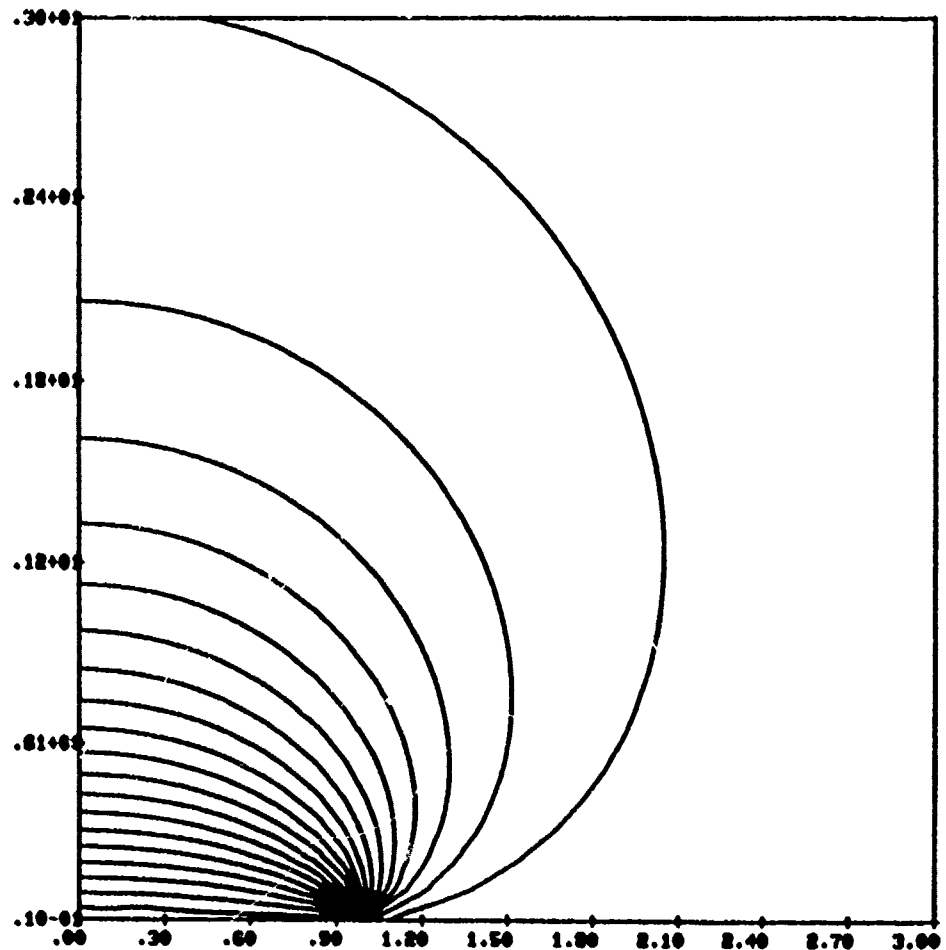


Figure 3.5. Potential contours for charged disk on grounded plane, calculated according to Eq. (3.65).

SECTION 4

A HYBRID ELECTROSTATIC/ELECTRODYNAMIC SGEMP COMPUTER CODE

4.1 WHY DEVELOP YET ANOTHER 2-D SGEMP CODE?

A major effort under this contract has been development of a new SGEMP code appropriate to spacecraft on test bodies having strong differential precharge. The special problem here is that electrostatic potentials vary rapidly in space on a scale of 1 cm or less. In fact, one would like to resolve layers of dielectric $\sim 10^{-2}$ cm thick. A standard SGEMP code with uniform 1 cm zoning would require 10^4 zones per square meter of mesh space, and a timestep ($\Delta t < \Delta x/c\sqrt{2}$) of $\sim 10^{-11}$ seconds. Yet the shortest time of interest is $\sim 10^{-9}$ seconds. Nonuniform zoning with otherwise standard techniques generates spurious electromagnetic noise everywhere, but especially at the irregular interfaces. A new approach was required to achieve a practical, generalizable method for this class of problem.

Our solution was to solve separately the conflicting parts of the problem, viz., high-resolution electrostatics coupled to coarse-resolution electrodynamics by the trajectories of emitted electrons. Separation of fields into electrostatic (longitudinal, curl-free) and electromagnetic (transverse, divergence-free) components is a well-known technique. For the problems of interest the longitudinal fields are the primary influence on the particle trajectories, while the transverse fields determine the SGEMP response.

In using this code to model the MRC test body, we resolved the fiberglass-paint dielectric layer with thickness 0.02 cm, had spatial zones in front of the surface with thickness 0.2 cm, and resolution as small as 1 cm along the

dielectric surface near the edge. (The latter could have been made still smaller without severely testing our storage restrictions.) The electrostatic grid is shown in Figure 4.1. The electromagnetic grid (Figure 4.2) had uniform 6.67 cm zones, and a timestep of 0.125×10^{-9} seconds was used. (Typically the electrostatic-particle portions of the code need be invoked only once every 2-8 timesteps.) Excellent results were obtained.

4.2 CODE DESCRIPTION

4.2.1 Mathematical Summary

The electrostatic portion of the code calculates the electrostatic potential, V , from

$$\nabla^2 V = -\rho/\epsilon_0 \quad (4.1)$$

and tracks particles in the electric field $\tilde{E}^T = \tilde{E}^T - \nabla V$. The electromagnetic code uses the particle information to generate a source current density, \tilde{J} , and timesteps

$$\epsilon_0 \frac{\partial \tilde{E}^T}{\partial \tilde{t}} = \left(\frac{1}{\mu_0} \nabla \tilde{X} \tilde{B} - \tilde{J} + \nabla \tilde{\psi} \right) \quad (4.2)$$

$$\frac{\partial \tilde{B}}{\partial \tilde{t}} = -\nabla \tilde{X} \tilde{E}^T \quad (4.3)$$

where $\tilde{\psi}$ is determined by requiring $\nabla \cdot \tilde{E}^T = 0$, or

$$-\nabla^2 \tilde{\psi} = \nabla \cdot \left(\frac{1}{\mu_0} \nabla \tilde{X} \tilde{B} - \tilde{J} \right) \quad (4.4)$$

subject to the same boundary conditions as V . Knowledge of \tilde{B} is then equivalent to knowledge of surface currents.

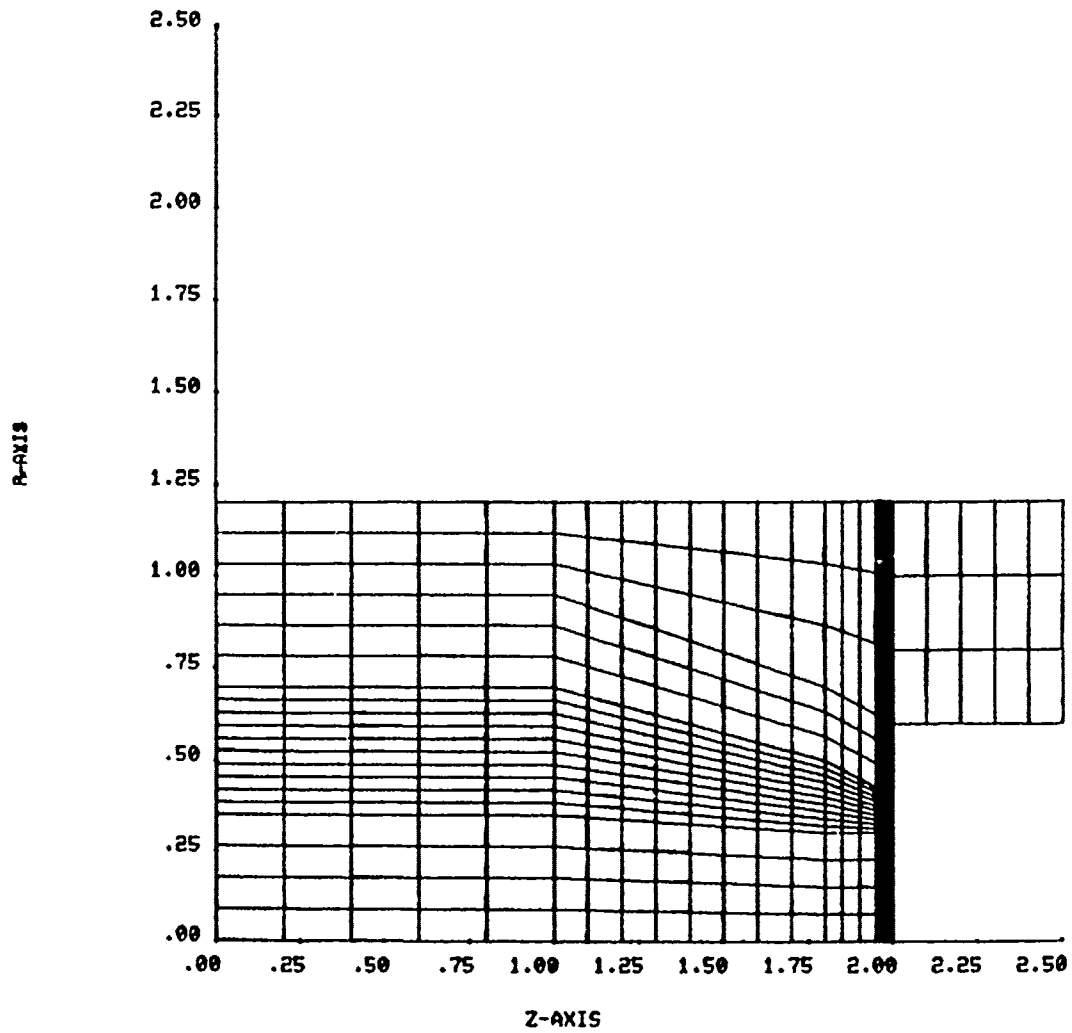


Figure 4.1. Electrostatic grid used for precharge-enhanced SGEMP/discharge calculations. Note fine resolution near dielectric-metal edge and in front of emitting surface.

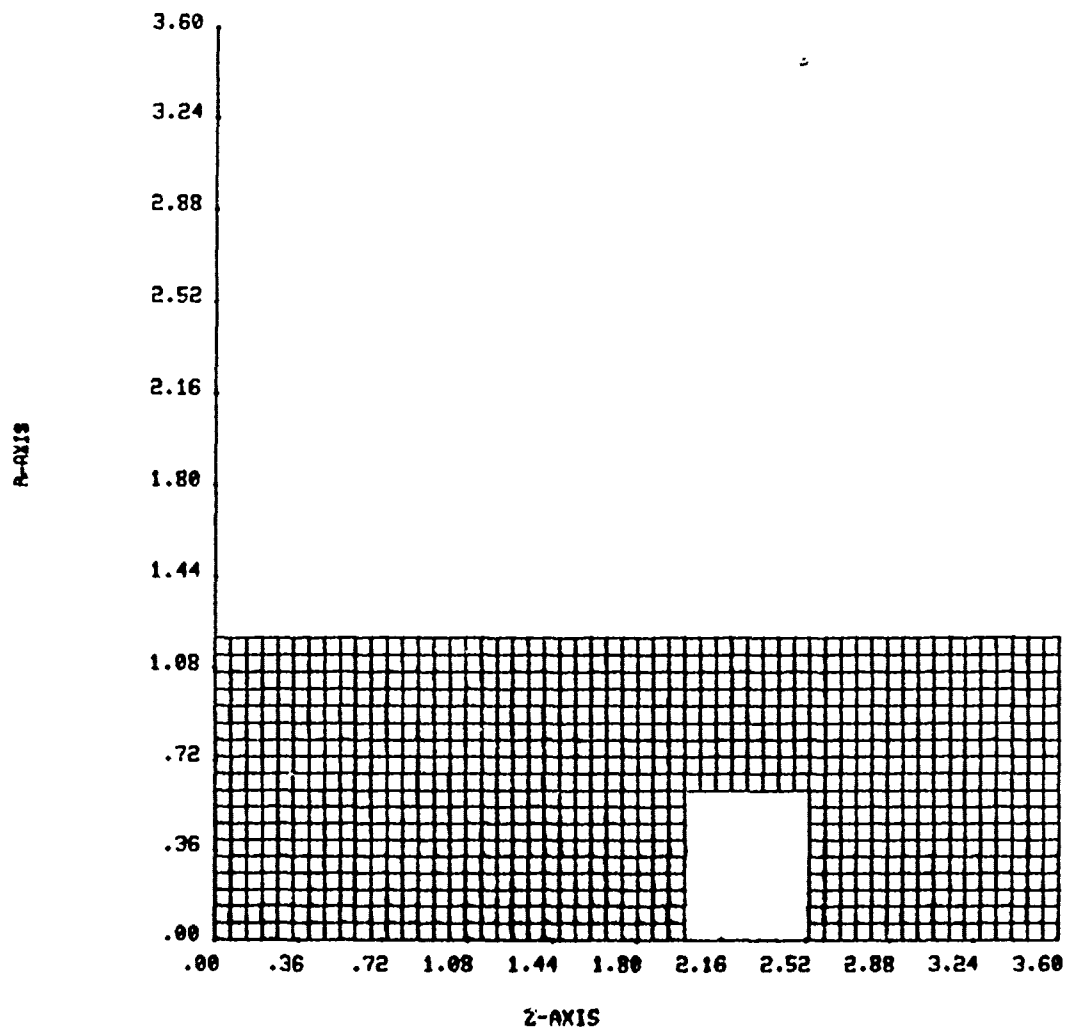


Figure 4.2. Grid used for electromagnetic part of precharge-enhanced SGEMP/discharge calculation. Note uniform zoning to minimize numerical noise and instability.

The centering for the electromagnetic code is shown in Figure 4.3. This centering has the advantages that currents and potentials are defined on the object surfaces, while electric fields are defined in space, making it easy to feed electromagnetic fields into the electrostatic code and track particles in the total field $\tilde{E} = \tilde{E}^T + \tilde{E}^L$. (For problems considered here, \tilde{E}^T is a small correction.) It is essential that the discrete representations of Laplacian, divergence, and gradient form a consistent set, so that $\nabla \cdot \tilde{E}^T$ exactly vanishes numerically. For this centering, it is not possible to construct a simple operator such that $\operatorname{div} \operatorname{curl} B$ vanishes identically. This problem is solved by inclusion of $\operatorname{curl} B$ in Eq. (4.4).

4.2.2 Code Structure

A block diagram of the hybrid code is shown in Figure 4.4. Note the use of the Incomplete Cholesky Conjugate Gradient (ICCG) ^[9] method to solve large sets of linear equations in both major code modules. It is the availability of this highly efficient algorithm that makes a code of this type possible.

The computational grids are generated using the MESHGEN ^[10] code. (This code has proved to be less than satisfactory. We expect that new mesh generators soon to be available will be substantial improvements.) The initialization phase uses the finite element technique to construct the Poisson's equation matrices, and converts the initial potential distribution to an initial charge distribution. Conducting objects and boundary nodes may be floating or held at fixed potential.

The electromagnetic and electrostatic/particle modules use ICCG and otherwise standard techniques to solve the equations described above. Each module maintains its own fast

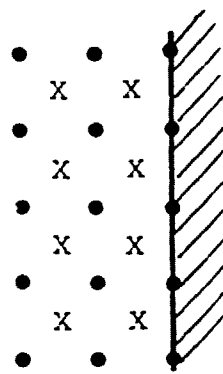


Figure 4.3. Centering scheme for transverse electromagnetic code. Scalar quantities (potential ψ , magnetic field B_ϕ , current divergence $\nabla \cdot \mathbf{J}$) are centered at solid points, while vector quantities (transverse electric field \mathbf{E} , current density \mathbf{J}) are centered at crosses.

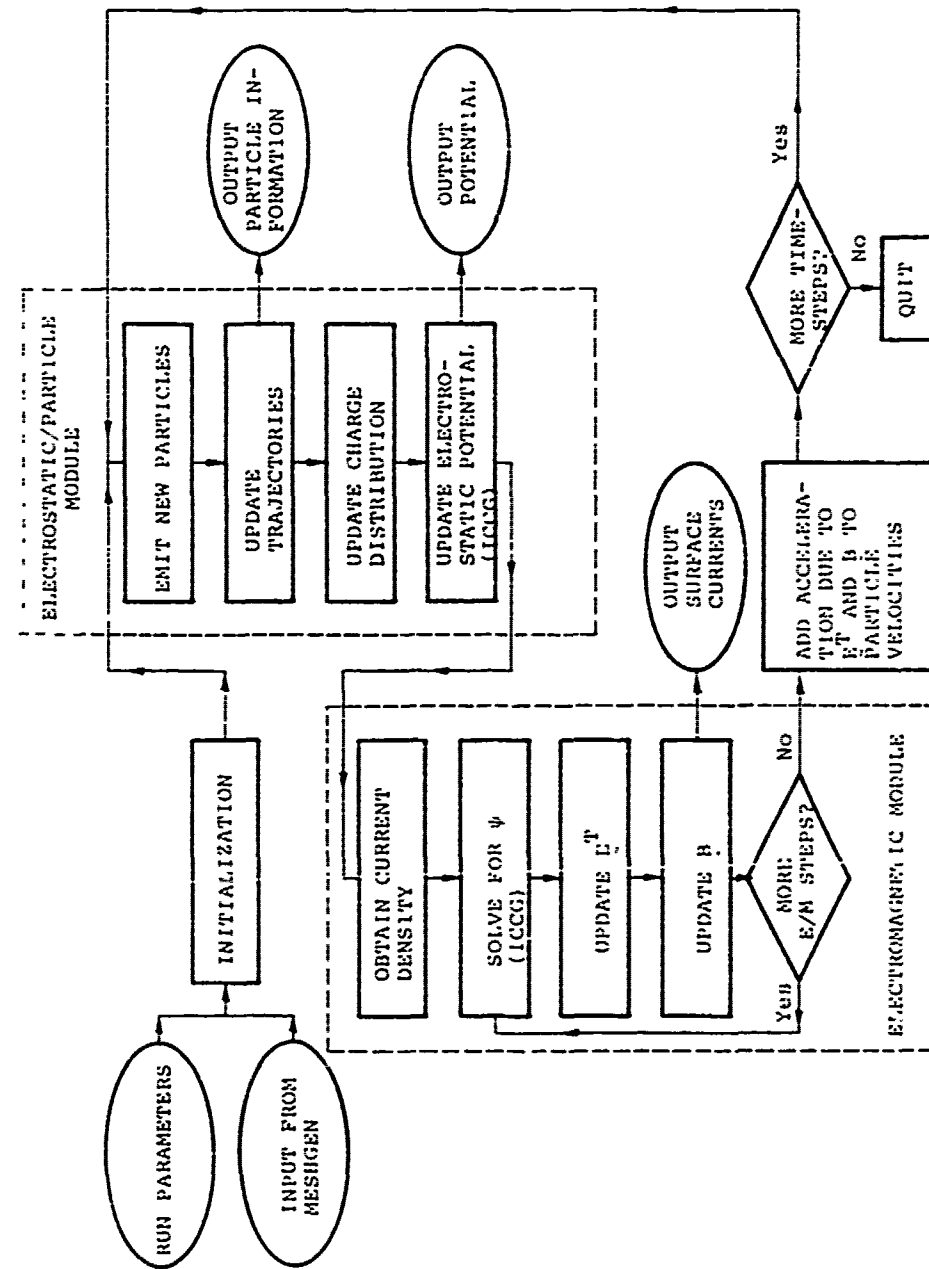


Figure 4.4. Block diagram of hybrid code.

random-access file in which mesh information, particle information, field information, etc. are stored. These files may be saved for later restarts or other investigations.

The code prints out electrostatic potential information periodically as requested. Particle information is stored on a disk file for later plotting of trajectories. Surface current information is both printed and stored for later processing.

4.3 SIMULATION OF SGEMP EXPERIMENTS

We used this newly-developed code to simulate experiments of the type performed by MRC. We chose not to attempt to reproduce any particular shot because the combined effects of poorly defined pulse shape and emission spectrum and the nonuniform precharge patterns would vitiate any agreement or lack thereof. Rather, we simulated generic shots to study the variation of response with electron energy and current in the general range of these experiments, and to develop simple estimates for the peak response.

Our first results were given in detail in our quarterly report of August 1979.^[11] In those calculations we emitted from the insulator a square pulse of 10 mA/cm^2 of electrons for $20 \times 10^{-9} \text{ sec}$, with an exponential spectrum of characteristic energy 300 eV. We found that the highest surface currents occurred at the edge of the emitting insulator, and that the peak values increased from $\sim 1.8 \text{ A/m}$ without precharge to $\sim 11 \text{ A/m}$ with the insulator differentially precharged to -10 kV , an enhancement of ~ 6 . Similar enhancements were observed elsewhere, e.g., on the back corner the response increased from $\sim 0.3 \text{ A/m}$ to $\sim 1.5 \text{ A/m}$.

While we were pleased with the agreement between our calculated surface currents and those measured by MRC, we were concerned that we predicted blowoff (i.e., final

potential of test body) far in excess of that measured. We predicted that the test body would rise to nearly 10 kV, rather than the 1-2 kV that was measured. The main reason for this difference was that our estimate of the capacitance of the test body to the tank (~ 75 pf) was far below MRC's value of 240 pf. The discrepancy was due in part to tank clutter and instrumentation, in part to our neglect of rear surface fields in the electrostatic grid (Figure 4.1), and in part because neglect of potential gradients along the surface caused excessive blowoff.

To do more highly resolved calculations we chose a baseline case as follows:

Pulse shape: square wave of width 2×10^{-8} sec

Voltage profile: $V(r) = V_0 J_0 (2.4 r/R)$ ($r < R$)

Emission current (J): 200 A/m^2

Electron spectrum (T): 30 eV exponential

Here J_0 is the ordinary Bessel function, and V_0 was chosen as -10 kV. V_0 , J , and T were varied. Zones of 0.2 cm immediately in front of the emitting surface were found to resolve the space charge layer nicely. Some results are shown in Table 4.1. Appendix B contains a selection of surface current response curves and particle trajectory plots.

The main conclusion to be drawn from Table 4.1 is that there is a well-defined limit for SGEMP response to low energy electrons under differentially precharged conditions. In this limit the response depends only weakly on the electron current density and spectrum, and strongly on the precharge potentials. Note also that both the surface currents and blowoff are in good agreement with MRC results.

Table 4.1. Results of SGEMP Calculations With Bessel Function Profile

Case	J (A/m ²)	T (eV)	V_o (volts)	Peak Surface Current (A/m)	Radius of Peak Current (cm)	Peak Current at Rear Corner (A/m)	Blowoff (μ C)
I	200	30	-10,000	8.4	25	0.8	0.272
II	200	120	-10,000	10.0	28	0.9	0.321
III	200	480	-10,000	13.0	30	1.3	0.426
IV	400	30	-10,000	9.5	27	0.75	0.286
V	400	30	-15,000	15.0	27	1.4	0.461

An instructive way of presenting the spatial dependence of the skin current beneath the insulator is as follows. A rough maximum is given by supposing that all current emitted within radius r [$\pi r^2 J$] is replaced by surface current across r [$2\pi r K$]. Thus we have

$$K_{\max}(r) = \frac{1}{2} r J . \quad (4.5)$$

The ratio K/K_{\max} is then indicative of the suppression of response due to space charge effects.

Figure 4.5 shows $K(r)/K_{\max}(r)$ for the cases run. Note the modest rise of the baseline curve (I) as the particle energy is increased by a factor of 16 (II, III), and the sharp drop as current increases by only a factor of 2 (IV). Increasing the potential (IV, V) markedly increases the efficiency of low energy electrons in producing a response.

An alternative means for studying the surface current spatial dependence is in terms of conductivity. Under this contract we developed a theory for the conductivity of a space charge layer (Appendix A). In this case there is a double layer of space charge, divided by the virtual cathode which forms above the emitting surface. The lower layer has a conductivity $\sigma_1 \approx 1 \times 10^{-5} T^{1/2}$. The upper is characterized by an energy $V_o J_o (2.4 r/R)$, and a lower coefficient due to having a unidirectional current: $\sigma_2 \approx 5 \times 10^{-6} [V_o J_o (2.4 r/R)]^{1/2}$. The surface current is the image of this conductivity current, and is thus given by

$$K(r) \approx (\sigma_1 + \sigma_2) |V_o| (2.4/R) J_1(2.4r/R) . \quad (4.6)$$

We found the computed peak currents could be approximated using the parameters

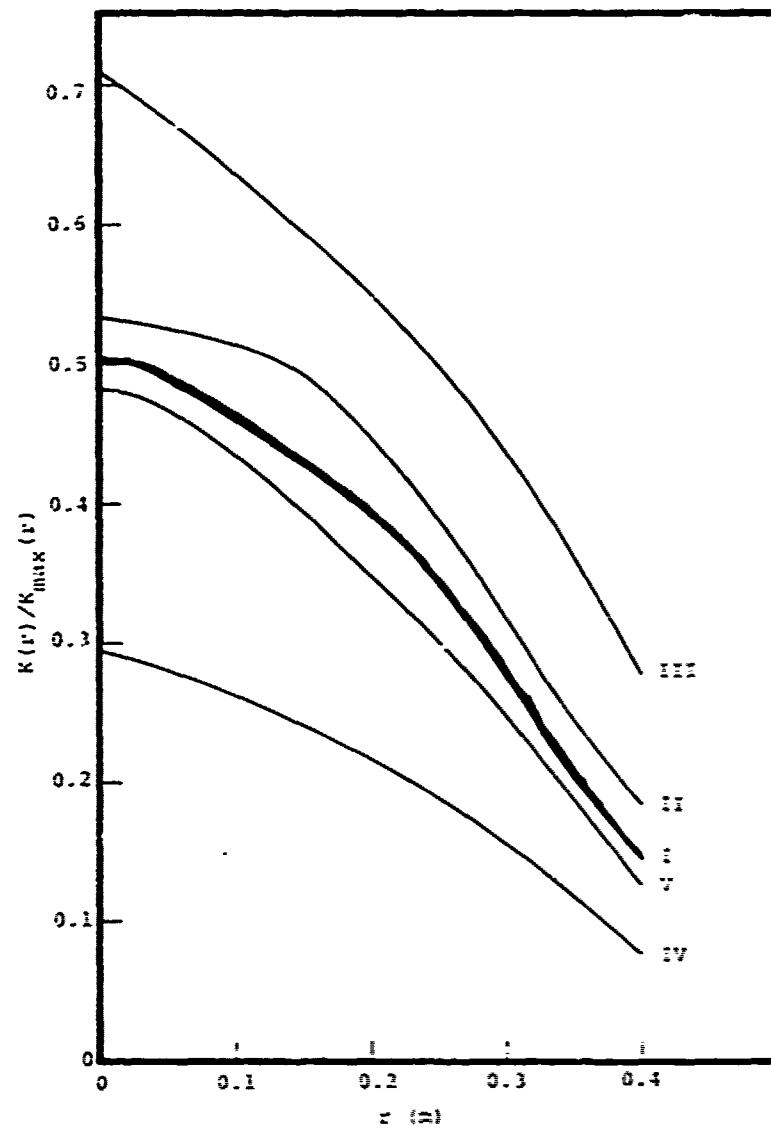


Figure 4.5. Relative surface currents (see Eq. 4.5) for the baseline precharge case (I), and the other cases as described in Table 4.1.

$$\sigma_1 = 8.2 \times 10^{-6} T^{1/2} \quad (4.7)$$

$$\sigma_2 = 3.27 \times 10^{-6} [V_o J_o (2.4 r/R)]^{1/2} .$$

These curves are shown in Figure 4.6. They reproduce well the peak heights and their variation with energy, and the outward movement of the peaks with increasing energy. They predict a peak at a somewhat smaller radius than the actual computer simulations.

4.4 SIMULATION OF SPACE CHARGE-LIMITED DISCHARGES

The SGEMP code described in the previous sections can readily be modified to simulate space charge-limited discharges. To do this we change the electron emission routine to emit that current of zero-kinetic-energy electrons which maintains a non-negative surface-normal electric field. This current is given by the Child-Langmuir law:

$$J = (4\epsilon_0/9) (2e/m)^{1/2} |E_z|^{3/2} / (\Delta z)^{1/2}$$

where Δz is the mesh spacing in front of the emitting surface, and E_z is the mean electric field across Δz (assumed electron repelling). Not only is this treatment applicable to discharges per se, but it is equally appropriate to cases in which x-rays cause a plethora of low energy electrons to be emitted from a precharged surface.

In connection with a theory of surface discharges, Section 5.6 presents some emission current results for the ERC geometry assuming

$$V(r) = V_o \left(1 - e^{(r/R)/\lambda} \right) / \left(1 - e^{-R/\lambda} \right)$$

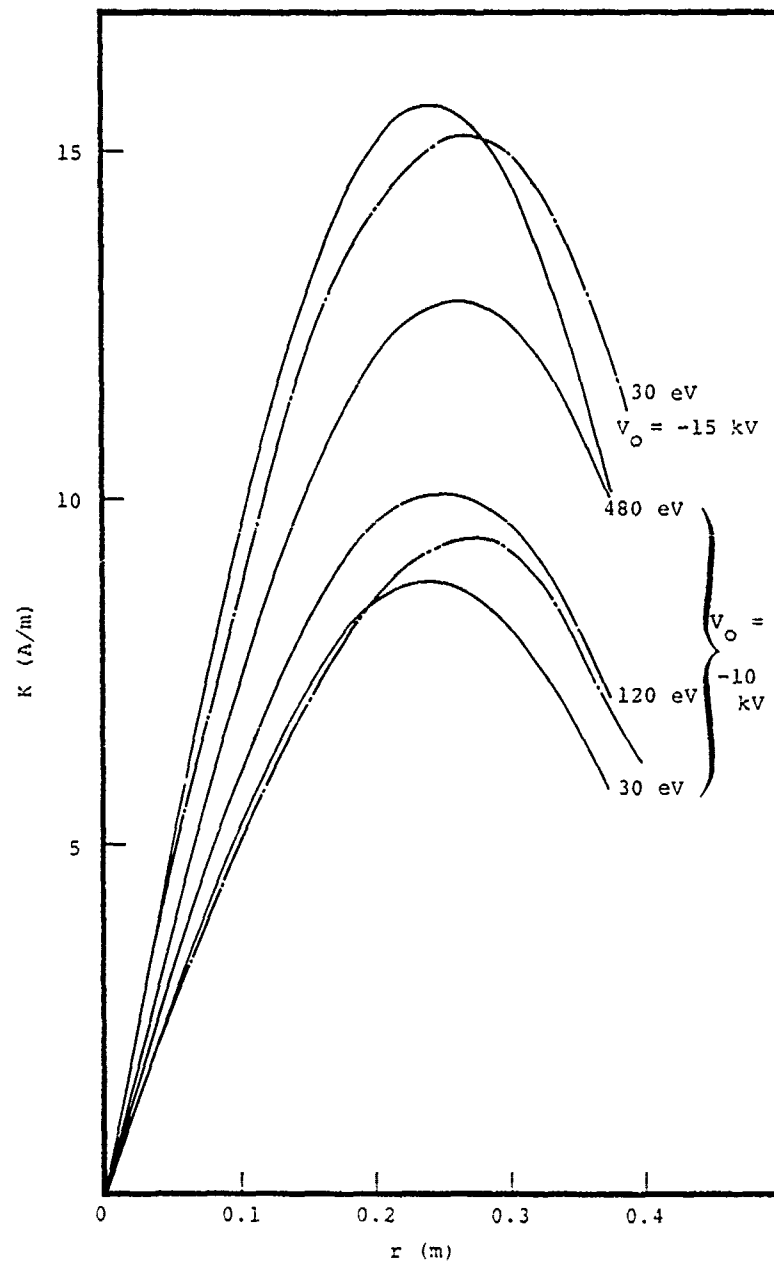


Figure 4.6. Predictions of peak SGEMP surface currents using Eqs. (4.6-4.7) (solid curves). Dot-dash curves are Cas's IV and V of Table 4.1.

where $V_0 = -15$ kV. Here we concentrate on the surface currents associated with such a discharge. Parameters characterizing this response are shown in Table 4.2. For the Bessel function case the response is similar to the SGEMP calculation, the latter giving higher surface currents due to non-negligible effects of a finite-energy emission spectrum. As the healing length parameter, λ , becomes short, the response rises markedly. Also, a new effect is seen, viz., a negative precursor in the surface current interior to the dielectric (Figure 4.7). This can be explained by examining Maxwell's equation

$$\nabla \times \mathbf{H} = \mathbf{J} + \epsilon_0 \frac{\partial}{\partial t} \mathbf{E} .$$

In this interior region the second term on the right, caused by increased emission at larger radii, initially dominates the first, causing the observed effect.

Table 4.2. Surface Current Response for Discharges

Voltage Profile ($V_O = -15$ kV)	$\lambda = .40$	J_O	$\lambda = .20$	$\lambda = .10$	$\lambda = .05$	$\lambda = .04$	$\lambda = .03$
Peak Current (A/m)	8.4	9.8	9.3	12.2	18.0	20.7	24.6
Radius of Peak Current (m)	0.24	0.24	0.30	0.34	0.40	0.40	0.40
Peak Surface Cur- rent at Rear Corner (A/m)	0.17	0.80	0.85	1.3	1.6	2.8	3.4
Negative Precursor (A/m) at $r = 0.20$ m	none	none	none	none	-1.8	-2.7	-3.8

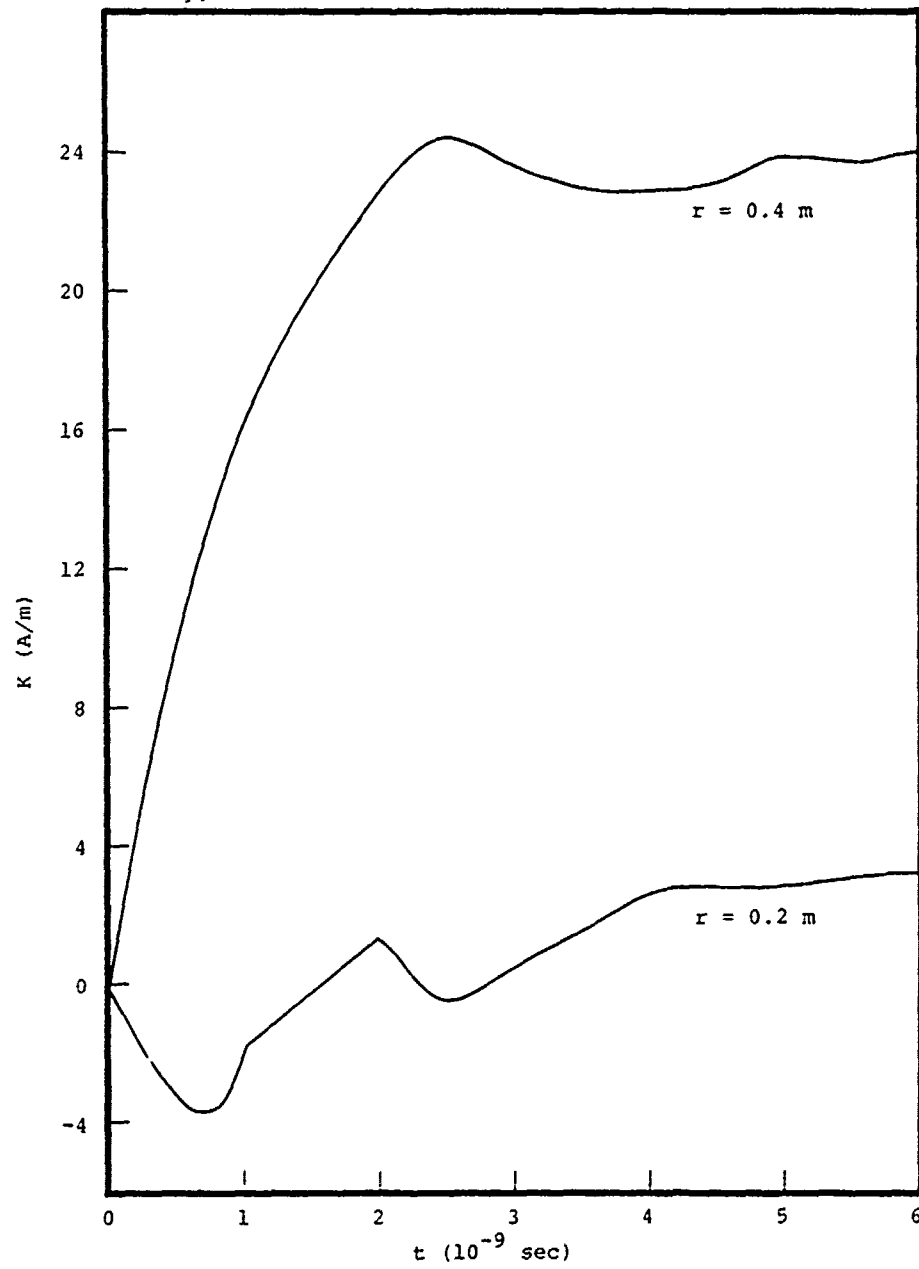


Figure 4.7. Surface currents versus time at $r = 0.4$ m and $r = 0.2$ m for discharge with $\lambda = 0.03$ m. Note negative precursor for small r .

SECTION 5

A THEORY OF DIELECTRIC SURFACE DISCHARGES*

There exists a large body of experimental data which measure peak blowoff currents from the discharges of space-craft dielectric materials. In order to predict how large surfaces behave, several researchers^[12-14] have measured how the peak blowoff currents scale with area. Attempts at a self-consistent theory to predict the observed scaling have all suffered from qualitative weaknesses^[15] and have not been successful quantitatively. In this section we present a simple model of surface charge emission which reproduces the observed area dependencies of surface discharge quite well. The model predicts spatial electron currents and therefore is useful in estimating induced surface currents for a wide variety of configurations. We make no attempt to analyze microscopic phenomena within charged dielectrics or to predict discharge thresholds. While limiting the overall scope of our model, the independence from internal dielectric microprocesses allows our theory, in principle, to be applicable to all good dielectrics, given only surface voltages prior to breakdown.

5.1 REVIEW OF THE DATA

Several researchers^[12-14,16] have exposed thin dielectric samples to electron beams which caused arcing. We shall focus on the area scaling experiments performed by Balmain.^[12] In these experiments circular Mylar samples were exposed to a 20 kV electron beam in a high vacuum tank. The samples were masked by grounded aluminum plates to minimize edge inhomogeneities. The beam density was of the order of 1 μ A per square centimeter. Balmain found that essentially all the

* For presentation at IEEE 1980 Nuclear and Space Radiation Effects Conference, Ithaca, NY, July 1980.

surface charge was blown off to the tank wall and could be measured as current to the grounded sample backing plate. The peak amplitude of this current scaled approximately as the area for small samples, $A \leq 0.1 \text{ cm}^2$, and as the square root of the area for large samples, $A > 1 \text{ cm}^2$. The tank walls were a minimum of about 15 cm from the sample. Currents observed ranged from 0.01 amperes to 100 amperes, with pulse durations 10-100 ns.

5.2 THE MODEL

The most striking feature of the discharge data was the magnitude of the observed currents. For the 1 square centimeter sample the current was 10 amperes. Given the distance between the sample and the tank wall, if the sample had been an isolated cathode, Child's law (one-dimensional space charge limited emission) would have predicted a maximum of 3×10^{-2} amperes. While neutralization of the electron space charge by an expanding surface plasma could allow high currents, the velocity of a plasma blowoff, $\sim 10^6 \text{ cm/sec}$, is far too slow to form a conducting channel within the observed pulse duration of a few hundredths to a tenth of a microsecond. In order to achieve the magnitude of the currents observed, it is apparent that most of the sample surface must participate in the discharge.

The model we propose relies on the edge potential gradients to enhance the space charge limited emission from the surface. We assume that some observed arc discharge occurs within the dielectric. This discharge produces enough radiation to trigger space charge limited emission simultaneously from the entire surface. The large magnitude of the ejected electron current results from the strong electric fields near the edge of the dielectric. Below we present a quantitative formulation which predicts both small and large limits and the transition between them. The model is, in principle, entirely predictive.

Before dealing with an actual experimental configuration, it is instructive to examine the space charge limited current emission between two semi-infinite conducting half planes (Figure 5.1). This problem has an analytical solution due to the absence of a scale length (see Section 3). The first result is that the density of emission current increases as the square of the distance to the edge

$$J \propto \frac{V^{3/2}}{x^2} \quad (5.1)$$

This corresponds to a strongly singular current near the edge. The implication for experiments is that if the voltage drops off at the edge of a sample on a scale small compared to the sample radius, then the emission near the edge will dominate the total emission. The circumference is then the important emitting region. It follows that the current is proportional to the square root of the sample area.

A second important result for the semi-infinite plane example is that particles travel a large distance parallel to the surface before being collected. A particle emitted a distance, d , from the edge of the cathode lands on the anode approximately $38 d$ from the edge. This implies that a small grounded mask will collect the charge emitted only from a tiny region of dielectric. Thus, most of the charge will travel to the vacuum tank walls.

The obvious drawback of the step function potential calculation is the singular total emission current. Certain other semi-infinite problems without scale length are solvable which yield bounded currents per unit edge length. However, they are not easily related to realistic cases. In Sections 5.3-5.5 we present a theoretical formulation for emission at an edge with a single scale length. Numerical methods must be used to predict actual current profiles. We found that

straightforward use of the hybrid SGEMP code described in Section 4 was the best tool for this purpose. Section 5.6 contains results for an emitting disk on a ground plane, which is a good model for comparison with experiment.

5.3 GENERAL DIMENSIONAL CONSIDERATIONS FOR SPACE CHARGE LIMITED EMISSION

We consider a general geometry with electrostatic potential

$$V(\underline{r}) = V_0 v(\underline{r}/\lambda) = V_0 v(\underline{z}) \quad (5.2)$$

where $V(\underline{r})$ is specified on the boundaries, some subset of which are capable of emitting electrons in space charge limited fashion, V_0 characterizes the magnitude of the potential, and λ characterizes the spatial variation of potential on the boundaries. The space charge density is given by

$$\rho(\underline{r}) = -\epsilon_0 \nabla^2 V(\underline{r}) = -(\epsilon_0 V_0 / \lambda^2) \nabla^2 v(\underline{z}) \quad (5.3)$$

and the current density by

$$\begin{aligned} \underline{j}(\underline{r}) &= \rho(\underline{r}) \underline{U}(\underline{r}) = -(\epsilon_0 V_0 / \lambda^2) \left(\frac{2eV_0}{m} \right)^{1/2} \underline{z} \nabla^2 v(\underline{z}) \\ &= \left(\frac{2e\epsilon_0^2}{m} \right)^{1/2} \frac{V_0^{3/2}}{\lambda^2} \underline{z} j(\underline{z}) \quad . \end{aligned} \quad (5.4)$$

Here we have assumed non-crossing particle orbits so that $\underline{U}(\underline{r})$ is a unique function of space, and we introduce

$$\tau = \left(\frac{2eV_0}{m\lambda^2} \right)^{1/2} t \quad (5.5)$$

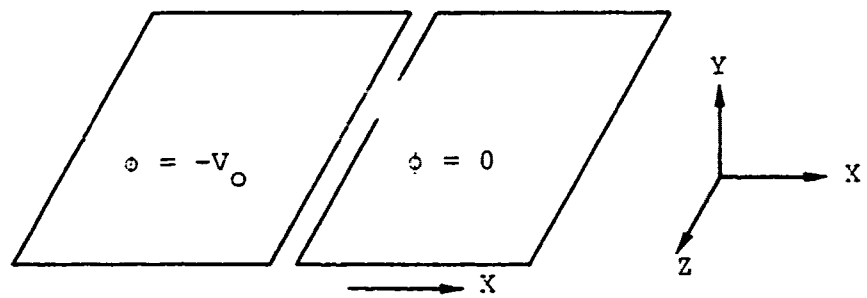


Figure 5.1. Edge is located at $x = 0$, $y = 0$ line.

and

$$\dot{\tilde{z}} = \frac{dz}{d\tau} \quad (5.6)$$

is the dimensionless particle velocity.

The above allows the entire problem to be reduced to dimensionless equations:

The steady-state requirement

$$\nabla \cdot j = 0 \quad (5.7a)$$

Poisson's equation

$$\nabla^2 v = +|j|/|\dot{z}| \quad (\text{assuming electron currents}) \quad (5.7b)$$

and the equation of motion

$$\ddot{\tilde{z}} = \frac{1}{2} \nabla v . \quad (5.7c)$$

These three equations, together with the boundary conditions and the scaling relations

$$v(\tilde{r}) = v_0 v(\tilde{r}/\lambda) \quad (5.8a)$$

$$j(\tilde{r}) = \left(\frac{2e\epsilon_0^2}{m} \right)^{1/2} \frac{v_0^{3/2}}{\lambda^2} j(r/\lambda) \quad (5.8b)$$

$$\rho(\tilde{r}) = - \frac{\epsilon_0 v_0}{\lambda^2} |j(r/\lambda)| / |\dot{z}(r/\lambda)| \quad (5.8c)$$

then permit a complete (numerical) solution of the problem.

5.4 PROBLEMS WITH NO LENGTH SCALE

We consider here a general class of problems relating to the breakdown near an edge. Suppose two semi-infinite planes intersect at angle θ_0 (Figure 5.2) and have potentials

$$V(\underline{r}) = V_0 (|\underline{r}|/\lambda)^\nu f_\nu(\theta) \quad (5.9a)$$

$$f_\nu(0) = 0 \quad (5.9b)$$

$$f_\nu(\theta_0) = 1 \quad (5.9c)$$

This problem can be seen to have no length scale because it is invariant to the transformation

$$\lambda \rightarrow \alpha \lambda \quad (5.10a)$$

$$V_0 \rightarrow \alpha^\nu V_0 \quad . \quad (5.10b)$$

Using this in (5.8b) gives

$$\underline{J}(\underline{r}) = \left(\frac{2e\varepsilon_0^2}{m} \right)^{1/2} \frac{|V_0|^{3/2}}{\lambda^2} \alpha^{3\nu/2-2} \underline{j}(\underline{r}/\alpha\lambda) \quad (5.11a)$$

or

$$\underline{J}(\underline{r}, \hat{\theta}) = \left(\frac{2e\varepsilon_0^2}{m} \right)^{1/2} \frac{|V_0|^{3/2}}{\lambda^2} \left(\frac{\underline{r}}{\lambda} \right)^{3\nu/2-2} \underline{j}(1, \hat{\theta}) \quad (5.11b)$$

or

$$\underline{J}(\underline{r}, \hat{\theta}) = \left(\frac{2e\varepsilon_0^2}{m} \right)^{1/2} \left(\frac{|V_0|}{\lambda^\nu} \right)^{3/2} r^{3\nu/2-2} \underline{j}(1, \hat{\theta}) \quad (5.11c)$$

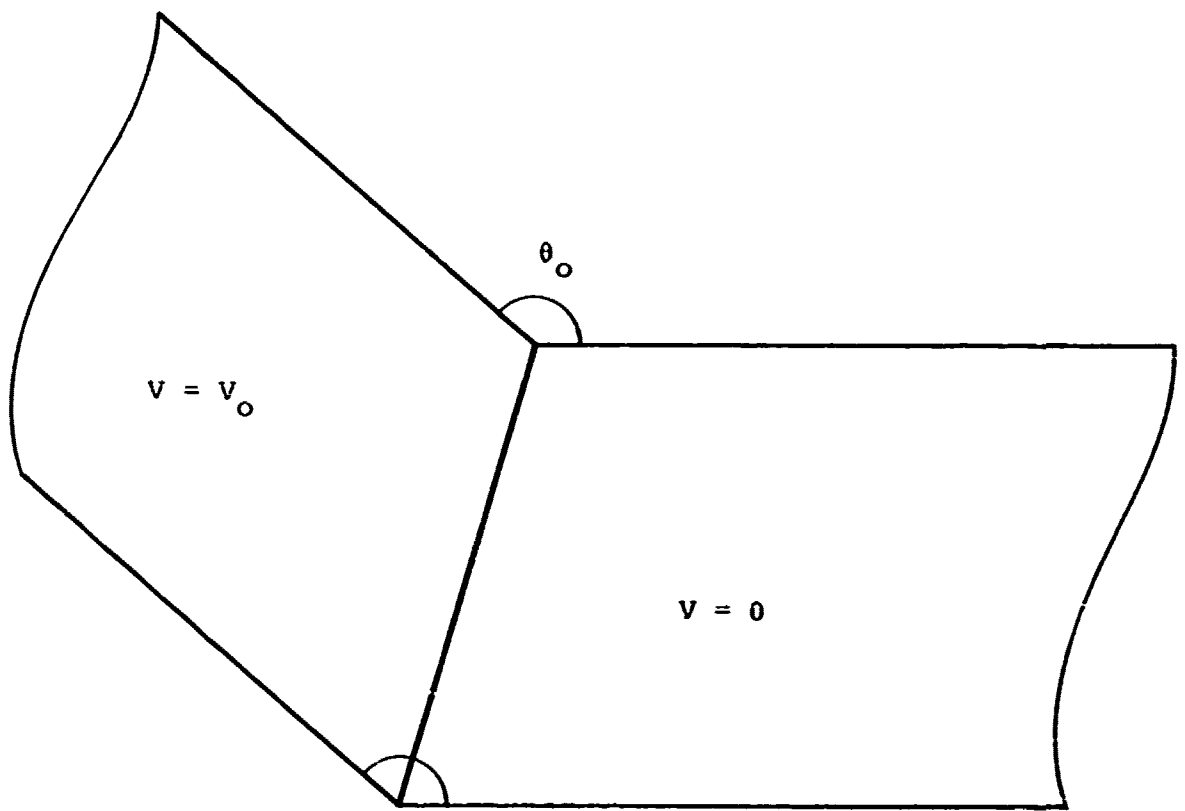


Figure 5.2. Two equipotential planes intersecting at angle θ_0 (Eq. 5.13).

In particular, for $v = 0$ (step function potential), the current at the emitting surface diverges as r^{-2} , a non-integrable singularity. The current density is given by

$$|J(r, v_0)| = \frac{4\epsilon_0}{9} \left(\frac{2e}{m}\right)^{1/2} \frac{g(\theta_0)}{\theta_0^2} \frac{v_0^{3/2}}{r^2} \quad (5.12)$$

with $g(\theta_0)$ given in Table 5.1. Also shown in Table 5.1 is the ratio of landing distance to takeoff distance, which goes to the fairly large value of 38 for $\theta_0 = \pi$.

For $v > 0$, $v_0 < 0$, an upper limit to the repelling field at the cathode (at θ_0) is provided by the Laplace solution

$$V = \frac{v_0}{\sin v_0} \left(\frac{r}{\lambda}\right)^v \sin v \quad (5.13)$$

Thus a requirement for non-zero emission is $\cos v_0 > 0$. For the plane problem ($\theta_0 = \pi$) we get non-zero emission for $v < 1/2$. However, from (5.15c) we see that an integrable emission current requires $v > 2/3$. Thus for $v_0 < 0$ the plane problem never leads to a convergent non-zero current.

For $v > 0$, $v_0 > 0$ the cathode ($\theta = 0$) field is always electron-repelling. However, for $\cos v_0 > 0$ the anode field is also electron repelling. We find that for $\theta_0 = \pi$, $v \geq 0.9$ the anode current collection density vanishes (i.e., electrons are accelerated to infinite r). Thus the class of "sensible" plane ($v_0 = \pi$) problems (i.e., integrable, non-zero current at both electrodes) requires $v_0 > 0$, and $2/3 < v \leq 0.9$.

Table 5.1. Emission Current Density (Relative to Child-Langmuir-like Value) and Anode Current Density Reduction Factor for Geometry of Figure 5.2 with Step-function Potential.

θ_o	$g(\theta_o)$	$R(\theta_o)$
0.1	1.0	1.003
0.5	1.0	1.08
1.0	0.95	1.37
$\pi/2$	0.90	2.29
2.0	0.81	4.16
2.5	0.63	10.5
3.0	0.45	28.9
π	0.38	38.2

θ_o = angle between half planes.

$g(\theta_o)$ = dimensionless parameter from Eq. (5.12) used to calculate space charge limited current between infinite half planes.

$R(\theta_o)$ = distance from origin of electrons striking anode when emitted from cathode at $R = 1.0$.

5.5 A CLASS OF PROBLEMS WITH ONE LENGTH SCALE

We consider a class of problems similar to the above, but require

$$\theta_0 = \pi \quad (5.14a)$$

$$v_0 < 0 \quad (5.14b)$$

$$v(r,0) = 0 \quad (5.14c)$$

$$v(r,\pi) = v_0(1 - e^{-r/\lambda}) \quad (5.14d)$$

or

$$= v_0 \tanh(r/\lambda) \quad (5.14e)$$

or

$$= \frac{2v_0}{\pi} \arctan\left(\frac{\pi r}{2\lambda}\right) \quad (5.14f)$$

or some similar function. For a point on the cathode $r \gg \lambda$, any problem of this class looks like the $v = 0$ (step function) problem of the preceding section, and thus has emission current $J \propto r^{-2}$. On the other hand, for $r \ll \lambda$ they all reduce to the $v = 1$ problem, and thus emit zero current. $J(r)$ thus has a maximum for $r \sim \lambda$. The value at this maximum can be far in excess of the value $g(\pi) v_0^{3/2} \lambda^{-2}$ inferred from (5.12), since the current is limited not by its own space charge (which is rapidly removed by the tangential electric field) but by space charge from the more weakly emitting region $r > \lambda$.

5.6 A PROBLEM WITH TWO LENGTH SCALES

In realistic problems there tend to be two scales of length: one characterizing the geometry and one characterizing the surface voltage profile near an edge. We consider in particular a charged dielectric disk of radius R on a ground plane. It is apparent the Eqs. (5.8a,b) must now be written

$$V(r) = V_0 v(r/\lambda; R/\lambda) \quad (5.15a)$$

$$J(r) = \left(\frac{2e\epsilon_0^2}{m} \right)^{1/2} \frac{V_0^{3/2}}{\lambda^2} j(r/\lambda; R/\lambda) . \quad (5.15b)$$

We can simplify (5.19b) by integrating over the disk surface:

$$I_{\text{tot}} = \int_0^R 2\pi r dr J(r) = 2\pi \left(\frac{2e\epsilon_0^2}{m} \right)^{1/2} V_0^{3/2} \int_0^{R/\lambda} j(z; R/\lambda) z dz \quad (5.16)$$

Written thus, it is manifestly clear that the total current is $V_0^{3/2}$ times a function of R/λ only.

We have used the self-consistent electromagnetic particle code described in Section 4 to simulate this problem for a disk with $R = 40$ cm and a potential of the form

$$V(r) = V_0 \frac{1 - e^{-(R-r)/\lambda}}{1 - e^{-R/\lambda}} . \quad (5.17)$$

This potential has a peak value V_0 at the center of a disk of radius R , and goes to zero at the edge with a scale length, λ .

$$\frac{dV}{dr} (r=R) = \frac{V_o}{\lambda} \frac{1}{(1 - e^{-R/\lambda})} \quad (5.18)$$

$$= \begin{cases} V_o/\lambda & R \gg \lambda \\ V_o/R & R \ll \lambda \end{cases} .$$

The parameter λ was varied from 3 cm to infinity (triangle potential). The results are shown in Figures 5.3-5.6. For $\lambda \ll R$, it is apparent from Figure 5.3 that the maximum current density is given by

$$J_{\max} (\lambda \ll R) \approx 2.45 \times 10^{-7} V_o^{3/2} / \lambda^2 \quad (5.19)$$

in keeping with Eq. (5.8b), and from Figure 5.6 that

$$I_{\text{tot}} \approx \left(6.5 \times 10^{-6} + 2.9 \times 10^{-6} \frac{R}{\lambda} \right) V_o^{3/2} \quad (5.20)$$

in keeping with Eq. (5.16). The current maximum occurs at $r_{\max} \approx R - 1.3\lambda$, and the emission vanishes at $r \approx R - \lambda/2$ in keeping with the ideas of subsection 5.5.

5.7 COMPARISON WITH EXPERIMENT

A simple comparison with experiment is presently not possible since the sample surface voltage profile just prior to discharge was not measured. We would hope that voltage profiles would become available soon. However, if we assume the analytical form of the potential in Eq. (5.17), then for any example there are only two physical parameters to be estimated: V_o and λ . Balmain's data extrapolate to 10^3 amps for a 1 m^2 area sample. If we assume $V_o = -15 \text{ kV}$, Eq. (5.20) gives $\lambda = 0.3 \text{ cm}$. To extrapolate to small samples we suppose

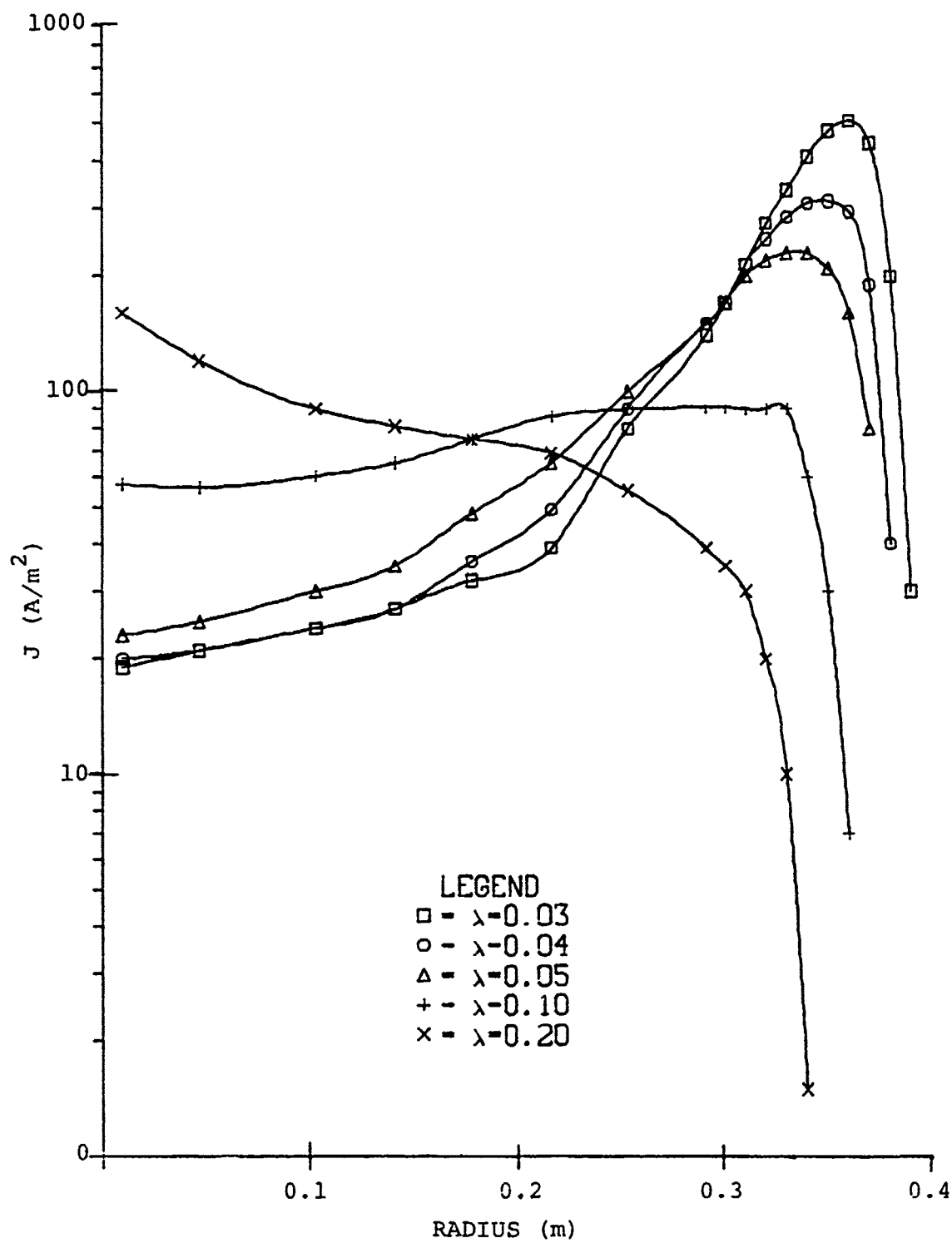


Figure 5.3. Current density versus radius for various values of healing length, λ , for a 0.40 meter radius disk charged to -15 kV.

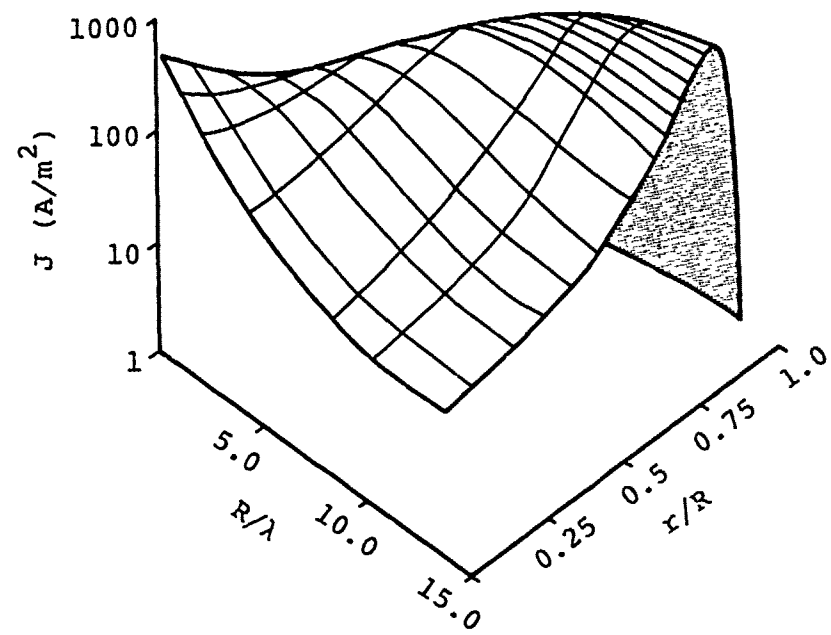


Figure 5.4. Emission current density (A/m^2) as a function of r/R and R/λ for $V_o = 15 \text{ kV}$.

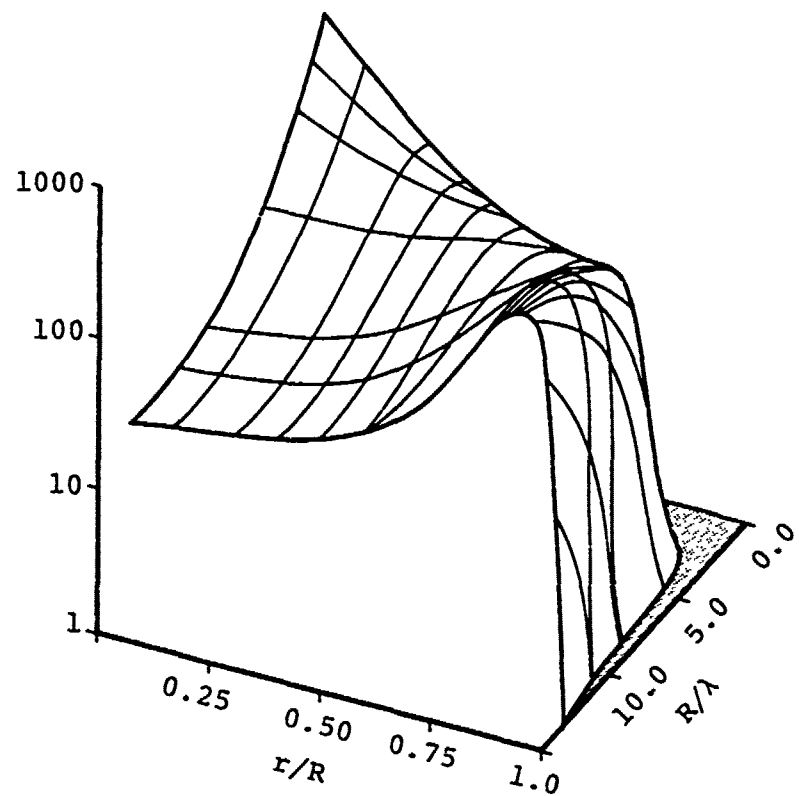


Figure 5.5. Emission current density (A/m^2) as a function of r/R and R/λ for $V_o = 15 \text{ kV}$.

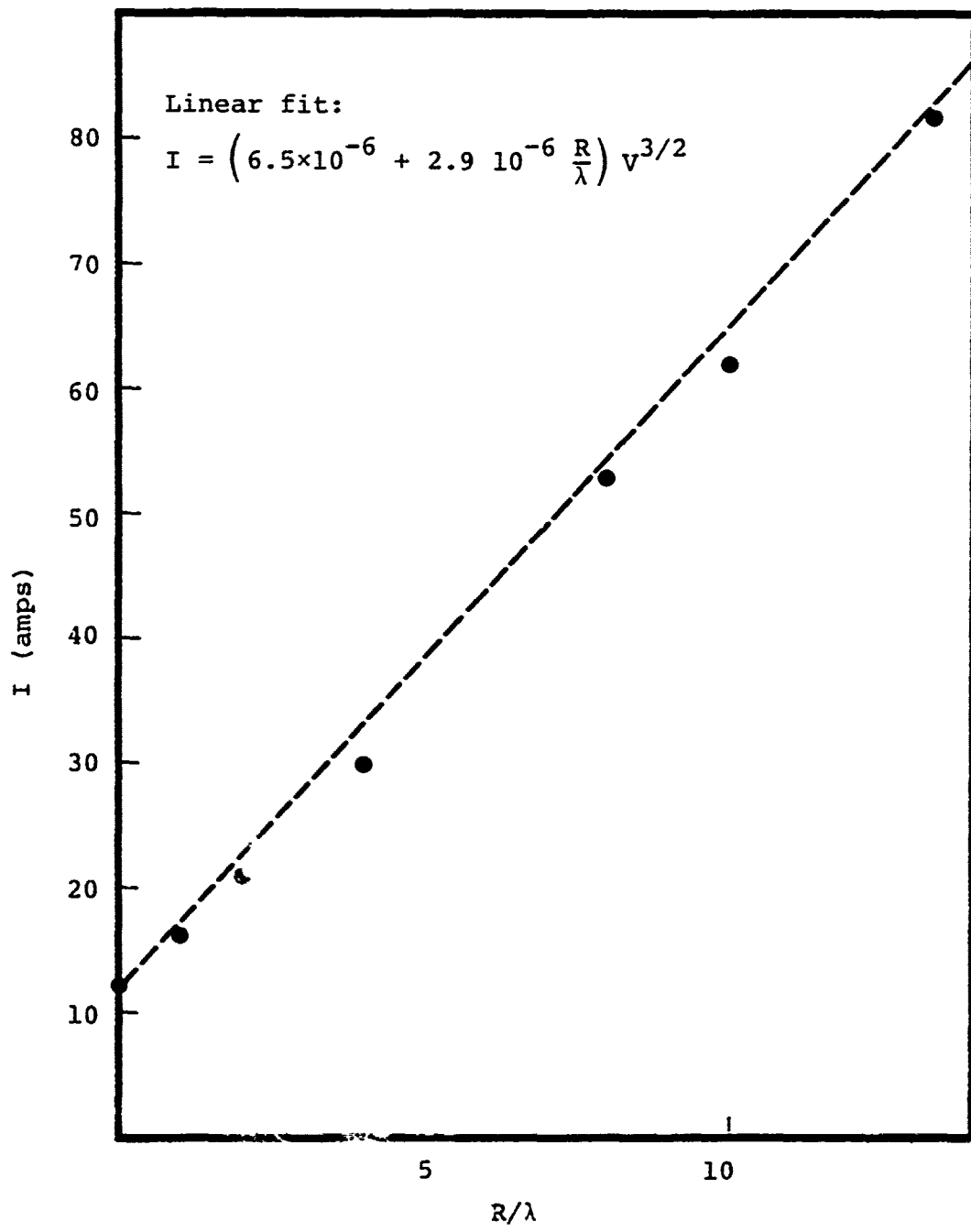


Figure 5.6. Total space charge limited emission current from disk having potential profile Eq. (5.2) with $V_0 = -15$ kV.

$$\left. \frac{dv}{dr} \right|_{r=R} = \text{constant} \quad (5.21)$$

$$\lambda = \text{constant}$$

at breakdown. Using the above data we find $dv/dr|_{r=R} = 5 \times 10^6$ V/m. The predictions of Eq. (5.17), (5.20), and (5.21) for the current, together with Balmain's peak current data^[12] are shown in Figure 5.7. We suggest that the discrepancies for the very small examples are due in part to the short pulse length, which was comparable to the inverse bandwidth of Balmain's experiment. For large samples $R/\lambda \gg 1$, Eq. (5.22) predicts $I \propto R/\lambda \propto A^{1/2}$. For small samples, Eq. (5.3) gives $V_o = R dv/dr$, so that

$$I \propto \left(R \frac{dv}{dr} \right)^{3/2} \propto A^{3/4} . \quad (5.22)$$

(If the blowoff is considered emission limited, we would have $I \propto A$.)

While this comparison involves fitting a parameter and assumed potential form, the asymptotic behavior and the magnitude agreement lend credence to the theory. Definitive tests performed with measured and well characterized voltage profiles would be a tremendous aid in evaluating the hypotheses.

5.8 CONCLUSION

We have presented a model for the "blowoff" of surface charge from a dielectric surface during discharge. This model successfully explains both the magnitude of charge release currents and how such currents scale with sample area. While the specific dielectric mechanisms which trigger discharges are not included, their absence makes the results generalizable to a wide range of materials.

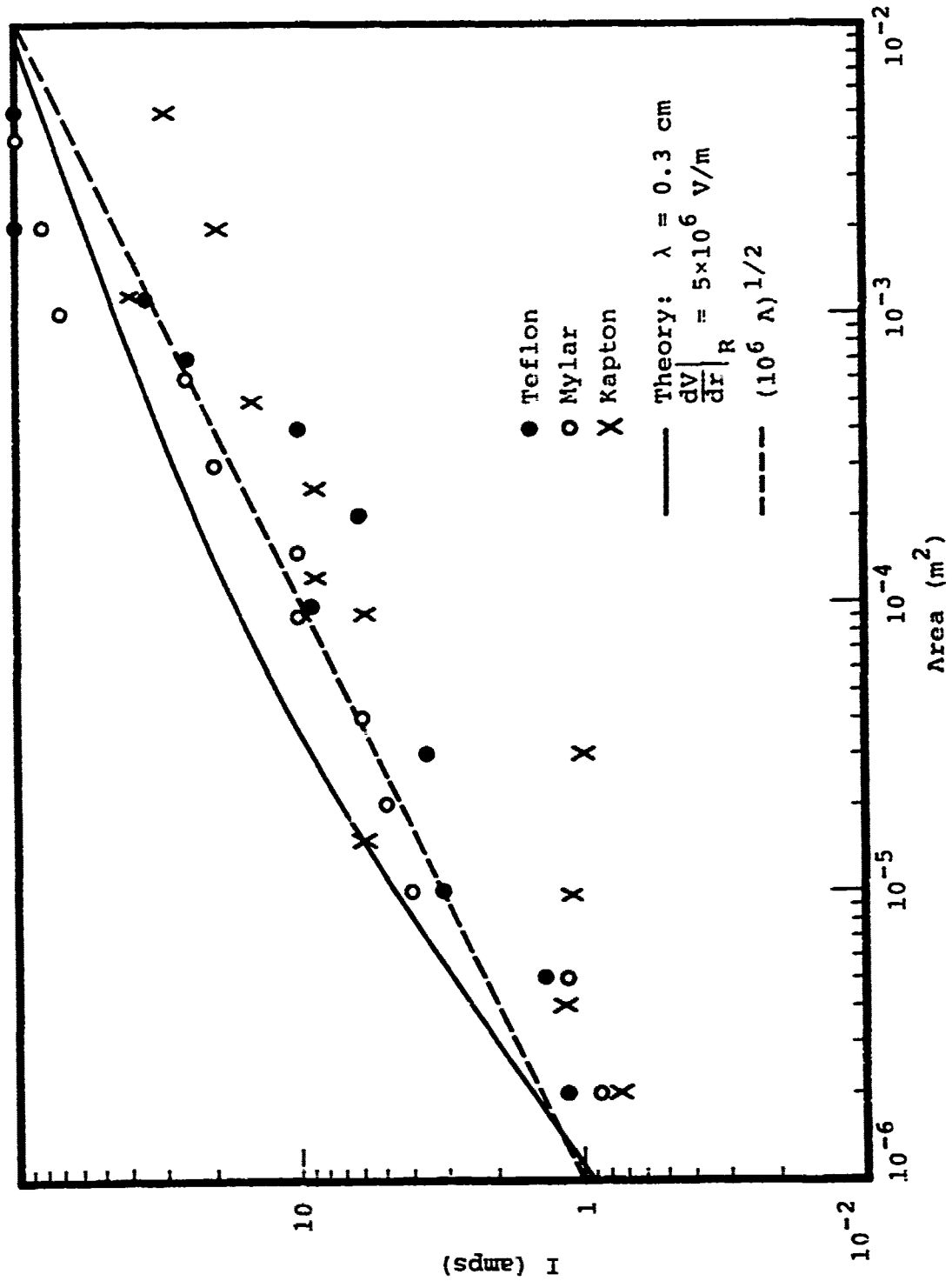


Figure 5.7. Emission current calculated using assumption (5.21) and Eq. (5.20), compared with data of Balmain (Reference 2).

One feature of the model is that the entire area simultaneously discharges. This accounts for the substantial loss of surface charge. The model accurately predicts the circumference dependence of discharge currents for moderately large samples. Extensions of the model to include finite return path impedance should account for observed impedance effects.

Finally, since emitted electron trajectories are calculated, the model predicts the effective electromagnetic driver of surface discharges. Using such a driver and SGEMP codes, one can (Section 4.4) predict the response of space-craft to electrostatic surface discharges.

REFERENCES

1. Spacecraft Charging Technology - 1978, NASA Conf. Publ. 2071, AFGL-TR-79-0082, 1979.
2. Bernstein, M. J. and J. A. Smith, "Primary and Secondary Electron Fields Induced by Soft X-rays," IEEE Trans. Nucl. Sci., NS-26, p. 4978, 1979.
3. Wilson, A., D. E. Parks and I. Katz, "Influence of Spacecraft Charging on SGEMP," Systems, Science and Software Topical Report SSS-R-78-3419, for Contract No. DNA001-76-C-0121, October 1977.
4. van Lint, V. A. J., D. A. Fromme and J. A. Rutherford, "Spontaneous Discharges and the Effect of Electron Charging on Skynet SGEMP Response," IEEE Trans. Nucl. Sci., NS-25, p. 1293, 1978.
5. Katz, I., J. J. Cassidy, M. J. Mandell, G. W. Schnuelle, P. G. Steen and J. C. Roche, "The Capabilities of the NASA Charging Analyzer Program," Reference 1, pp. 101-122.
6. Wenaas, E. P., R. H. Stahl and R. M. Wheeler, "SXTF RDT&E Description Conceptual Reference Design," JAYCOR Report 200-79-163/2066 for Contract DNA001-78-C-0102, 1979.
7. van Lint, V. A. J., B. C. Passenheim, R. Stettner and D. A. Fromme, "The Effect of Electron Precharging on the SGEMP Response of Insulators," IEEE Trans. Nucl. Sci., NS-26, p. 5024, 1979.
8. Sneddon, I. N., Mixed Boundary-Value Problems in Potential Theory, Amsterdam: North-Holland Publ. Co., New York: John Wiley and Sons, Inc., p. 211, 1966.
9. Kershaw, D. S., "The Incomplete Cholesky-Conjugate Gradient Method for the Iteration Solution of Systems of Linear Equations," J. Comp. Phys., 26, p. 43, 1978.
10. Egeberg, J. L., "MESHGEN - A Computer Code for Automatic Finite Element Mesh Generation," Sandia Laboratories SCL-DR-69-49, 1969.
11. Mandell, M. J., G. W. Schnuelle, P. G. Steen, E. M. Waisman and M. Rotenberg, "Precharge Enhanced SGEMP," Systems, Science and Software Quarterly Progress Report, SSS-R-79-4131, August 1979.

12. Balmain, K. G. and G. R. Dubois, "Surface Discharges on Teflon, Mylar and Kapton," IEEE Trans. Nucl. Sci., NS-26, p. 5146, 1979.
13. Flanagan, T. M., R. Denson, C. E. Mallon, M. J. Treadaway and E. P. Wenaas, "Effect of Laboratory Simulation Parameters on Spacecraft Dielectric Discharges," IEEE Trans. Nucl. Sci., NS-26, p. 5134, 1979.
14. Aron, P. R. and J. V. Staskus, "Area Scaling Investigations of Charging Phenomena," Reference 1, p. 485, 1978.
15. Leadon, R. and J. Wilkenfeld, "Model for Breakdown Process in Dielectric Discharges," Reference 1, p. 704, 1978.
16. Hazelton, R. C., R. J. Churchill and E. J. Yadlowsky, "Measurements of Particle Emission from Discharge Sites in Teflon Irradiated by High Energy Electron Beams," IEEE Trans. Nucl. Sci., NS-26, p. 5141, 1979.

APPENDIX A

MECHANISM FOR SGEMP-TRIGGERED SURFACE FLASHOVER

by

M. J. Mandell, A. R. Wilson, I. Katz, G. W. Schnuelle
Systems, Science and Software
M. Rotenberg
University of California, San Diego

Published in IEEE Transactions on Nuclear Science,
Volume NS-26, No. 6, pp. 5030-5034, December 1979.

MECHANISM FOR SGEMP-TRIGGERED SURFACE FLASHOVER*

M. J. Mandell, A. R. Wilson, I. Katz, G. W. Schnuelle
 Systems, Science and Software
 P. O. Box 1620, La Jolla, CA 92038

M. Rotenberg
 University of California, San Diego
 La Jolla, CA 92093

Summary

A mechanism for simultaneous flashover of an array of dielectric surfaces is proposed. The timescale and current level of the resultant discharge are evaluated, and consequences for SGEMP response are discussed.

Introduction

In this paper we examine how the discharge of thin dielectric surfaces can significantly enhance SGEMP response. The mechanism of discharge involved, viz. surface flashover, has not previously been discussed in the SGEMP context, although apparent SGEMP-triggered discharges were observed in tests on the Skynet qualification model.¹

The basic problems of SGEMP are the generation of electromagnetic energy in response to an x-ray pulse and coupling of this energy into the structure and circuitry of a spacecraft. Most studies have focused on electromagnetic signals produced directly by the 10^2 - 10^4 eV primary photoemitted electrons. Such signals are not independent of the initial state of the test object. Uniform negative precharging leads to a slightly enhanced response.² Substantial further enhancement due to differential precharging have previously been examined³ and effects of this type are currently under study.

Yet larger responses would result from release of stored electrical energy as a synergistic effect. Many common insulating spacecraft surfaces have capacitances C to ground of ~ 10 pf/cm². Differential charging of such a surface to $\phi = 10$ kV thus produces an energy density $\epsilon = \frac{1}{2} C\phi^2 = 5 \times 10^{-3}$ J/cm². For an incident x-ray fluence of this amount the electromagnetic energy density that can be created by primary photoelectrons is about a thousand times smaller (even less if the emission current is limited by space charge). Thus a discharge of insulating surface layers can lead to a substantial response even if it couples very inefficiently to electromagnetic energy.

The most rapid discharge of a substantial dielectric area would occur by surface flashover. By this, we mean that an electron layer forms just above the surface, causing it to become effectively conducting, i.e., capable of carrying large currents parallel to the surface. In this paper we address the questions: (1) If such a layer is formed, what

are the characteristics of the subsequent discharge? (2) Under what conditions might such a discharge be initiated by an x-ray pulse?

Surface Conductivity

Let us begin by addressing the question of the surface conductivity associated with a space charge layer. If an emitted electron returns to the surface after a time τ , it will travel along the surface with mean velocity $v = \frac{1}{2} e E_{\parallel} \tau$, where E_{\parallel} (assumed uniform) is the electric field parallel to the surface. Such a field results from non-uniformity of the precharging due, for example, to ambient surface conductivity near edges⁴ (see Figure 1). The area density of electrons above the surface emitted with energy between ϵ and $\epsilon + d\epsilon$ is $\frac{\partial j}{\partial \epsilon}(\epsilon) \tau^2(\epsilon) d\epsilon$. τ is a surface current

$$K_{\parallel} \left(\frac{A}{m} \right) = \frac{e}{2m} E_{\parallel} \int_0^{\infty} \frac{\partial j}{\partial \epsilon}(\epsilon) \tau^2(\epsilon) d\epsilon \quad (1)$$

is obtained, or, a surface conductivity

$$\sigma \left(\text{ohms}^{-1} \right) = \frac{e}{2m} \int_0^{\infty} \frac{\partial j}{\partial \epsilon}(\epsilon) \tau^2(\epsilon) d\epsilon. \quad (2)$$

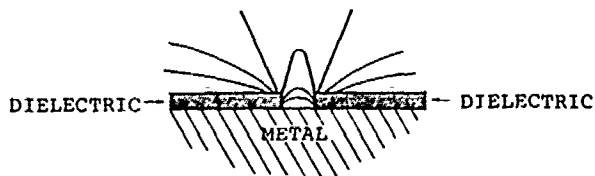


Figure 1. Schematic diagram of potential contours near edges of charged dielectrics. Reasonable value for potential gradient along dielectric surface might be 1 kV/mm, or 10^6 V/m.

We can evaluate this conductivity for either the monoenergetic (Child-Langmuir) case $j'(\epsilon) \sim \delta(\epsilon - \epsilon_1)$, or for the thermal case $j'(\epsilon) \sim e^{-\epsilon/T}$. (We neglect all initial transverse velocities.)

*This work supported by the Defense Nuclear Agency under Contract DNA001-79-C-0079.

For the monoenergetic case (see Appendix A) the flight time τ is given by

$$\tau(\text{sec}) = 1.09 \times 10^{-8} \epsilon^{1/4} J^{-1/2} \quad (3a)$$

and from Eq. (2) we obtain

$$\sigma(\text{ohms}^{-1}) = 1.05 \times 10^{-5} \epsilon^{1/2} \quad (3b)$$

where ϵ is emission energy (eV) and J is emission current (A/m^2). Note that σ is independent of J (although the conductivity will saturate if J is too small). Thus the surface resistivity of a monoenergetic space charge layer is $\sim 95 \text{ k}\Omega/\epsilon^{1/2}$.

For the thermal case we find (see Appendix B)

$$\begin{aligned} \tau(\epsilon) &= \left(\frac{2\pi m}{eT} \right)^{1/4} \left(\frac{\epsilon_0 T}{J} \right)^{1/2} \exp(\epsilon/2T) \\ &\times \text{erf}[(\epsilon/2T)^{1/2}] \end{aligned} \quad (4a)$$

$$\begin{aligned} &= 7.27 \times 10^{-9} T^{1/4} J^{-1/2} \exp(\epsilon/2T) \\ &\times \text{erf}[(\epsilon/2T)^{1/2}] \end{aligned} \quad (4b)$$

where T is the temperature (eV) and ϵ_0 the permittivity of free space.

To evaluate the conductivity we must insert into Eq. (2) a convergence factor $\exp(-\epsilon/T_c)$, reflecting the fact that very high energy electrons leave the influence of the transverse field. We then find

$$\begin{aligned} \sigma(\text{ohms}^{-1}) &= 4.6 \times 10^{-6} T^{1/2} \left(\frac{T_c}{T} \right) \\ &\times \left[\frac{4}{\pi} \left(\frac{T_c}{2T+T_c} \right)^{1/2} \arctan \left(\frac{T_c}{2T+T_c} \right)^{1/2} \right] \end{aligned} \quad (5)$$

(The quantity in square brackets becomes unity for $T_c \gg T$.)

Surface Diffusion Discharge

We turn now to the relationship between conductivity and discharge characteristics. The space charges and currents must satisfy the equation

$$\frac{\partial \rho}{\partial t} + \nabla \cdot j = 0. \quad (6)$$

Since there is negligible net current in the z -direction, the current divergence is entirely lateral — that is, parallel to the emitting surface. It is thus appropriate to define an areal charge density

$$q = \int \rho dz \quad (7)$$

and to integrate the current density j over the vertical extent of the space charge layer

$$K_{\parallel} = \int j dz. \quad (8)$$

This allows us to write

$$\frac{\partial q}{\partial t} + \nabla \cdot K_{\parallel} = 0. \quad (9)$$

The areal charge density can be considered as having two components

$$q = q_s + q_v \quad (10)$$

where q_s is the charge residing at the surface and q_v is the contribution in the space charge limited layer. Under conditions of SGEMP relevance the space charge limited current density is typically $J \gtrsim 10^{-2} \text{ A/cm}^2$ and corresponding flight times $\tau \sim 10^{-10}$ secs so that

$$\begin{aligned} q_v &\sim J \tau \\ &\sim 10^{-12} \text{ coulombs/cm}^2. \end{aligned}$$

By comparison, the surface charge, q_s , is much larger since, for a dielectric layer of thickness $d \sim 10^{-2} \text{ cm}$ the capacitance is

$$C = \frac{9 \times 10^{-14}}{d} \sim 10^{-11} \text{ farads/cm}^2.$$

Thus, the surface charge density is

$$\begin{aligned} q_s &= C \phi \\ &\sim 10^{-7} \text{ coulombs/cm}^2 \end{aligned} \quad (11)$$

if the surface is charged to 10 kV with respect to the underlying conducting surface. Inserting this expression for q and the relation implied by Eqs. (1) and (2), namely,

$$K_{\parallel} = \sigma E_{\parallel} = -\sigma \nabla \phi \quad (12)$$

into Eq. (9), we obtain

$$C \frac{\partial \phi}{\partial t} = \nabla \cdot (\sigma \nabla \phi)$$

$$\frac{C}{\sigma} \frac{\partial \phi}{\partial t} = \nabla^2 \phi. \quad (13)$$

(We neglect spatial dependence of the conductivity, which, in the treatment used here, is a function only of the electron emission spectrum.) The quantity C has the dimension of capacitance per unit area (farads/cm^2) and σ those of conductance (ohms^{-1}) so that the inverse diffusion coefficient C/σ has dimensions of time per unit area. The discharge time is then proportional to the sample area and inversely proportional to its thickness.

The solution to (13) for a 1 cm radius disk with $C/\sigma = 5 \times 10^{-7} \text{ sec/cm}^2$ is shown in Figure 2. These parameters are appropriate to a charged solar cell cover with a ground electrode along its edge. It is seen that the surface is about 20 percent discharged in 10^{-8} seconds. Simultaneous discharge of many such solar covers could produce a strong electromagnetic response.

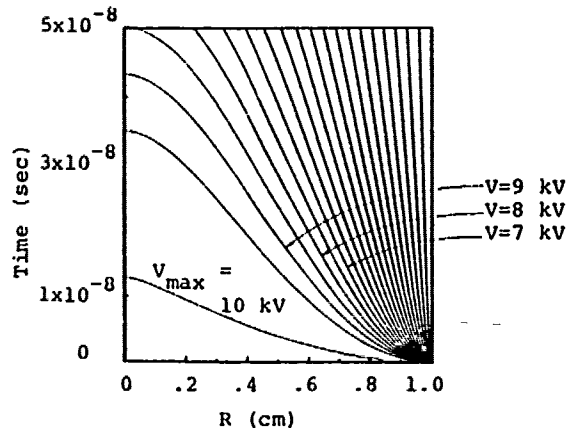


Figure 2. Contours of constant potential as functions of position and time.

Secondary Electron Avalanche

A discrepancy in the above mechanism appears when we examine the current level required for such a discharge. If a 10 pf/cm^2 surface at 10 kV is to discharge 20 percent in 10^{-8} sec, a net emission current density of 2 A/cm^2 is required. Since SGEMP photo-electron currents are much less than this, some current amplification mechanism is necessary. For such a mechanism we suggest a secondary electron avalanche, which was studied in a related context by Anderson.⁵ The basic idea is that electrons striking a surface with energy in the range $\sim 50-1000 \text{ eV}$ can liberate as many as ~ 20 low energy ($\sim 2 \text{ eV}$) secondary electrons. These secondaries can then be accelerated by the electric field parallel to the surface to continue the cascade.

To examine the plausibility of this mechanism, we return to Eq. (4b). Suppose an x-ray pulse produces electrons with $J = 10^2 \text{ A/m}^2$ and $T = 300 \text{ eV}$. (We do not mean to imply here that a thermal distribution

adequately represents an SGEMP electron emission spectrum. Our intent is simply to show that the high energy components of the spectrum space-charge-limit the low energy electrons in such a way that they may cause a secondary-electron avalanche.) Since $\text{erf}(x) \approx x$ for $x < 1$, the flight time of a 2 eV electron is

$$\tau \sim 7 \times 10^{-9} (2 \text{ eV})^{1/2} (300 \text{ eV})^{-1/4}$$

$$\cdot (100 \text{ A/m}^2)^{-1/2} (2)^{-1/2}$$

$$\sim 1.7 \times 10^{-10} \text{ sec.}$$

In a lateral field of $3 \times 10^5 \text{ V/m}$, it will hop a distance $(e/2m)E_{\parallel}^2 \tau^2 = 8 \times 10^{-4} \text{ m}$, and gain 240 eV of energy. (This field is appropriate near the edge of a small sample charged to 1 kV.) It will then, upon landing, produce $\sim 2-20$ secondary electrons. In fact, the x-ray produced current of low energy electrons is a substantial fraction of the total current, so that the emission current increases considerably with just one hop. The amplification will be reduced as the secondary electrons become limited by their own space charge. The steady-state emission current density is

$$J_{ss} \sim 1 \times 10^{-5} \epsilon^{1/2} E_{\parallel}^2 / \epsilon_s \quad (14)$$

where ϵ is the emission energy and ϵ_s is the energy for unit secondary production. For $\epsilon = 2 \text{ eV}$, $\epsilon_s = 30 \text{ eV}$, $E_{\parallel} = 3 \times 10^5 \text{ V/cm}$ we find $J_{ss} \sim 4 \text{ A/cm}^2$, far in excess of what is needed to sustain the discharge.

Conclusions

In conclusion, x-rays can trigger the simultaneous discharge of an array of small dielectric surfaces through the mechanism of secondary electron avalanche. The lateral electric field, resulting from the difference in potential between charged dielectric surfaces and an underlying conductor (e.g., as in solar panels - see Figure 1), provides the energy for the discharge. The SGEMP effect (driven by the displacement current) of these discharges will be greatest when the segments are at most a few cm^2 in area, and are differentially charged to 1-10 kV. The displacement current, $\partial E / \partial t$ will be proportional to the dielectric thickness. By way of comparison to SGEMP, the currents generated by such a breakdown are (see Eq. (3b))

$$K_{\parallel} = \sigma E_{\parallel} \sim 1 \times 10^{-5} \times 10^6 = 10 \text{ A/m}$$

for conditions where an electric field $E \sim 10^6 \text{ V/m}$ exists. This is an order of magnitude larger than the SGEMP surface current

response observed for fluence conditions ranging from 10^{-1} to 10^{-5} joules/cm².⁶

References

1. Van Lint, V.A.J., D. A. Fromme and R. Stettner, "Skynet Satellite Electron Pre-charging Experiments," *Spacecraft Charging Technology - 1978*, NASA Conference Publication 2071, AFGL-TR-79-0082.
2. Woods, A. J. and E. P. Wenaas, "Precharging Effects on the SGEMP Response," *IEEE Trans. Nuc. Sci.* NS-25, 1365 (1978).
3. Wilson, A., D. Parks and I. Katz, "Influence of Spacecraft Charging on SGEMP," *Systems, Science and Software Report SSS-R-78-3419* (October 1977) (to be published).
4. Rotenberg, M., M. J. Mandell and D. E. Parks, "Effects of Bulk and Surface Conductivity on the Potential Developed by Dielectrics Exposed to Electron Beams," to appear in *J. Appl. Phys.* (1979).
5. Anderson, R. A., "Mechanism of Fast Surface Flashover in Vacuum," *Appl. Phys. Lett.* 24, 54 (1974).
6. Wilson, A. and D. E. Parks, "Body Current Scaling Under High Fluence Conditions," *IEE Trans. Nuc. Sci.*, NS-23, 1916 (1976).

Appendix A Conductivity of Monoenergetic Space Charge Layer

The potential due to the space charge of electrons emitted normally and monoenergetically [energy ϵ (eV)] satisfies the equation

$$\frac{d^2\phi}{dz^2} = \frac{2J}{\epsilon_0 \sqrt{2e\phi/m}}. \quad (A.1)$$

A virtual cathode forms at a distance d from the surface, and (A.1) is subject to boundary conditions $\phi(0) = +\epsilon$, $\phi(d) = 0$, $\phi'(d) = 0$. Letting $k = 2/\epsilon_0 \sqrt{2e/m}$, we find

$$\phi = \left[\frac{3}{2} \sqrt{kJ} (d-z) \right]^{4/3} \quad (A.2)$$

$$d = \frac{2}{3} \epsilon^{3/4} (kJ)^{-1/2}. \quad (A.3)$$

The flight time is then given by

$$\tau = 2 \int_0^d \frac{dz}{\sqrt{\frac{2e}{m} \phi(z)}} = \epsilon^{1/4} J^{-1/2} \left(\frac{32m \epsilon_0^2}{e} \right)^{1/4} \quad (A.4)$$

$$\tau = 1.09 \times 10^{-8} \epsilon^{1/4} J^{-1/2}.$$

The transverse conductivity is then

$$\sigma = \frac{e}{2m} J \tau^2 = \epsilon^{1/2} \left(\frac{8e \epsilon_0^2}{m} \right)^{1/2} = 1.05 \times 10^{-5} \epsilon^{1/2} (\text{ohms}^{-1}) \quad (A.5)$$

Appendix B Conductivity of Thermal Space Charge Layer

Consider a surface emitting electrons with a total current J_0 (A/m²) and spectrum

$$\frac{\partial j}{\partial \epsilon} = -3 J_0 e^{-\beta \epsilon} \quad (B.1)$$

where $\epsilon = 1/2 mv_z^2$ is the normally directed energy component. We wish to calculate (1) the potential $\phi(z)$, subject to boundary conditions $\phi(0) = \phi'(\infty) = 0$; the flight time $\tau(\epsilon)$; and (3) the transverse conductivity.

The space charge density at z is composed of contributions from those electrons with sufficient energy to pass z :

$$\rho(z) = -2 \int_{-e\phi(z)}^{\infty} \frac{\partial j}{\partial \epsilon} [(2/m)(\epsilon + e\phi(z))]^{-1/2} d\epsilon. \quad (B.2)$$

Using (B.1) and integrating,

$$\rho(z) = - J_0 (2\pi m \beta)^{1/2} e^{\beta e \phi}. \quad (B.3)$$

The potential is then the solution of

$$\frac{d^2\phi}{dz^2} = - \rho/\epsilon_0 = \frac{J_0}{\epsilon_0} (2\pi m \beta)^{1/2} e^{\beta e \phi} \quad (B.4)$$

subject to the above boundary conditions. This solution is

$$\phi = - \frac{2}{5e} \ln \left(1 + \frac{z/z_0}{\sqrt{2}} \right) \quad (B.5)$$

where

$$z_0 = \left[\frac{8e J_0}{\epsilon_0} \sqrt{2\pi m \beta} \right]^{1/2}. \quad (B.6)$$

Inversely,

$$z(\phi)/z_0 = \sqrt{2} [e^{-\beta e \phi/2} - 1]. \quad (B.7)$$

The flight time τ is given by

$$\tau(\epsilon) = 2 \int_0^{z(-\epsilon/e)} [(2/m)(\epsilon + e\phi(z))]^{-1/2} dz \quad (B.8)$$

$$\tau(\epsilon) = \left(\frac{e}{e J_0} \right)^{1/2} \left(\frac{2\pi m}{B} \right)^{1/4} e^{\beta\epsilon/2} \operatorname{erf} \left(\sqrt{\frac{B\epsilon}{2}} \right) \quad (B.9)$$

$$\tau(\epsilon) = 7.27 \times 10^{-9} T^{1/4} J_0^{-1/2} e^{-\epsilon/2T} \operatorname{erf} \left(\sqrt{\frac{\epsilon}{2T}} \right) \quad (B.10)$$

where τ is in seconds, T in eV, and J_0 in A/m^2 .

The transverse current is given by

$$K_{\parallel} = \frac{e}{2m} \int_0^{\infty} \frac{\partial j}{\partial \epsilon} \tau^2(\epsilon) E_{\text{eff}}(\epsilon) d\epsilon. \quad (B.11)$$

Here we must take into account the fact that very high energy electrons leave the region of the transverse field, and should be given reduced weight in calculating transverse current. To achieve a simple, one-parameter model we take

$$E_{\text{eff}}(\epsilon) = E_{\parallel} e^{-\epsilon/T_c}. \quad (B.12)$$

(A better defined approximation would be to treat explicitly the dependence of transverse field on height. We reserve such a treatment for future work.) Equations (B.1), (B.9), (B.11), and (B.12) then give

$$\sigma = \epsilon_0 (\pi/2m)^{1/2} \int_0^{\infty} e^{-\epsilon/T_c} \operatorname{erf}^2 \left(\sqrt{\frac{\epsilon}{2T}} \right) d\epsilon \quad (B.13)$$

or

$$\sigma = 4.65 \times 10^{-6} T^{1/2} \left(\frac{T_c}{T} \right) \times \left[\frac{4}{\pi} \left(\frac{T_c}{2T+T_c} \right)^{1/2} \arctan \left(\frac{T_c}{2T+T_c} \right)^{1/2} \right] \text{ohms}^{-1}. \quad (B.14)$$

APPENDIX B

RESULTS FOR SGEMP (BESSEL FUNCTION PROFILE) CALCULATIONS

We present here particle trajectory plots and surface current plots for the five SGEMP cases of Table 4.1. The particle trajectory plots are "open shutter" pictures of electron tracks. Note the substantial amount of charge accelerated radially outward by the surface precharge fields. There is also a substantial current layer of space charge-limited electrons along the front surface extending beyond the edge of the dielectric. No electrons were seen to hit the side or rear of the test body, though a few may do so later in time.

Surface current plots are presented from four representative surface nodes (see Figure B.1). Node 398 has the peak response for this voltage profile. Node 400 is at the edge of the dielectric. Node 403 at the front corner and node 314 at the rear corner give a measure of the electromagnetically propagating response likely to be picked up by antennas or to penetrate through apertures. (The surface currents have been filtered to remove high frequency numerical noise.)

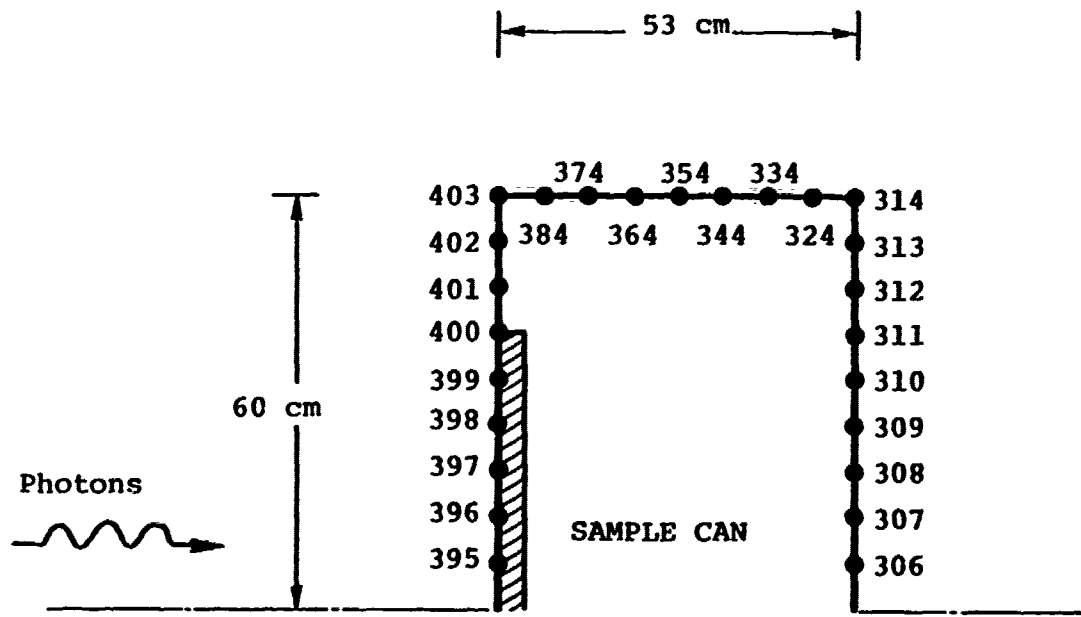


Figure B.1. Location of B-field (surface current) node points in computer model of differentially precharged SGEMP experiment.

CASE I

$V_o = -10 \text{ kV}$

$T = 30 \text{ eV}$

$J = 200 \text{ A/m}^2$

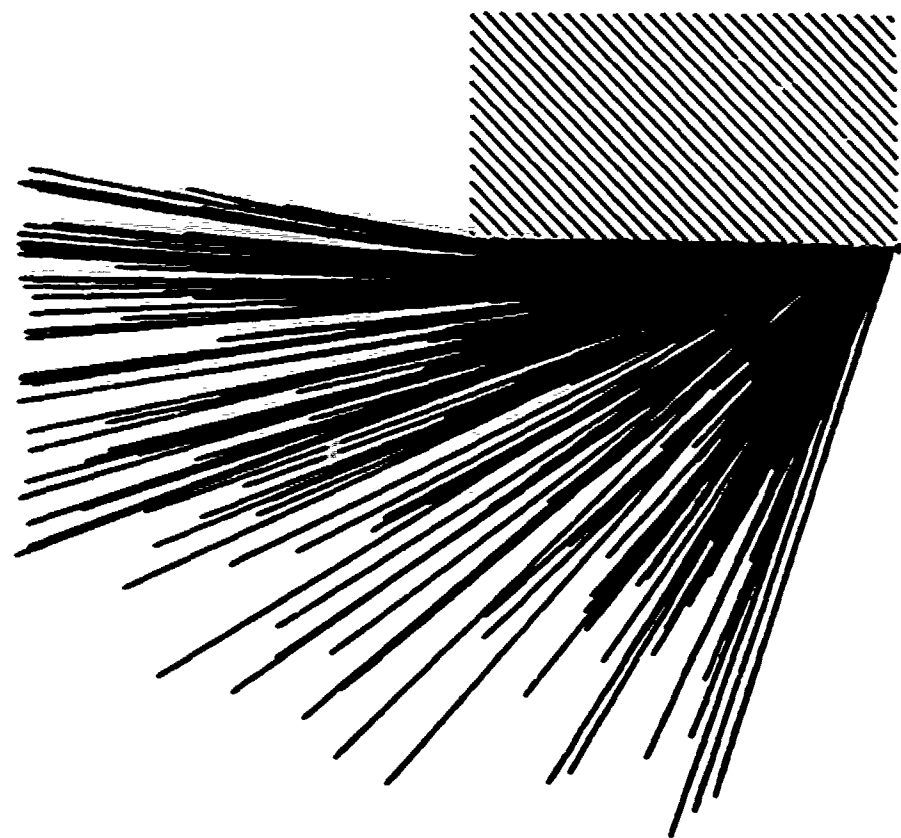


Figure B.2. Particle trajectories, Case I.

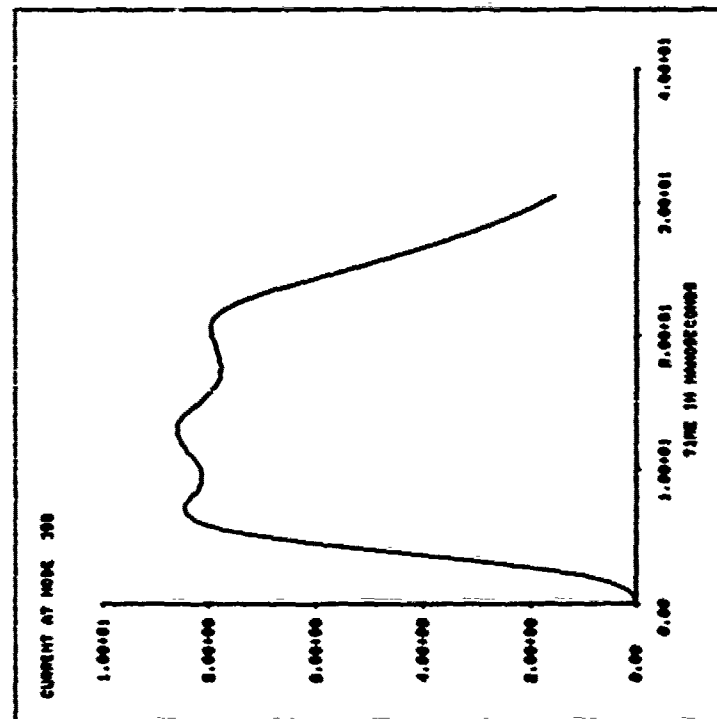
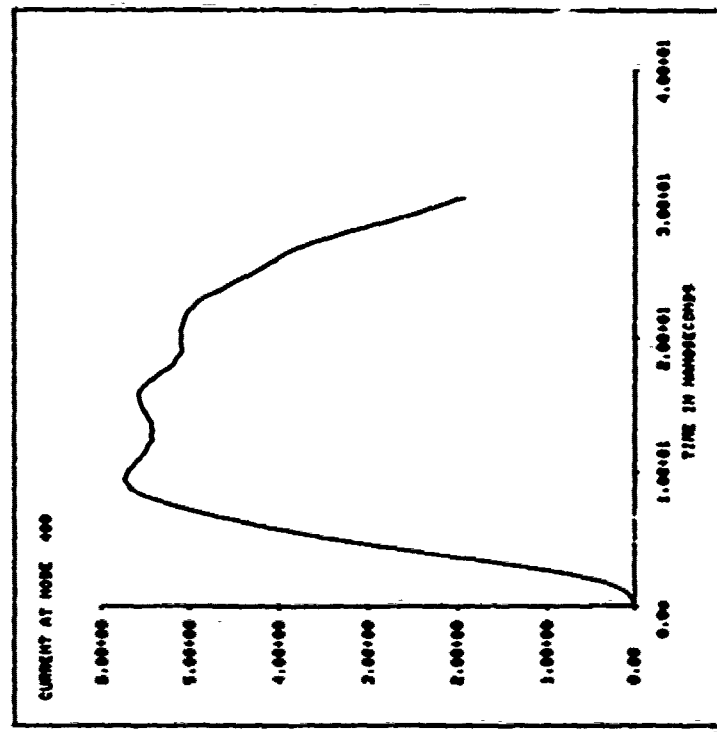


Figure B.3a,b. Surface currents, case I.

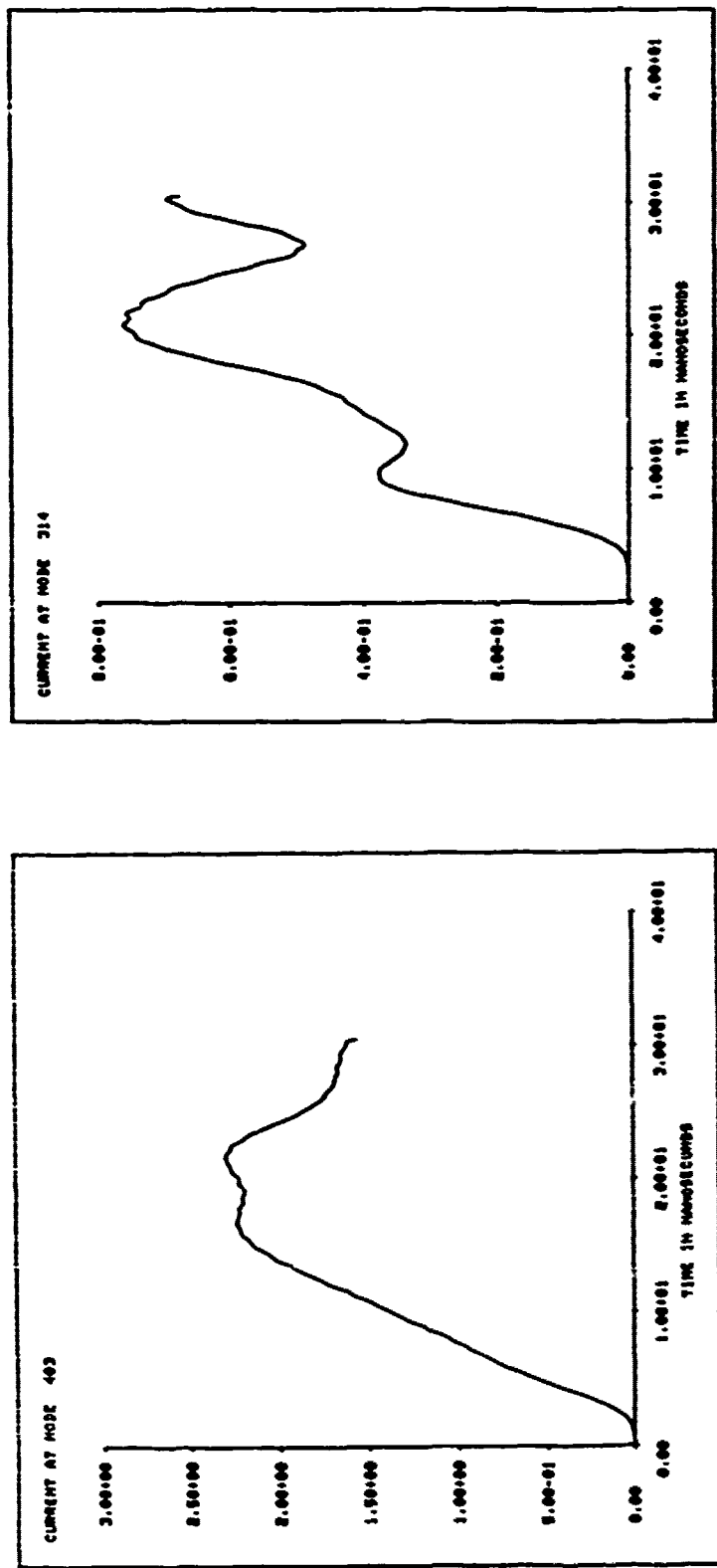


Figure B.3c,d. Surface currents, case I.

CASE II

$V_o = -10$ kV

$T = 120$ eV

$J = 200$ A/m²

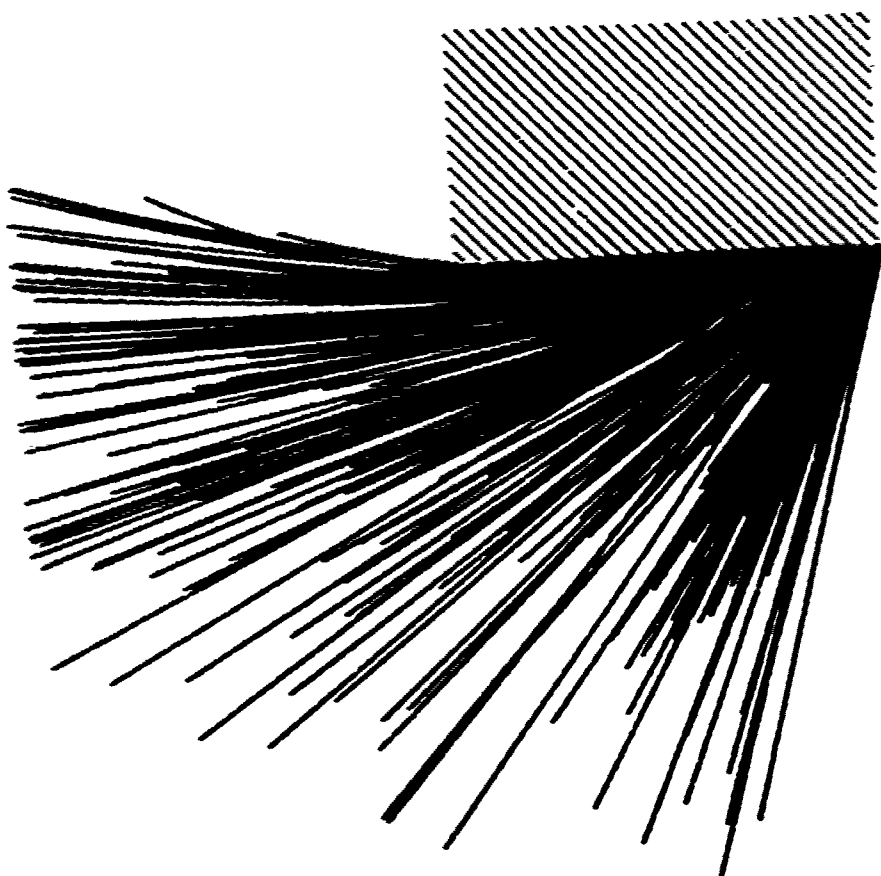


Figure B.4. particle trajectories, Case II.

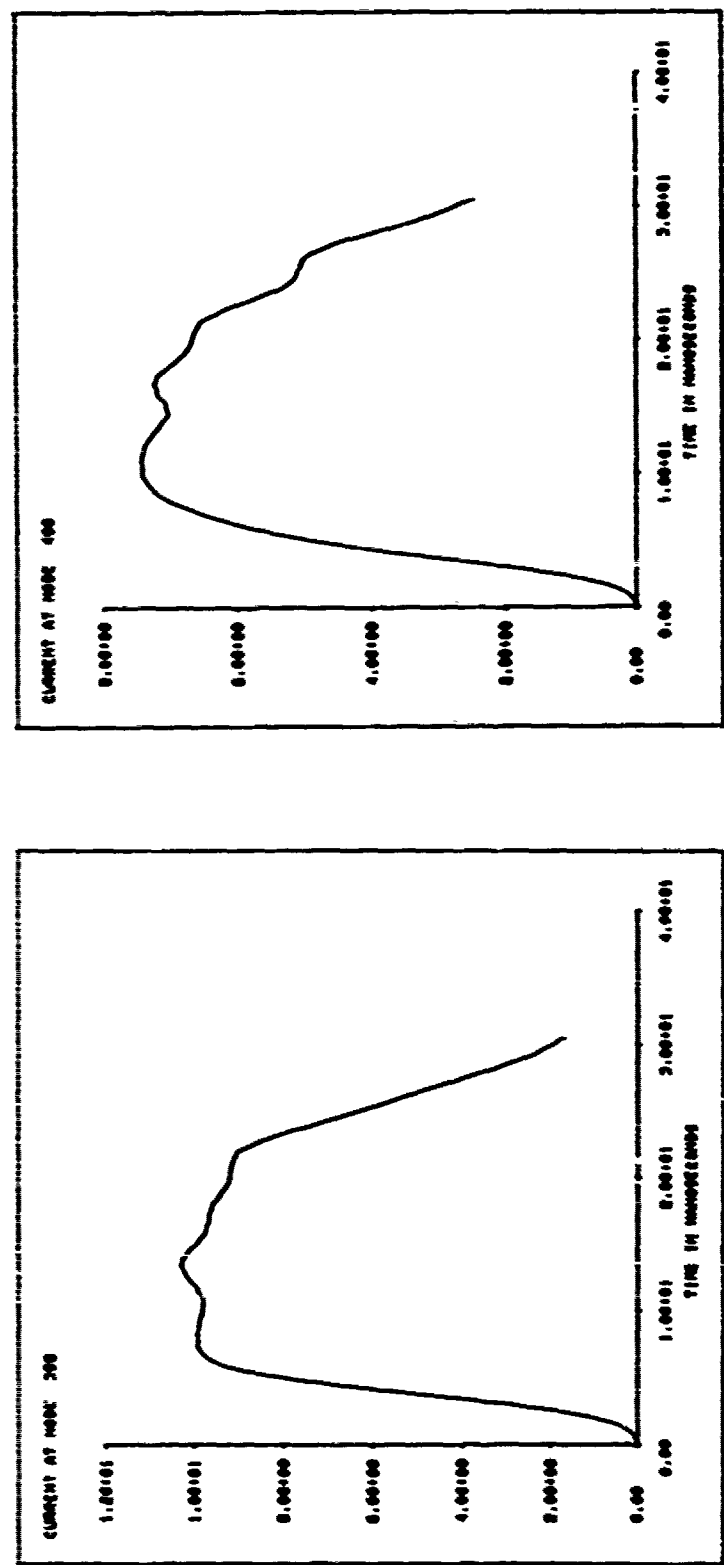


Figure B.5a,b. Surface currents, case II.

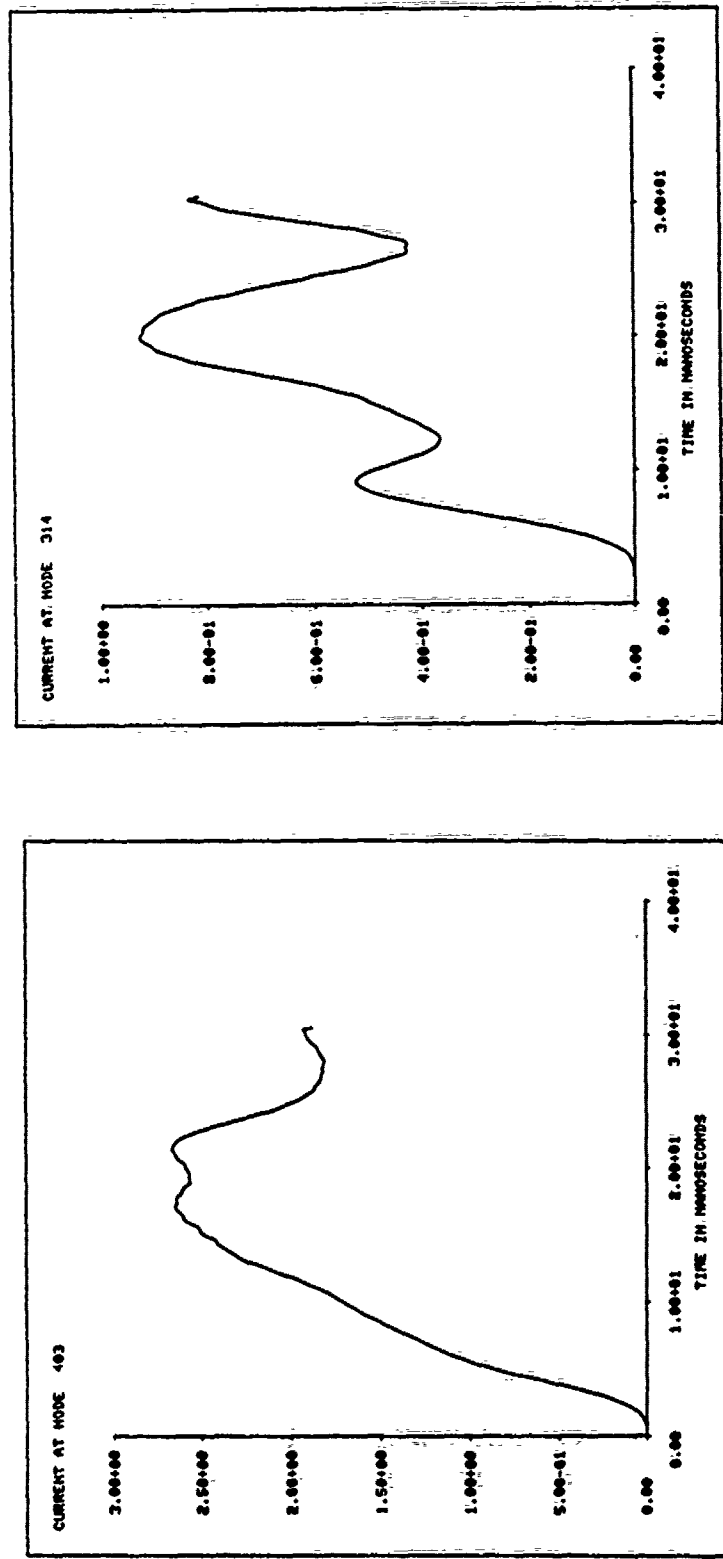


Figure B.5c,d. Surface currents, case III.

CASE III

$V_o = -10$ kV

$T = 480$ eV

$J = 200$ A/m²

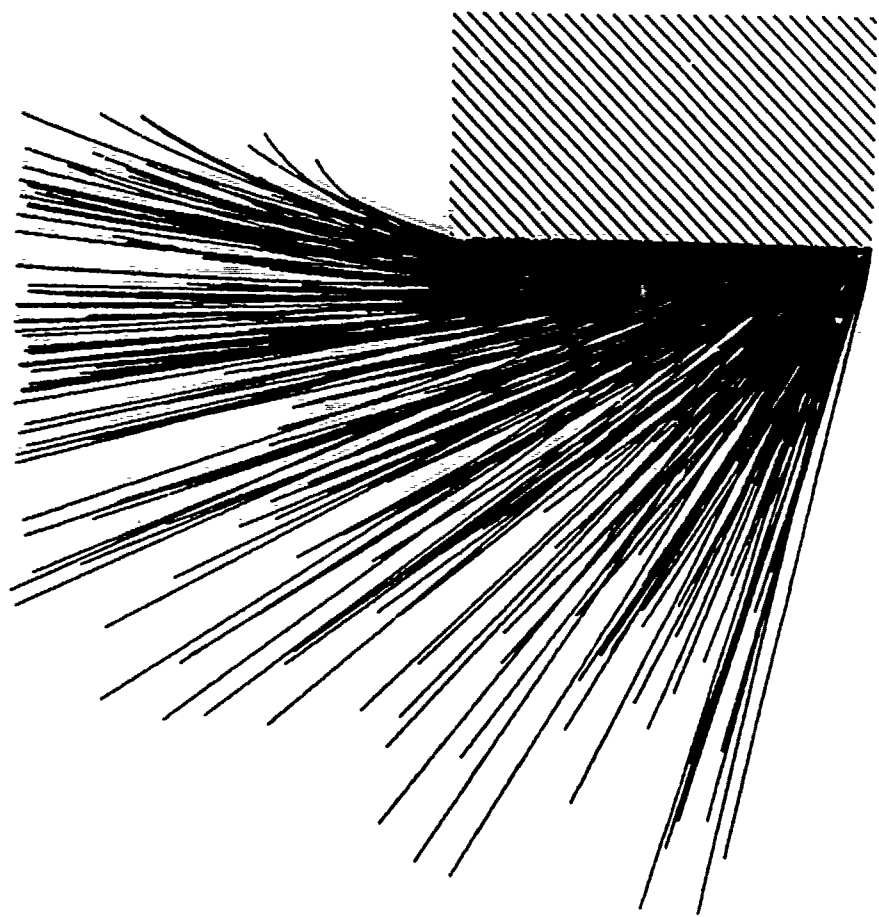


Figure B.6. Particle trajectories, Case III.

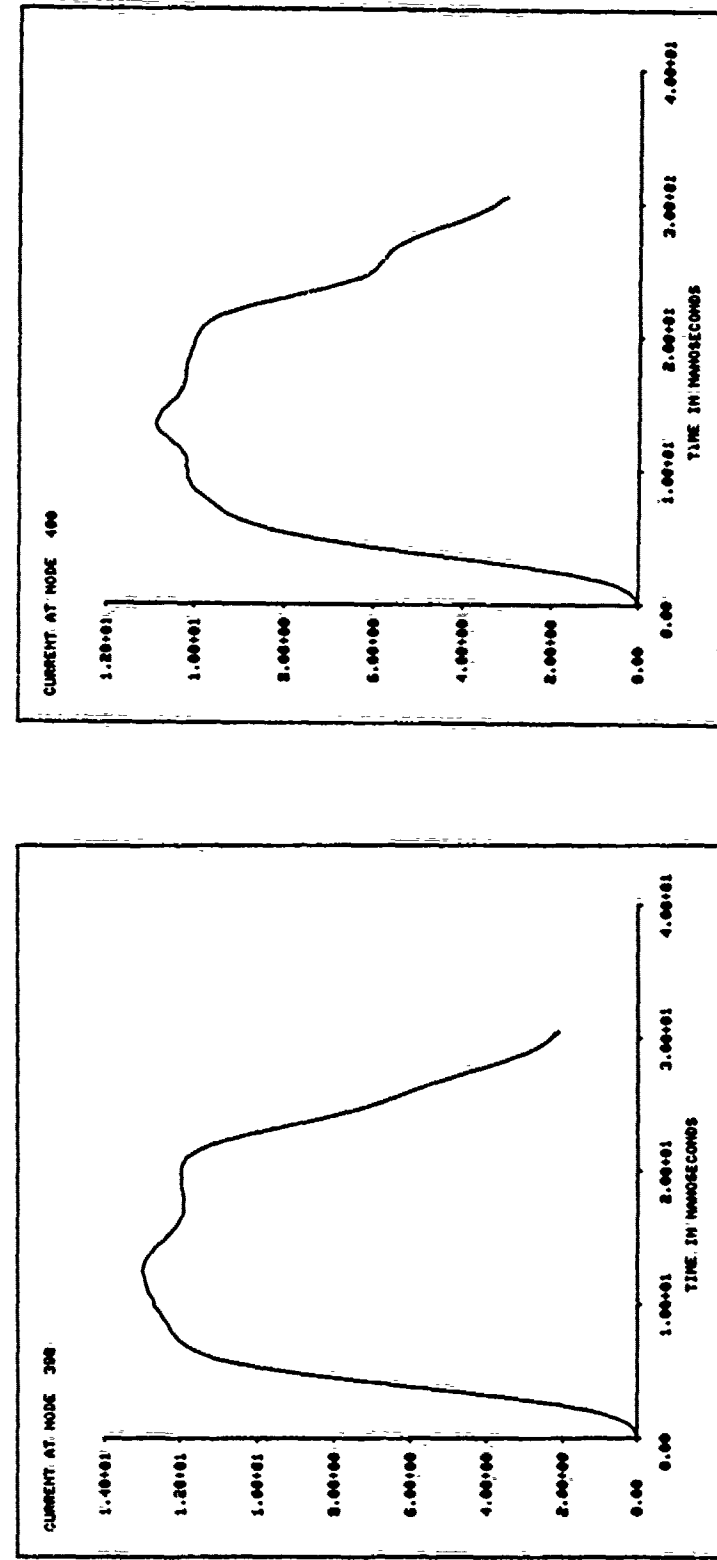


Figure B.7a,b. Surface currents, Case III.

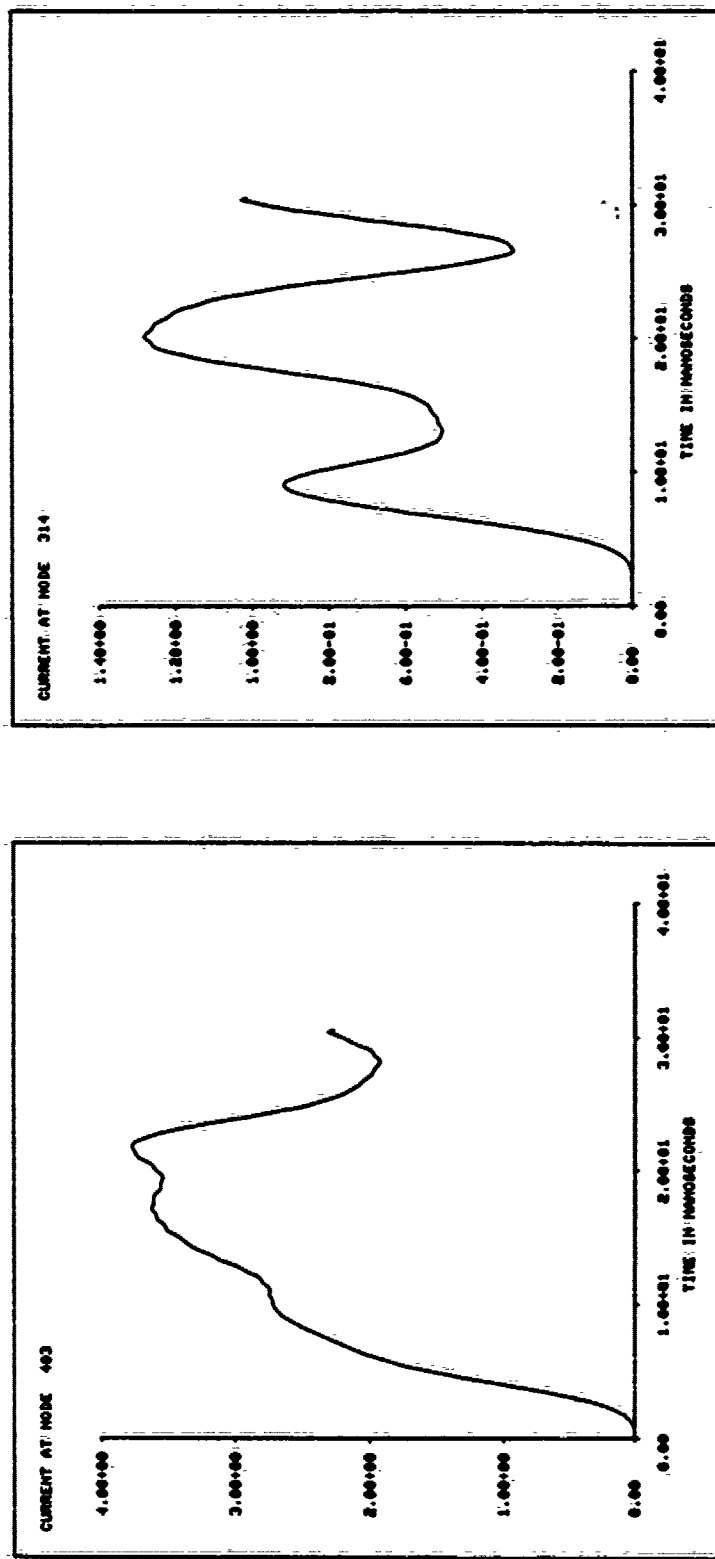


Figure B.7c,d. Surface currents, Case III.

CASE IV

$V_o = -10$ KV

$T = 30$ eV

$J = 400$ A/m²

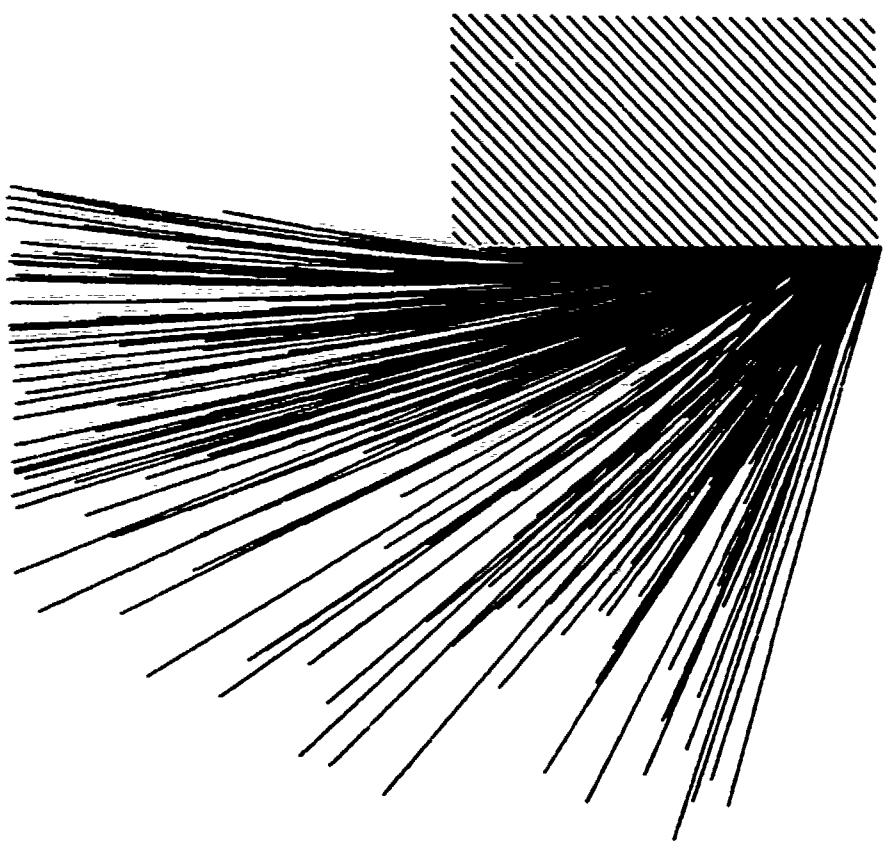


Figure B.8. Particle trajectories, Case IV.

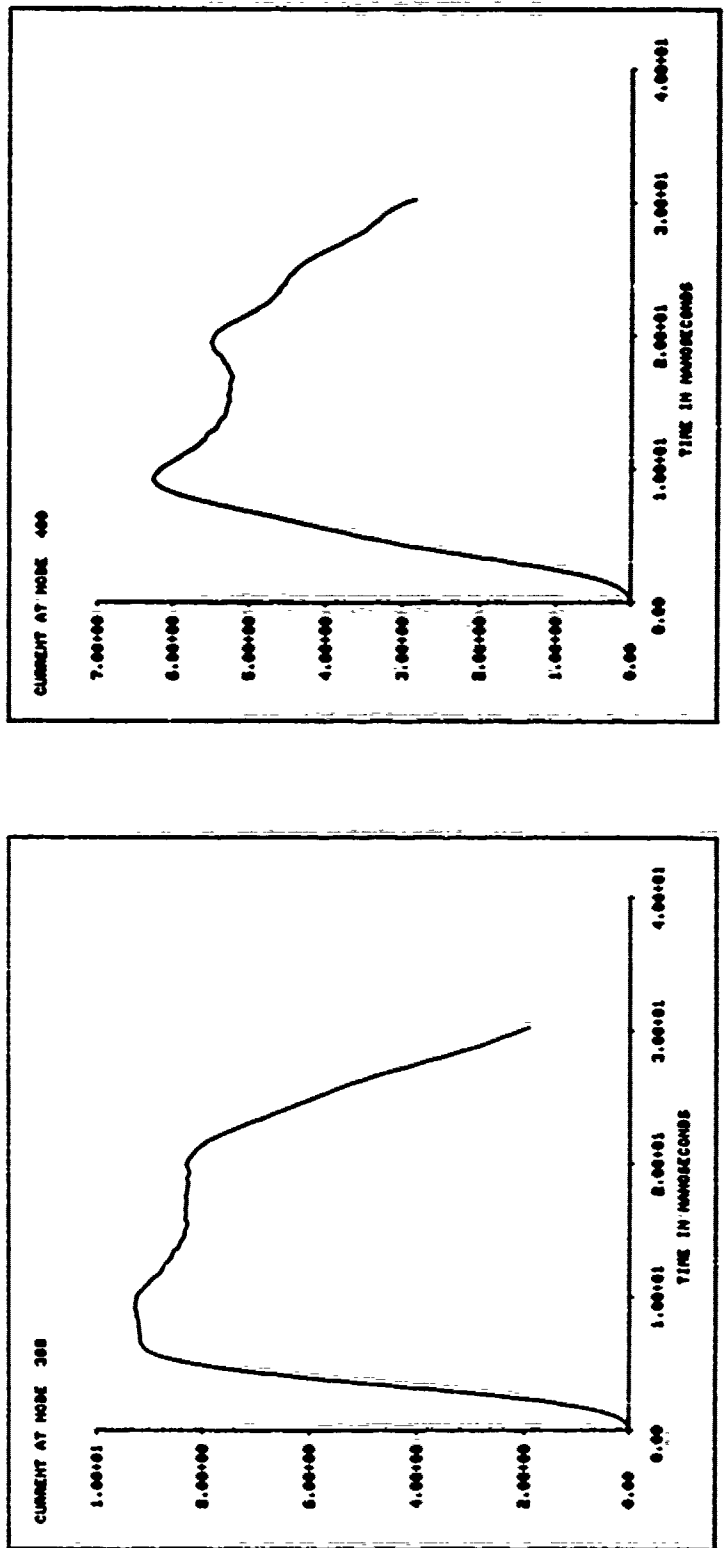


Figure B.9a,b. Surface currents, Case IV.

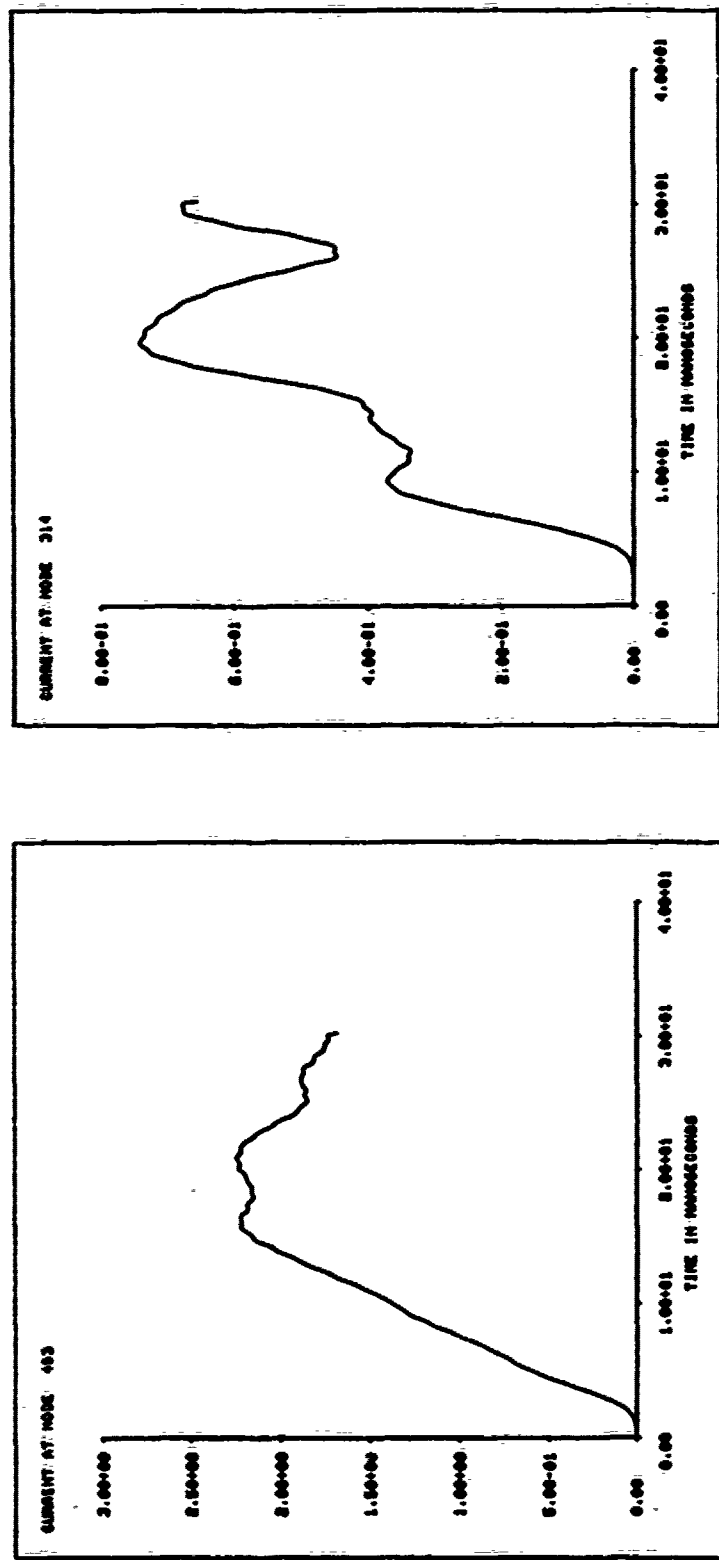


Figure B.9c,d. Surface currents, Case IV.

CASE V

$v_o = -15 \text{ kV}$

$T = 30 \text{ eV}$

$J = 400 \text{ A/m}^2$

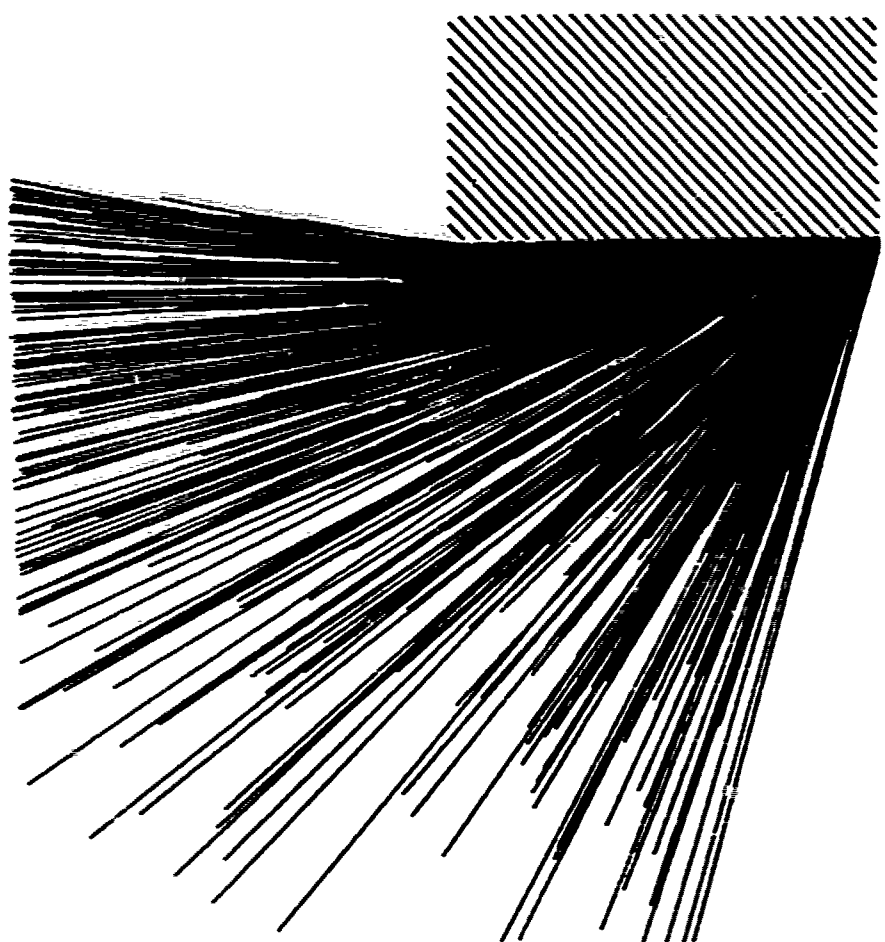


Figure B.10. Particle trajectories, Case V.

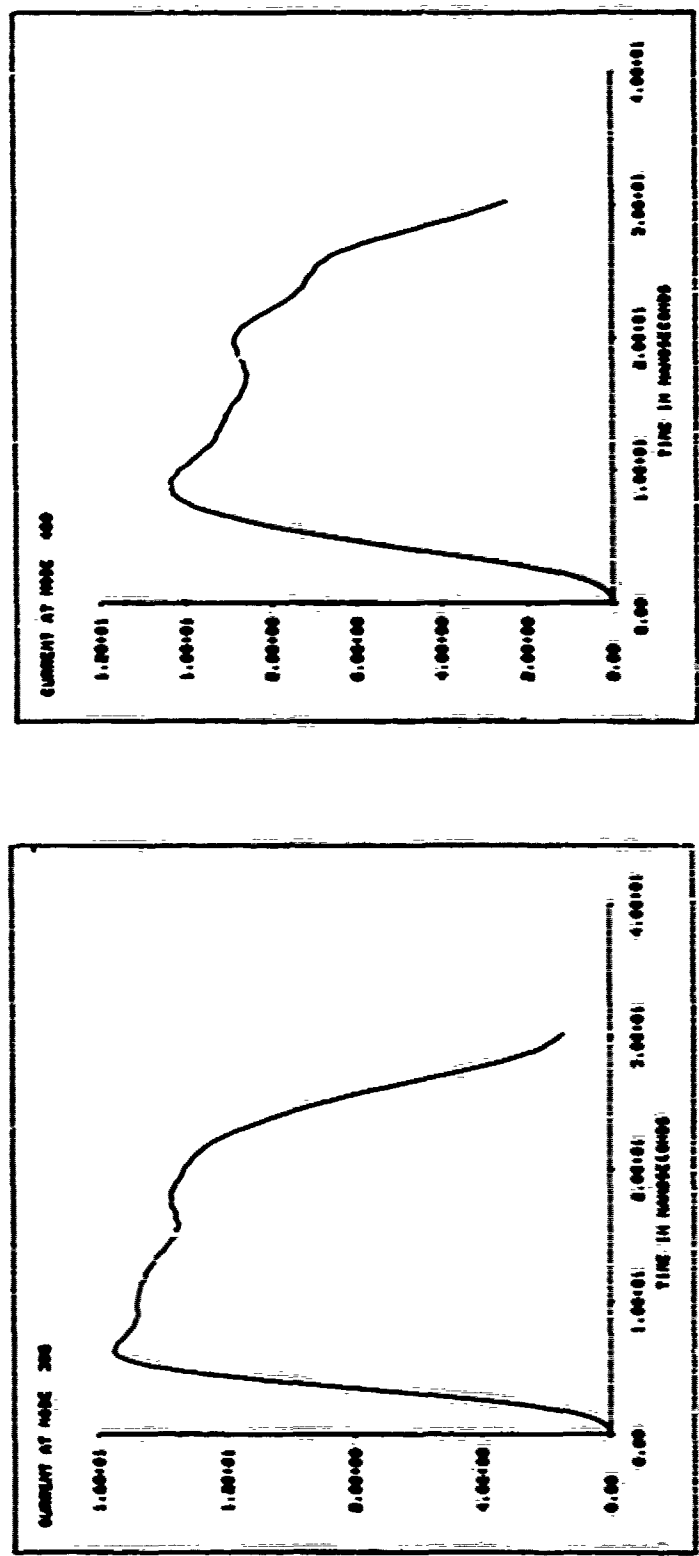


Figure B.11a,b. Surface currents, Case V.

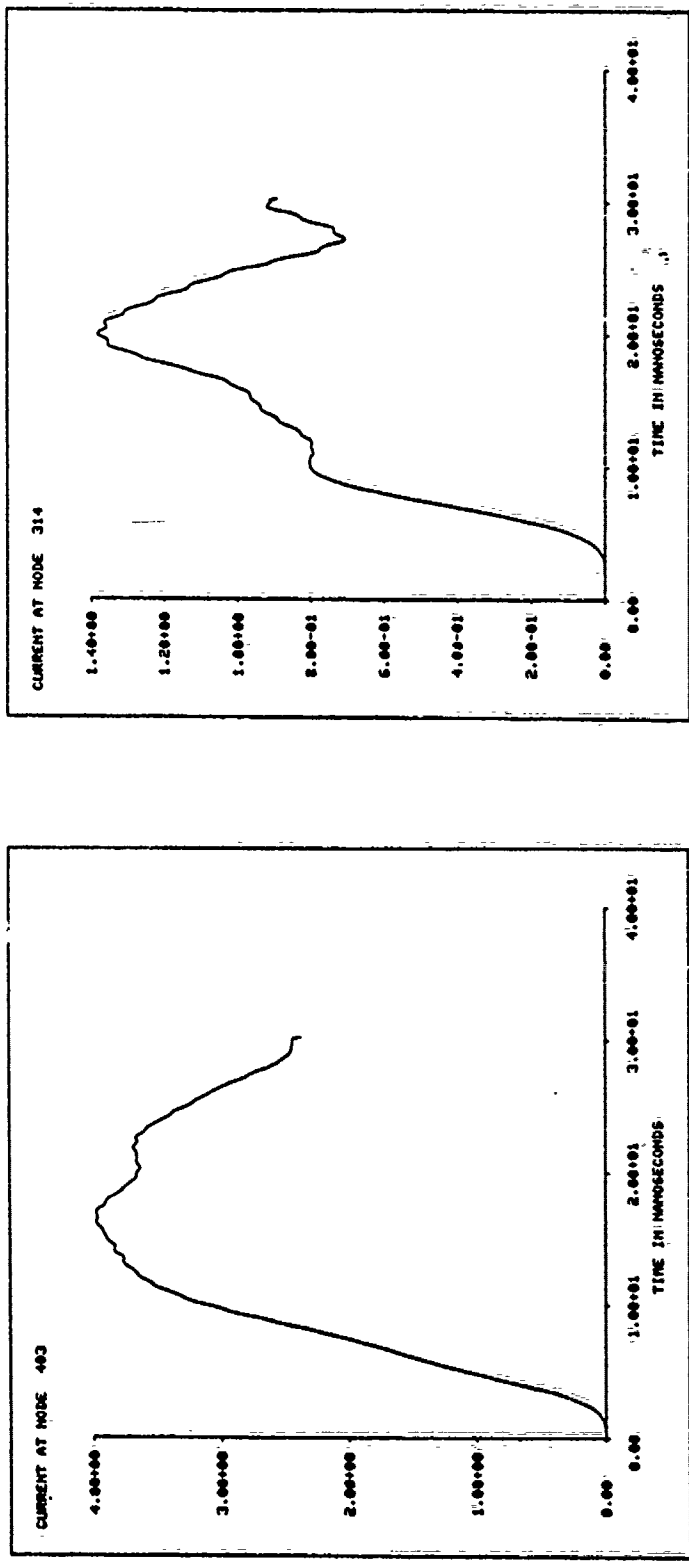


Figure B.11c,d. Surface currents, Case V.

APPENDIX C

TECHNICAL NOTE

EFFECT OF EARTH'S MAGNETIC FIELD ON
PRECHARGING EXPERIMENTS

by

G. W. Schnuelle and M. J. Mandell

TECHNICAL NOTE

EFFECT OF EARTH'S MAGNETIC FIELD ON
PRECHARGING EXPERIMENTS

G. W. Schnuelle and M. J. Mandell

The ambient magnetic field can profoundly affect the charging of an object by an electron gun in a 30 m tank. The Larmor radius for electrons is $r_L \sim 1.2 \sqrt{E/B}$ meters, where E is the electron energy in kV and B the magnetic field in gauss: $r_L \sim 7$ meters for a 10 kV gun with $B = 0.5$ gauss. Obviously some reduction of the ambient field is necessary. We have used the NASCAP code to illustrate the effects of various levels of ambient field bucking.

Figure 1 illustrates the object used in the simulations; the zone size is 1 meter. Figures 2 through 4 show the trajectories of a 1 milliamp beam of 10 kV electrons as they travel from the source toward the object. The source is positioned 16 meters from the object, and the magnetic field is oriented out of the plane of the paper. The calculation includes the combined effects of the ambient magnetic field and the electrostatic field from the charged object on the trajectories. In Figures 2 through 4, the object is uniformly charged to -5 kV, and the magnetic field is 0., .1, and .25 gauss (about half ambient) respectively.

With the field bucked to half ambient (Figure 4), electrons cannot reach the top half of the object. With the field bucked to one-fifth ambient (Figure 3), the gun can spray the entire object. However, even in this case the field causes trajectories reaching the top of the object to have much higher curvature than those striking the bottom. (Note that the curvature increases as the electron energy decreases approaching the charged object.) As a result of the angle dependence of secondary emission, the net current

density on the top portion is $+7 \times 10^{-8} \text{ A/m}^2$, while the current at the bottom is $-4 \times 10^{-8} \text{ A/m}^2$. Several thousand volts of differential charging will result from the effects of the non-zero magnetic field.

These calculations indicate that reduction of the ambient field to approximately 0.1 gauss should suffice to allow 10 keV electrons to reach a test object. However, even in this case further simulations will be required to estimate the effects of the remaining magnetic fields on differential charging.

To reduce the horizontal and vertical magnetic field components by a factor of 10 over a large tank is a major task. It has not been attempted at the NASA Johnson Space Center; instead, experiments have been performed at several field strengths and the results extrapolated.

Care in the positioning of electron guns combined with the capability of moving guns on pods out from walls could overcome at much lower cost the problem of precharging in the earth's magnetic field.

An alternative method of achieving differential charging would be: (1) bias spacecraft ground to +10 kV; (2) turn on a low energy plasma source, allowing charge to accumulate on dielectric surfaces until they are near tank ground; (3) return spacecraft to tank ground, so dielectric surfaces are at -10 kV; (4) if desired, discharge selected areas with UV source.

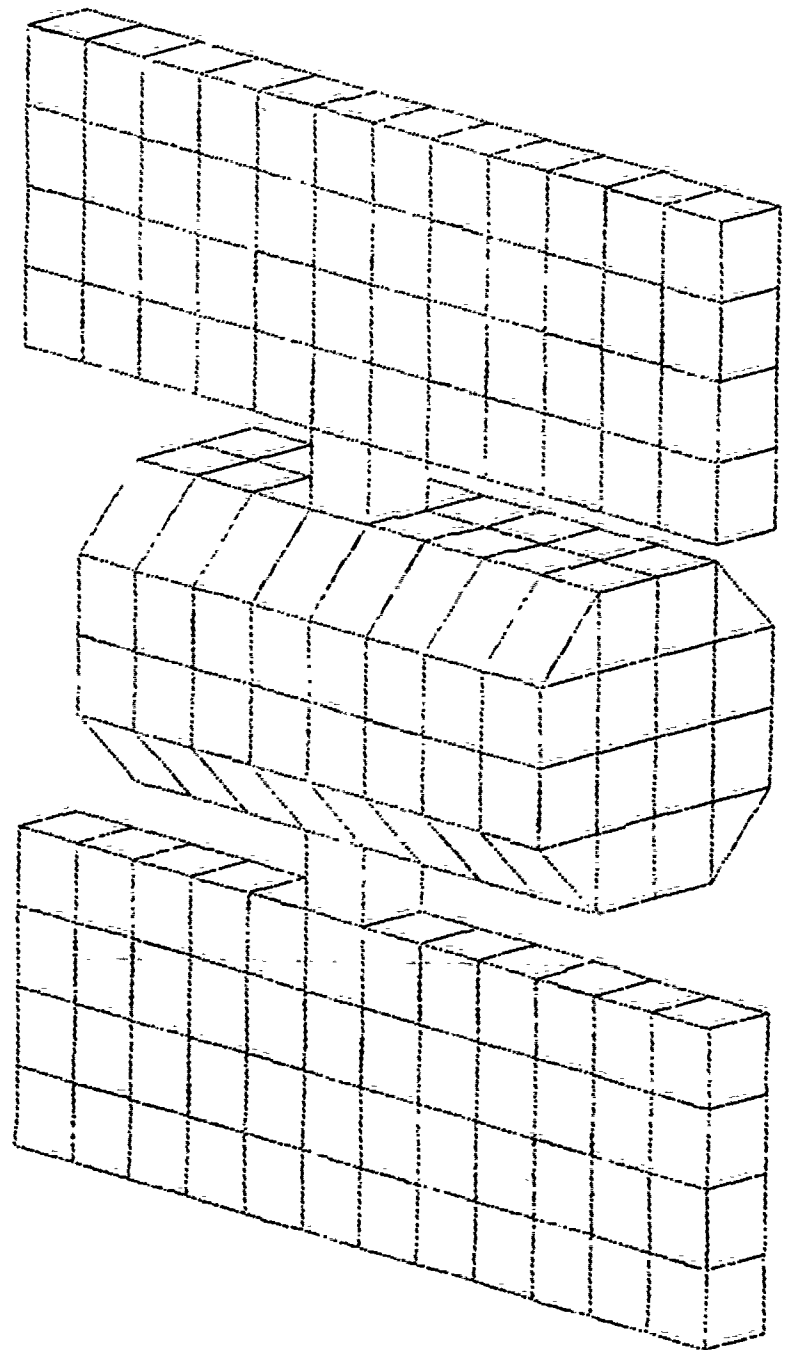


Figure 1. Test object. Zone size = 1 meter.

SSS-R-80-4205

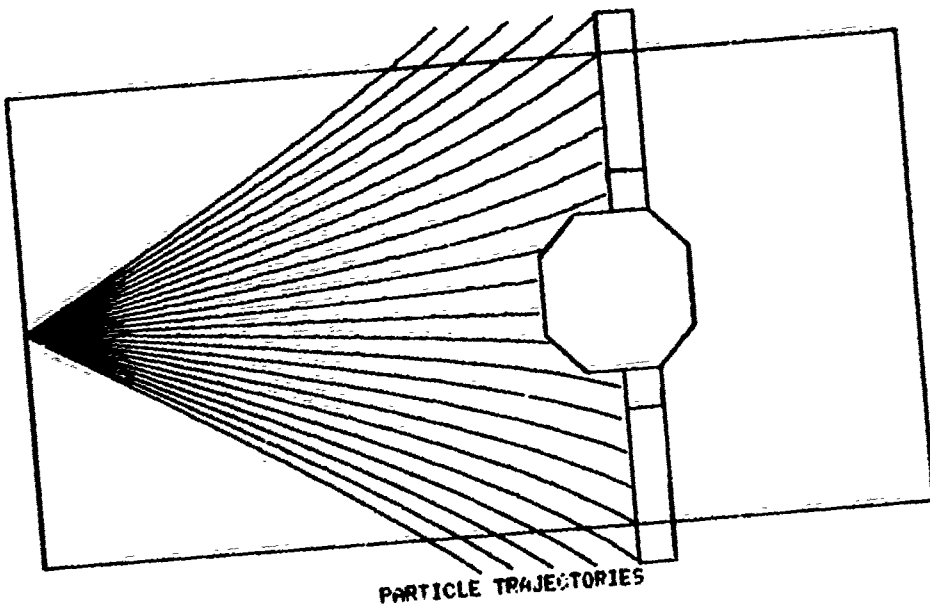


Figure 2. Trajectories of 10 kV electrons traveling 16 m to test object. No magnetic field. Object potential = -5 kV.

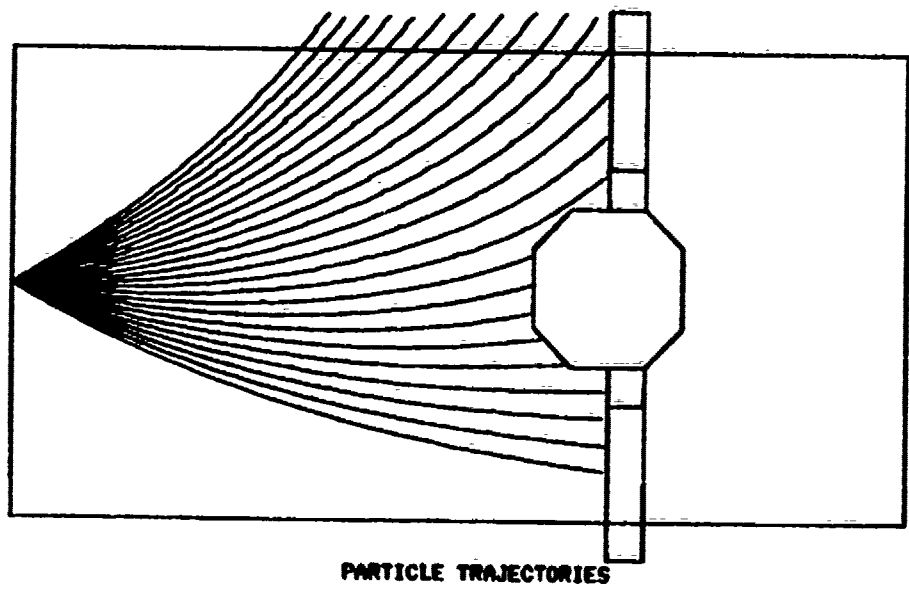


Figure 3. Trajectories of 10 kV electrons traveling 16 m to test object. Magnetic field is 0.1 gauss (out of plane of paper). Object potential = -5 kV.

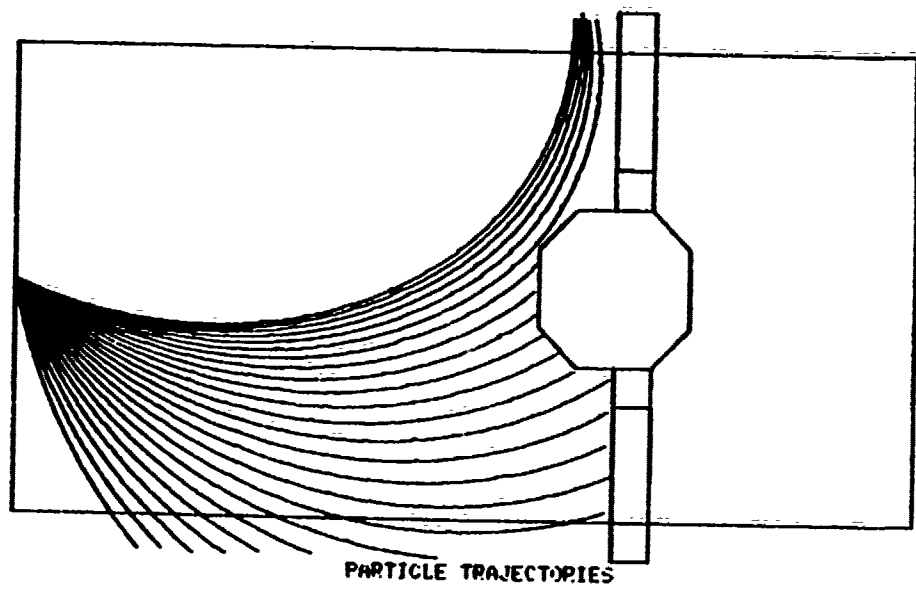


Figure 4. Trajectories of 10 kV electrons traveling 16 m to test object. Magnetic field is 0.25 gauss (out of plane of paper). Object potential = -5 kV.

DISTRIBUTION LIST

DEPARTMENT OF DEFENSE

Assistant to the Secretary of Defense
Atomic Energy
ATTN: Executive Assistant

Director
Defense Intelligence Agency
ATTN: DB-4C

Director
Defense Nuclear Agency
2 cy ATTN: RAEV
4 cy ATTN: TITL

Defense Technical Info Center
12 cy ATTN: DD

Field Command
Defense Nuclear Agency
ATTN: FCLMC
ATTN: FCPR

Field Command
Defense Nuclear Agency
Livermore Division
ATTN: FCPKL

Interservice Nuclear Weapons School
ATTN: TTV

Joint Chiefs of Staff
ATTN: J-5 Nuclear Division
ATTN: C3S Evaluation Office

Joint Strat Tgt Planning Staff
ATTN: JLA
ATTN: JLTw-2

National Communications System
Department of Defense
ATTN: NCS-TS

Undersecretary of Def for Rsch & Engng
Department of Defense
ATTN: Strategic & Space Systems (OS)
ATTN: AE

DEPARTMENT OF THE ARMY

BMD Advanced Technology Center
Department of the Army
ATTN: ATC-0

BMD Systems Command
Department of the Army
ATTN: BDMSC-H

Deputy Chief of Staff for Rsch Dev & Acq
Department of the Army
ATTN: DAMA-CSS-N

Electronics Tech & Devices Lab
U.S. Army Electronics R&D Command
ATTN: DRSEL

DEPARTMENT OF THE ARMY (Continued)

Harry Diamond Labs
Department of the Army
ATTN: DELHD-N-RBC, R. Gilbert
ATTN: DELHD-I-TL

U.S. Army Communications Sys Agency
ATTN: CCM-AD-LB

U.S. Army Foreign Science & Tech Ctr
ATTN: DRXST-IS-1

U.S. Army Missile R&D Command
ATTN: RSIC

DEPARTMENT OF THE NAVY

Naval Research Laboratory
ATTN: Code 6707, K. Whitney
ATTN: Code 7550, J. Davis
ATTN: Code 6701

Naval Surface Weapons Center
ATTN: Code F31

Strategic Systems Project Office
ATTN: NSP

DEPARTMENT OF THE AIR FORCE

Air Force Geophysics Lab
ATTN: PH, C. Pike

Air Force Weapons Lab
Air Force Systems Command
ATTN: SUL
ATTN: NT
ATTN: NXS
2 cy ATTN: DYC

Ballistic Missile Office
Air Force Systems Command
ATTN: MNH
ATTN: MNRTE
ATTN: MNG

Deputy Chief of Staff
Research, Development & Acq
Department of the Air Force
ATTN: AFRDQI

Headquarters Space Division
Air Force Systems Command
ATTN: SKF

Rome Air Development Center
Air Force Systems Command
ATTN: ESR, E. Burke

Strategic Air Command
Department of the Air Force
ATTN: NRI-STINFO Library
ATTN: XPFS

OTHER GOVERNMENT AGENCIES

Central Intelligence Agency
ATTN: OSWR/STD/HTB, A. Padgett

NASA
Lewis Research Center
ATTN: N. Stevens
ATTN: C. Purvis
ATTN: Library

DEPARTMENT OF ENERGY CONTRACTORS

Lawrence Livermore National Lab
ATTN: Technical Info Dept Library

Los Alamos National Scientific Lab
ATTN: MS 364

Sandia National Labs
Livermore Laboratory
ATTN: T. Dellin

Sandia National Laboratories
ATTN: 3141

DEPARTMENT OF DEFENSE CONTRACTORS

Aerospace Corp
ATTN: Library
ATTN: V. Josephson

AVCO Research & Systems Group
ATTN: Library A830

Boeing Company
ATTN: P. Geren

Computer Sciences Corp
ATTN: A. Schiff

Dikewood Corporation
ATTN: Technical Library

Dikewood Corporation
Los Angeles Operations
ATTN: K. Lee

EG&G Wash Analytical Services Ctr, Inc
ATTN: Library

Ford Aerospace & Communications Corp
ATTN: A. Lewis
ATTN: Technical Library

General Electric Company
Space Division
ATTN: J. Peden

General Electric Company—TEMPO
ATTN: W. McNamara
ATTN: DASIAC

Hughes Aircraft Company
ATTN: Technical Library

DEPARTMENT OF DEFENSE CONTRACTORS (Continued)

Institute for Defense Analyses
ATTN: Classified Library

IRT Corp
ATTN: B. Williams
ATTN: Library
ATTN: N. Rudie

JAYCOR
ATTN: E. Wenaas
ATTN: Library

JAYCOR
ATTN: R. Sullivan

Johns Hopkins University,
Applied Physics Lab
ATTN: P. Partridge

Kaman Sciences Corp
ATTN: W. Rich
ATTN: Library
ATTN: N. Beauchamp
ATTN: D. Osborn

Lockheed Missiles & Space Co, Inc
ATTN: Dept 85-85

McDonald Douglas Corp
ATTN: S. Schneider

Mission Research Corp
ATTN: C. Longmire
ATTN: R. Stettner

Mission Research Corp
ATTN: B. Goplen

Mission Research Corp—San Diego
ATTN: V. Van Lint
ATTN: Library

Pacific Sierra Research Corp
ATTN: H. Brode

R & D Associates
ATTN: S. Siegel
ATTN: Technical Info Center
ATTN: L. Schlessinger
ATTN: R. Schaefer
ATTN: P. Haas

Rockwell International Corp
ATTN: Library

Science Applications, Inc
ATTN: W. Chadsey

Spire Corp
ATTN: R. Little

SRI International
ATTN: Library

DEPARTMENT OF DEFENSE CONTRACTORS (Continued)

Systems, Science & Software, Inc

ATTN: A. Wilson
ATTN: Library
ATTN: M. Mandell
ATTN: D. Parks
ATTN: G. Schnuelle
ATTN: I. Katz
ATTN: E. Waisman
ATTN: P. Steen
ATTN: M. Rotenberg

DEPARTMENT OF DEFENSE CONTRACTORS (Continued)

TRW Defense & Space Sys Group

ATTN: D. Clément
ATTN: Technical Information Center

Hughes Aircraft Company

ATTN: E. Smith
ATTN: W. Scott
ATTN: A. Narevsky